

HOCHSCHULE NEUBRANDENBURG
UNIVERSITY OF APPLIED SCIENCES
FACULTY OF GEODESY AND GEOINFORMATICS

A THESIS SUBMITTED TO THE UNIVERSITY OF APPLIED SCIENCES
HOCHSCHULE NEUBRANDENBURG FOR THE DEGREE OF MASTER OF SCIENCES IN
GEODESY AND GEOINFORMATICS

**Validation of Neustrelitz Peak electron Density Model
(NPDM) and Peak Height Model (NPHM) using ground-
and space-based observations**

By

Yuliia Hresko

MS.C, Department of Higher Geodesy and Astronomy,
Faculty of Geodesy, Lviv Polytechnic National University

Under Supervision of

Dr. Mainul Hoque

Doctor, Institute of communication and navigation, German Aerospace Center
(DLR), Germany

Prof. Dr.-Ing. Andreas Wehrenpfennig

Professor, Doctor of Engineering, Department of Landscape Architecture,
Geoinformatics, Geodesy and Civil Engineering, Hochschule Neubrandenburg

June, 2019

Table of contents

Abstract

Chapter1. Introduction.....	6
1.1. Motivation of the research.....	6
1.2. Structure of the thesis.....	7
Chapter2. The Earth's atmosphere.....	8
2.1. General Description of the Atmospheric Regions, Composition and Temperature.....	8
2.2. Ionosphere.....	10
2.2.1. Formation of the ionosphere.....	10
2.2.2. Regular ionospheric layers.....	11
2.2.2.1. The D layer	12
2.2.2.2. The E layer.....	13
2.2.2.3. The F layer.....	13
2.2.2.4. The F1 layer.....	14
2.2.2.5. The F2 layer.....	14
2.2.2.6. Topside layer.....	15
2.2.2.7. Plasmasphere.....	15
2.2.3. Major geographic regions of the Ionosphere.....	16
2.2.3.1. Low latitudes.....	16
2.2.3.2. Middle Latitude Ionosphere.....	16
2.2.3.3. High-Latitude Region.....	17
2.3. Ionospheric Variability.....	17
2.3.1. Diurnal and Seasonal variation.....	17
2.3.2. Latitudinal Variation.....	18
2.3.3. Solar Cycle Variation.....	18
Chapter3. The ionospheric electron density models.....	20
3.1. Categorization of models.....	20
3.2. NPDM (Neustrelitz Peak Density Model)	22
3.3. NPHM (Neustrelitz Peak Height Model)	25
3.4. NeQuick (quick-run ionospheric electron density model)	27
Chapter4. Data resource.....	29
4.1. IPS (The Ionospheric Prediction Service)	29
4.2. SPIDR (Space Physics Interactive Data Resource)	30
4.3. IRO (Ionospheric radio occultation measurements)	30

4.4. NGDC (National Geophysical Data Center)	31
Chapter5. Model validation using ground based data (Ionosonde)	33
5.1. Analysis of the peak electron density NmF2.....	37
5.2. Analysis of the peak height hmF2.....	48
5.3. Time series analysis of the Ionosonde data (2009-2018 years)	53
5.3.1. JR055	56
5.3.2. RL052	58
5.3.3. RO041.....	61
5.4. The statistic for $NmF2_{mod}$ - $NmF2_{obs}$ and $hmF2_{mod}$ - $hmF2_{obs}$	64
Chapter6. Model validation using space based data (RO).....	73
6.1. Analysis of the peak electron density NmF2.....	79
6.2. Analysis of the peak height hmF2.....	86
6.3. The statistic for $NmF2_{mod}$ - $NmF2_{obs}$ and $hmF2_{mod}$ - $hmF2_{obs}$	96
Conclusions.....	97
References.....	98
List of figures.....	99
List of tables.....	103

Abstract

Nowadays study of the Earth's ionosphere is one of the main goals for human society, since the accuracy of positioning, navigation and quality of telecommunication depends on ionospheric effects. The ionosphere significantly is a highly variable environment that exhibits significant variation with altitude, latitude, longitude, diurnal, and seasonal variation as well as solar and geomagnetic activity. This variability arises from the coupling, time delays, and feedback mechanisms that are inherent in the ionosphere-thermosphere system, as well as from the effects of the solar, interplanetary, magnetosphere, and mesosphere, stratosphere, troposphere, and even lithosphere processes. When the radio waves propagate through the ionosphere, they are affected by different factors such as reflection, absorption, diffraction, refraction, polarization and scattering. The ionospheric delay is the most dominant error source for satellite navigation signals. This error can be directly measured and mostly mitigated using dual-frequency GNSS receivers. In present time, GNSS systems are using different ionospheric models for providing real-time ionospheric delay correction for single frequency users. This thesis analyzed validation of NTCM based modelling approaches for the estimation of ionospheric key parameters. Empirical modeling is important for the study of the ionosphere and practical applications. For our research we have used three ionospheric models: the quick run model (NeQuick), Neustrelitz Peak Density Model (NPDM) and Neustrelitz Peak High Model (NPHM). The model approach is applied to a vast quantity of global NmF2 and hmF2 data derived from GNSS radio occultation measurements by CHAMP, GRACE and COSMIC satellite missions and about 60 years of processed NmF2 data from 91 and hmF2 data from 27 worldwide ionosonde stations.

To compare models performance, we have computed the differences between ionosonde data, IRO data and model results for all hourly values of NmF2 and hmF2 and estimated the RMS of differences at each verification station for the selected periods. Regarding ionosonde data the NPDM model performs better than the NeQuick for all stations. The NPHM model performs better than the NeQuick for most of the stations except at medium latitude at medium and high solar activity. The NeQuick shows the worst performance at low latitude at medium and high solar activity root mean square is equal 6.0 and $6.6 \times 10^{11} \text{ m}^{-3}$ respectively. The NPDM model shows the best performance at low latitude at low and medium solar activity root mean square is equal 0.7 and $1.1 \times 10^{11} \text{ m}^{-3}$ respectively. Regarding IRO data the NPDM model performs better than the NeQuick for most of the stations except at low latitude at high solar activity. Both models show the best performance at low latitude at low solar activity and root mean square is equal $1.8 \times 10^{11} \text{ m}^{-3}$. The NPHM

model shows the best performance at medium latitude at medium solar activity. The results show that the NPDM and NPHM models show better performance than the NeQuick model on average. The performance of the model may be further improved by extending the database used.

Chapter1. Introduction

1.1. Motivation of the research

One of the largest errors in GPS positioning is attributable to the atmosphere. The long, relatively unhindered travel of the GPS signal through the virtual vacuum of space changes as it passes through the earth's atmosphere. Through both refraction and diffraction, the atmosphere alters the apparent speed and, to a lesser extent, the direction of the signal. This causes an apparent delay in the signal's transit from the satellite to the receiver.

The ionosphere is ionized plasma comprised of negatively charged electrons which remain free for long periods before being captured by positive ions. It extends from about 50 km to 1000 km above the earth's surface.

The magnitude of these delays is determined by the state of the ionosphere at the moment the signal passes through, so it's important to note that its density and stratification varies. The sun plays a key role in the creation and variation of these aspects. Also, the daytime ionosphere is rather different from the ionosphere at night.

When gas molecules are ionized by the sun's ultraviolet radiation, free electrons are released. As their number and dispersion varies, so does the electron density in the ionosphere. The higher the electron density, the larger the delay of the signal, but the delay is by no means constant.

The ionospheric delay changes slowly through a daily cycle. It is usually least between midnight and early morning, and most around local noon or a little after. During the daylight hours in the mid-latitudes, the ionospheric delay may grow to be as much as five times greater than it was at night. It is also nearly four times greater in November, when the earth is nearing its perihelion, its closest approach to the sun, than it is in July near the earth's aphelion, its farthest point from the sun. The effect of the ionosphere on the GPS signal usually reaches its peak in March, about the time of the vernal equinox.

There are several empirical ionospheric models. Well known empirical models included in our research are Neustrelitz Peak Density Model (NPDM), Neustrelitz Peak Height Model (NPHM) and quick-run ionospheric electron density model (NeQuick). As each of the models applies different modeling approaches and were developed with different background data, we assume that NmF2 and hmF2 modeling performance differ and the use of one model in particular conditions would be better than use of another. In the present study, the peak electron density of the F2 layer (NmF2) and the maximum ionization height (hmF2) derived from NeQuick model are compared with NPDM and NPHM values in term of model deviations from the same reference truth observations.

1.2. Structure of this thesis

In chapter one is given the motivation of the research, the aim of study and an introductory information about ionosphere.

In chapter two a brief description of atmospheric regions, composition and temperature is given. Also the formation of the ionosphere, regular ionospheric layers, major geographic regions of the ionosphere and ionospheric variability are described.

In chapter three the information about the categorization of the ionospheric models is given. In addition three models are described, which we have used for our investigation, namely the Neustrelitz Peak Density Model (NPDM), the Neustrelitz Peak Height Model (NPHM) and the Quick-run ionospheric electron density model (NeQuick).

Chapter four contains information about the data sources such as the Ionospheric Prediction Service (IPS), Space Physics Interactive Data Resource (SPIDR), National Geophysical Data Center (NGDC) and Ionospheric Radio Occultation (IRO) data.

In chapter five is given model validation on ground based data, analysis of the peak electron density $NmF2$ and peak height $hmF2$ and time series analysis of the Ionosonde data (2009-2018 years) for three ionosonde stations JR055 (JULIUSRUH/RUGEN), RL052 (CHILTON) and RO041 (ROME). Also statistics for $NmF2_{mod}$ - $NmF2_{obs}$ and $hmF2_{mod}$ - $hmF2_{obs}$, namely root mean square, standard deviation and mean value are presented.

Chapter six contains a model validation on space based data (IRO data), analysis of the peak electron density $NmF2$ and peak height $hmF2$. Also statistics for $NmF2_{mod}$ - $NmF2_{obs}$ and $hmF2_{mod}$ - $hmF2_{obs}$, namely root mean square, standard deviation and mean value are given.

Chapter2. The Earth atmosphere

2.1. General Description of the Atmospheric Regions, Composition and Temperature

The atmosphere is the gas envelope of the planet Earth, stretching up to a thousand kilometers up above the surface and retained by the Earth's gravity. The atmosphere takes part in the daily rotation and annual motion of our planet. This layer consists of a mixture of gases in which the liquids (droplets of water) and solid particles (smoke, dust) are in a suspended state.

The main parts of the atmospheric air are Nitrogen and Oxygen. In percentage the atmosphere is composed of about 78% Nitrogen (N₂), about 21% Oxygen (O₂), 0.97% Argon and Carbon dioxide 0.04%. The thickness of this layer is several thousand kilometers. As the air density decreases, the atmosphere without a clear boundary goes into outer space. The upper boundary of the atmosphere is approximately 20,000 km. Its lower boundary passes along the level of the earth's surface. 95% of the mass of the entire atmosphere is up to 25 km high, as it is held by the force of earthly gravity.

The most important parameter used to describe the vertical structure and regions of the atmosphere is the behavior of temperature with altitude (fig. 2.1), because it reflects the numerous physical and chemical processes. By this characteristic the earth's atmosphere is divided into five main layers: troposphere (0-12 km), stratosphere (12-50 km), mesosphere (50-80 km), thermosphere (80-700 km), exosphere (above 800 km). Intermediate layers between them are called respectively - tropopause, stratopause, mesopause, thermopause (Matveev 1984).

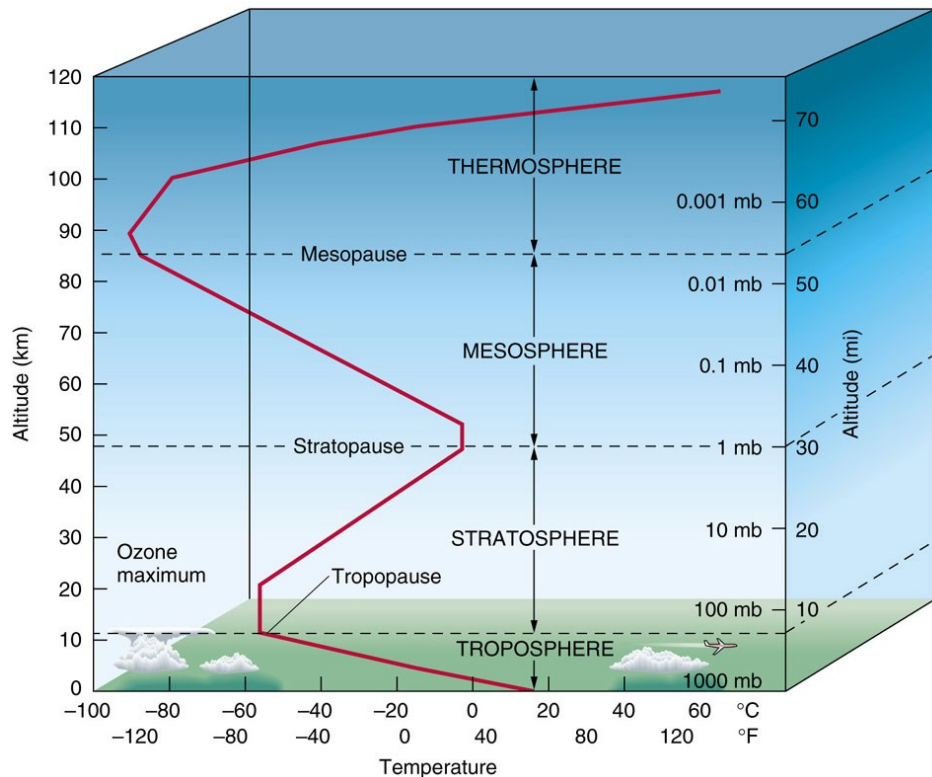


Fig.2.1. Vertical temperature profile of the atmosphere

The lowest layer of Earth's atmosphere is called troposphere. It extends from the Earth's surface to an average height up to 10 km above the poles and up to 15 km above the equatorial regions. The average temperature in troposphere is decreasing about 0.6° C every 100m (Zuev, Komarov, 1986). This layer is characterized by significant horizontal differences in the distribution of temperature, pressure and wind speed. Up to this level is the section of the atmosphere that supports life, where most weather phenomena occur, and where the physical process is mainly thermodynamic. The reason for this decrease in temperature is the vertical convective movement of the air: the gas in contact with the warm surface of the Earth expands and cools as it moves upwards in an adiabatic process. From above the troposphere is bounded by the tropopause.

The next relatively thin layer in the Earth's atmosphere is the tropopause. There the lowering of temperature with a height and above which the atmosphere becomes transparent for thermal radiation is stopped. The height of the tropopause in the arctic latitudes is 8 – 12 km, at the equator it is 16 – 18 km. In winter, the tropopause is located lower than in the summer. Also the height of the tropopause varies during cyclones and anticyclones: it decreases in cyclones, and increases in anticyclones.

The stratosphere is the next layer of Earth's atmosphere after the tropopause. This layer extends from 12 km above Earth's surface to the stratopause at an altitude of about 50 to 55 km. The stratosphere is a layer, in which temperatures rise with increasing altitude.

Although the temperature may be -60°C at the tropopause, the top of the stratosphere is much warmer, and may be near 0°C .

Above a maximum altitude of about 50 km the temperature begins to decrease again in a transition region called the mesosphere, continuing up to about 90 km where the temperature reaches about -70 to -90 K . The upper limit of the mesosphere is the mesopause, above which lies the thermosphere, where the temperature increases again due to the absorption of UV rays by oxygen and nitrogen, reaching a temperature of $1,500\text{ K}$ at an altitude of 200–300 km. Matter at this height is of extremely low density and consequently, the temperature parameter is meaningless and it is better to consider the mean quadratic velocity of the particles.

In this portion of the upper atmosphere the molecular oxygen and nitrogen are not evenly mixed, instead they are stratified according to their molecular mass with a particular scale height. In the thermosphere and upper region of the exosphere the strong UV radiation and X-rays produces an intense ionization so these two regions overlap with the ionosphere.

The ionosphere is not a distinct layer like troposphere, tropopause and others. This region includes the thermosphere, parts of the mesosphere and exosphere.

2.2. Ionosphere

2.2.1. Formation of the ionosphere

The ionosphere is ionized by solar radiation. The Sun emits ultraviolet, infrared, soft and hard X-rays, visible light and even cosmic waves. All these rays come from outer space, travelling earthwards into earth-surrounding atmosphere. Some of radiations are more dominant and more intense than others. At different altitudes in the ionosphere are presented various peaks in ionization. The density and temperature of the exhaust gases at different heights and the diversity of radiation are the main causes of the formation of various types of ionized layers at different height in the ionosphere. When the radiation rays enters the earth's atmosphere from above, they first encounter a rarefied population of gas particles in its extreme upper part, starting at an altitude of about 1,000 kilometers. At this height, the ionization process absorbs a very small, almost insignificant part of the radiation. Moving further earthwards, the rays encounter with an increase in the population of molecules and gas atoms. Therefore, ionization increases, which increases the density of electrons. UV and EUV rays play an important role for ionization between 140 to 350 kilometers. They form a layer of high electron density, known as the F-layer. In the daytime, the F-region is divided into two separated layers, known as F₂ and F₁. The F₂ is the most dominant and is located higher than

the F1. Of the two F-layers, F2 is the most important for radio communications. As sun light passes through the F-layer, most of the UV and EV rays are consumed by the ionization of that region.

Solar soft X-rays don't lose much of their strength travelling through the highest altitudes. At a height between 90 to 140 kilometers, they ionize a region and deposit most of their energy. This layer is called the E-layer. At an altitude of approximately 105 kilometers is the second peak of electron density. In this region sporadic additional ionization can be found in the form of drifting clouds with a high density of electrons, known as Es (sporadic E). Solar radiation with higher frequencies and with greater energy can penetrate further into the earth's atmosphere before repayment. That is why hard X-rays and Lyman-alpha can penetrate a height of 50 to 90 kilometers to ionize the lowest region of interest for radio communications. This region is called the D-layer.

In the ionosphere, radio waves require interaction with charged particles. Ions are also charge positive or negative, but they are much more massive than an electron. For this reason, the range of motion of the ion produced by the electric field of radio waves is much less than that of an electron, and it can be neglected in most discussions about the propagation of radio waves.

2.2.2. Regular ionospheric layers

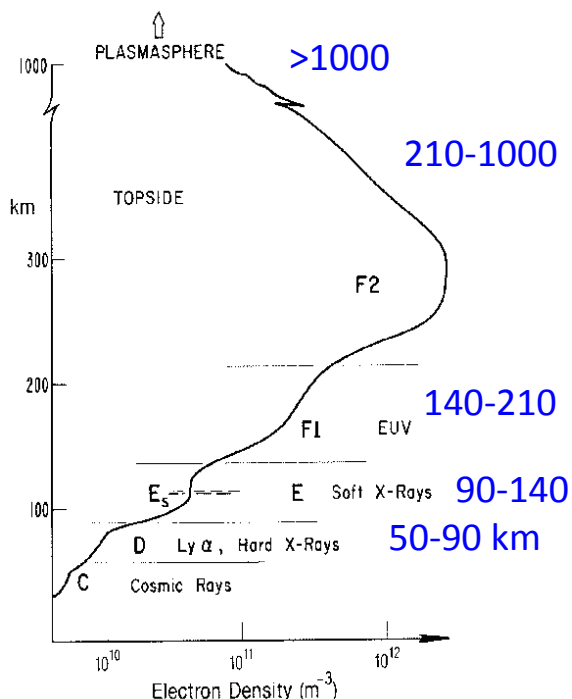


Fig. 2.2. The structure of the ionosphere (Brand, 1998)

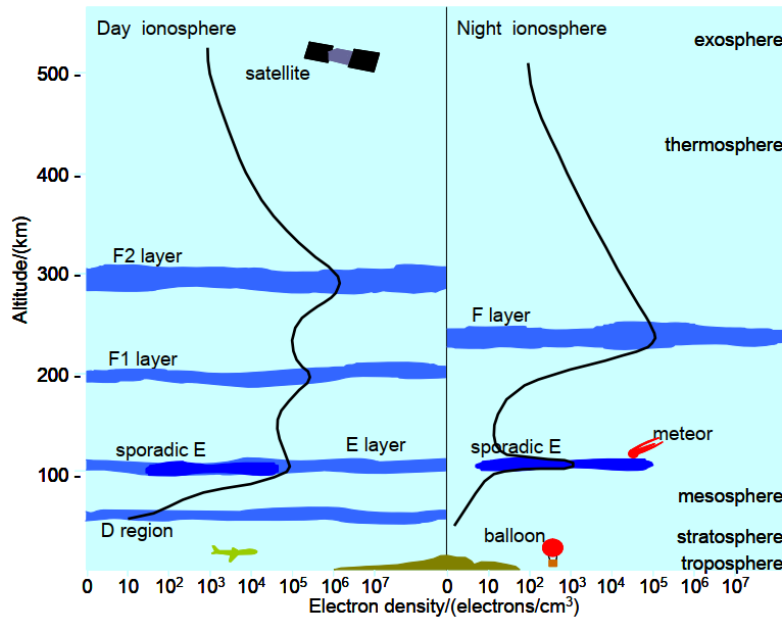


Fig.2.3.Day and night structure of the ionosphere

The ionosphere consists of a group of layers D, E and F. The layer F is divided into two regions F1 and F2.

Appleton was accustomed to using the symbol E to describe the electric field reflected from the first layer of the ionosphere, which he researched. Later Appleton discovered the second layer at a higher elevation and used the F symbol for the reflected wave. Suspecting a layer at a lower altitude, he adopted an additional symbol D. At that time, the letters became associated with the balls themselves, and not with the field of reflected waves. It is now known that electron density increases more or less evenly with height from the D-region, reaching a maximum in the F2 region.

2.2.2.1. The D-layer

The D-layer is the lowest and closest to the earth. This region is situated about 60 km to 100 km altitude. Between 90 and 100 km, the D-layer is ionized with the hard X-rays as the primary source. Lyman Alpha line radiation is the controlling source from 80 to 90 km. From 65 to 80 km, galactic cosmic rays have been shown to be the primary ionizing source. Enhancement of any of the sources causes an immediate increase in ionization of the D-layer. It builds up at sunrise, disappears at sundown, and reaches the highest ionization density at midday. The D-layer exists only during daytime. It needs constant radiation to supply continuously the ions that otherwise recombine very quickly to neutral atoms. The D-layer is

lesser ionized compared with the F-layer, but the dense concentration of more massive ions causes radio wave energy to be easily absorbed.

The ion density of the D-layer at its maximum is $N_e = 10^{10}$ / cubic meter (Marcel, 2002).

2.2.2.2. The E layer

The E region is situated about 100 to 125 km up. The E-layer is mainly ionized by the soft X-rays and also by EUV (Extreme Ultra Violet). It is a thin layer from 5 to 10 km thick. During daytime hours, the ionization characteristics are practically similar to those of the D region: the greatest ionization takes place near local noontime and mostly disappears at night. Depending on latitude, summer or wintertime, the E-layer will nearly completely disappear during the night or still exist with a very weak ionization grade. Experiments in the early 1980's, during the peak of solar cycle 21, revealed that the E-layer did not go totally away at night, but in fact sometimes was an exceptional or efficient source of nighttime propagation. Ionization increases rapidly after sunrise, drops off quickly after sundown, with the maximum around noontime and the minimum after midnight, all in local time.

Sometimes the E-layer also displays another amazing phenomenon named sporadic E (Es). In this layer, we can have areas of localized and sporadically intense ionization, occurring between about 100 and 115 km with a peak near 105 km. The critical frequency of the E-layer is mostly between 1.5 and 4 MHz: higher during a sunspot maximum than during a sunspot minimum. The critical frequency of sporadic E can exceptionally reach to about 30 MHz. (We shall learn more about the critical frequency later.) Because this region is more rarified than the D-layer, the recombination factor is also a bit lower. Therefore, the electron density is higher, and the decrease after sunset is not so sudden.

The ion density of the E-layer at its maximum is $N_e = 10^{11}$ / cubic meter (Marcel, 2002).

2.2.2.3. The F layer

From approximately 150 km height, we encounter the third region. This layer is the most interesting one for our long distance communications. The F-layer is ionized by Extreme ultraviolet light (EUV) and high ultra violet. During daylight, it splits the layer into two parts. The lower part starts at about 150 km altitude and becomes the F1-layer. The higher portion starts at about 200 km altitude and becomes the F2-layer. The given heights are not to be taken as absolute; they vary continuously.

The ion density of the F-layer at its maximum is $Ne = 10^{12}$ / cubic meter (Marcel, 2002).

2.2.2.4. The F1 layer

The F1 layer is situated at height of 140–210 km. The layer F1 is defined based on an inflection or a peak in the curve electron density around 180 km. The main source of ionization is extreme ultraviolet (EUV) solar radiation in the wavelengths $\lambda \approx 58.4$ and 30.4 nm. In the F1-region, the main primary ions which are produced directly by photoionization are O^+ and N_2^+ . The most numerous is the atomic oxygen ion O^+ . The most numerous is the atomic oxygen ion O^+ . Since atomic oxygen ion rarely losses its charge by the radiative recombination, indirect dissociative recombination is carried out in case of the F1-region. While in case of the E-region, dissociative recombination is carried out directly. This is the distinguishing feature between the E- and F1-regions.

The height of F1 depends on solar activity, season, and geomagnetic activity. Accordingly, the F1 layer is more pronounced in summer than in winter always disappears during the night and sometimes in winter even during the day. Under those conditions the F1 and F2 layers form a single portion of the ionospheric F region.

2.2.2.5. The F2 layer

The F2 layer is the most important layer of the ionosphere. It present 24 h a day under all solar-terrestrial conditions. This is the region between roughly 200 km to 600 km which has the greatest concentration of electrons. The F2-region is the most important region from navigation and space communication point of view. It is also the region which is the most variable and the most irregular from prediction point of view. The main characteristics of the F2 layer are its high variability, on timescales ranging from the 11 years of a solar cycle and even longer, to a few seconds during strong interactions with the plasmasphere above (at altitudes $>1\ 000$ km) depending on solar-terrestrial conditions. Its formation is predominantly dependent of the winds and its concentration varies with solar activity. The highest concentration of free electrons can be observed during the day, especially during local noon. During the night, this concentration decreases, but the layer remains due to low recombination of ion with neutral and wind transport effects. The F2 region has a peak near 300 km during the day and at higher altitudes at night. Shortly after sunset, the absolute density near the peak of the F region often increases due to plasma transport processes before decreasing to a night time value.

2.2.2.6. Topside ionosphere

This part of the Ionosphere starts at the height of the maximum density of the F2 layer of the Ionosphere and extends upward with decreasing density to a transition height where O⁺ ions become less numerous than H⁺ and He⁺. The transition height varies but seldom drops below 500km at night or 800km in the daytime, although it may lie as high as 1100km. Above the transition height, the weak ionization has little influence on radio signals.

Above the topside region, there is a region where the lighter ions (Hydrogen H⁺ and Helium He⁺) dominate. This region of ionosphere is effectively fully ionized, is called the plasmasphere or the protonosphere. The boundary between the topside and protonosphere regions is defined as the transition from atomic oxygen to atomic hydrogen as the primary ion constituent. This transition occurs at an altitude roughly 600 to 2000 km.

2.2.2.7. Plasmasphere

The Earth's plasmasphere is an inner part of the magnetosphere. It is located just outside the upper ionosphere located in Earth's atmosphere. It is a region of dense, cold plasma that surrounds the Earth. Although plasma is found throughout the magnetosphere, the plasmasphere usually contains the coldest plasma. Here's how it works:

The upper reaches of our planet's atmosphere are exposed to ultraviolet light from the Sun, and they are ionized with electrons that are freed from neutral atmospheric particles. The results are electrically charged negative and positive particles. The negative particles are electrons, and the positive particles are now called ions (formerly atoms and molecules). If the density of these particles is low enough, this electrically charged gas behaves differently than it would if it were neutral. Now this gas is called plasma. The atmospheric gas density becomes low enough to support the conditions for the plasma around earth at about 90 kilometers above Earth's surface.

Because of space weather storms this cold and dense plasmaspheric plasma can actually end up all over the place. Generally, that region of space where plasma from the ionosphere has the time to build up to become identified as the plasmasphere rotates or nearly rotates with the Earth. That region shrinks in size with increased space weather activity and expands or refills during times of inactivity. As it shrinks with increasing activity, some of the plasmasphere is drawn away from its main body in the sunward direction toward the boundary in space between that region dominated by Earth's magnetic field and the much larger region dominated by the Sun's magnetic field. The region dominated by Earth's magnetic field is called the magnetosphere. The larger Sun dominated region is called the heliosphere.

2.2.3. Major Geographic Regions of the Ionosphere

In addition to the variation of the plasma density with altitude, the ionosphere also shows important changes with time of day, latitude, longitude, season, solar activity and geomagnetic activity. Latitudinal variation has a distinctive behavior due to the geometry of the Earth's magnetic field lines. Hence the ionosphere can be classified by three latitudes controlled by different physical processes: the low, middle and high (aurora) latitude regions.

2.2.3.1. Low latitudes

The larger fraction of solar energy is absorbed within $+30^\circ$ latitude zone centered on the equator (Abdu, 2005), so it is expected to have larger ionization at the region. However, one of the most prominent features in the ionosphere, known as equatorial anomaly, occurs at the low latitudes, given origin to depletion at equatorial latitudes and two ionizations crest at low latitudes.

The electric field configuration, which is eastward during the day, produces an upward drift ($E \times B$ drift) leading to a plasma fountain. The lifted plasma by the fountain effect then diffuses downward along the geomagnetic field lines due to the gravitational force and pressure gradient, which result in the ionization enhancement on both sides of the magnetic equator at $+15^\circ$ latitude.

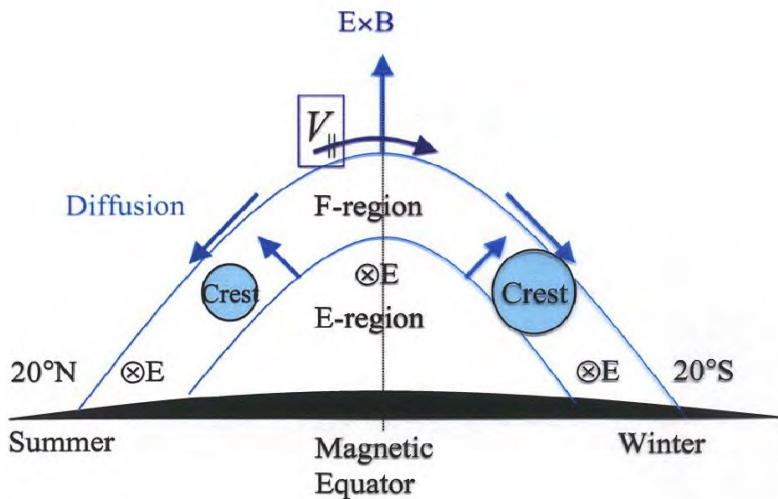


Fig.2.4. Asymmetry of the Equatorial Ionization Anomaly. E donates an eastward electric field and B is the northward geomagnetic field Scheme Anderson and Roble (1981)

The low latitude anomaly may exhibit asymmetry behavior between the northern and southern ionization crests due to an inter-hemispheric wind blowing from the summer to winter hemisphere. The behavior is represented in the Fig.2.4. In the summer hemisphere, plasma moves upward along the geomagnetic field lines, while plasma moves downward in

the winter hemisphere. Therefore, the plasma is transported from the summer hemisphere to the winter hemisphere. As a result, the equatorial anomaly crests in the winter hemisphere are generally larger than in the summer hemisphere.

2.2.3.2. Middle Latitude Ionosphere

The middle latitude ionosphere is a relatively less variable and less disturbed region and as a result of this, most of the ionosphere sensing instruments, observations and measurements are best obtained at this region. The middle latitude ionosphere region can roughly be considered as distributed from 30° to 60° on both sides of the equator.

2.2.3.3. High-Latitude Region

In addition to photoionization, collisional ionization is another source of ionization in the high-latitude region. The main reason for this is the fact, that the geomagnetic field lines are nearly vertical in this region leading to the charged particles descending to E layer altitudes (about 100 km). These particles can collide with the neutral atmospheric gases causing local enhancements in the electron concentration, a phenomenon which is associated with auroral activity. Auroral activity can also be regarded as an interaction between magnetosphere, ionosphere, and atmosphere.

2.3. Ionospheric Variability

The variations of the ionosphere can be of two general types. The first type is presented by variations, which are regular and can be predicted in advance with reasonable accuracy and the other by seasonal variations, which are irregular as a result of behaviour of the sun and can't be predicted.

2.3.1. Diurnal and Seasonal variation

Electron densities are normally higher during the day and lower at night. After dawn, solar radiation causes electrons to be produced in the ionosphere and frequencies increase rapidly to a maximum around noon. During the afternoon, electron densities begin falling due to electron loss and with darkness the D, E and F1 regions disappear. Communication during the night is by the F2 (or just F) region only and attenuation is very low. Through the night, maximum electron density gradually decreases, reaching their minimum just before dawn.

One of the factors that affect the reliability of any ionospheric prediction scheme is the large day-to-day variability of the ionosphere and this is reflected in the variations in the TEC.

Since TEC is a function of the amount of incident solar radiation, it is generally greater during the day when sunlight is present, producing ionization. On the night side of the Earth, the recombination dominates, thereby reducing the TEC.

Maximum TEC usually occurs in the early afternoon and minimum TEC usually occurs just before dawn. As a consequence, at night the ionospheric delay is approximately five to ten times less than for day time observations. Jayachandran et al (1992) founded, that the TEC variability is more a function of time of day than of solar activity. Furthermore, they also found that the variability is smaller during daytime and larger at night, at all latitudes and at both solar maximum and minimum.

2.3.2. Latitudinal Variation

As previously discussed, the TEC varies with geographic latitude. While this is partly due to changing zenith angle of the Sun, there are also effects due to the changing magnetic dip angle and it is convenient to distinguish three regions based on magnetic latitude, viz. high latitudes, mid latitudes, and low latitudes. Usually TEC is maximum at low latitudes and minimum at mid-latitudes and polar regions.

The TEC increases with decreasing latitude and usually the maximum TEC is recorded over the low-latitude region. The TEC peak at the tropical latitude region decreases as the equator is approached so that a trough like structure, known as the Equatorial Anomaly, occurs at or near the magnetic equator, and this trough becomes more pronounced during severe magnetic disturbances.

Ion production by solar EUV radiation and X-rays is relatively weak because of the low elevation of the Sun, and energetic charged particles are the main contributors to ion production at high-latitudes. The polar ionosphere at geomagnetic latitudes greater than about 75° is also the region, where most of the solar wind energy is dissipated and where this dissipation often dominates the total upper atmospheric energy budget. The energy is redistributed by heating and cooling, winds and waves.

2.3.3. Solar Cycle Variation

Ultraviolet radiation from the Sun is primarily responsible for the ionosphere existence. The UV output of the Sun varies with solar activity, with a clear variation with a mean period of about 11 years. Within the 11-year solar cycle period two main conditions occur; solar maximum and minimum and the TEC is much larger during solar maximum than solar minimum conditions.

One of the longest periodic variations in solar energy is a cycle averaging 11 years, corresponding to the time between reversals in the solar magnetic field. The intensity of solar radiation for long-term prediction purposes can generally be quantified by the 12-month running average R12 and solar radio flux index F10.7 or the monthly mean of their daily values.

Chapter3. Modelling the ionosphere

There are various criteria which have to be taken into account for the developing of an ionosphere model. The most important are: the choice for input data and the formulation of mathematical or physical descriptions for the parameter state and variations of the ionosphere.

3.1. Categorization of models

All ionosphere models can be categorized as climatological representations, which reflect the regular variability of the ionosphere depending on the geographical location, solar activity and seasonal variations. Two of the ionospheric irregularities are hardly taken into account by most models. These are TIDs and solar storms. All models have empirical nature driven by ionospheric sounding measurements. Also they include advanced physical mechanisms capable to describe ionospheric process interactions at the expense of an increased processing effort. Besides, there are hybrid models, which try to find a compromise between physics and the processing of measurements. Three fundamental model types are shown on Figure (3.1).

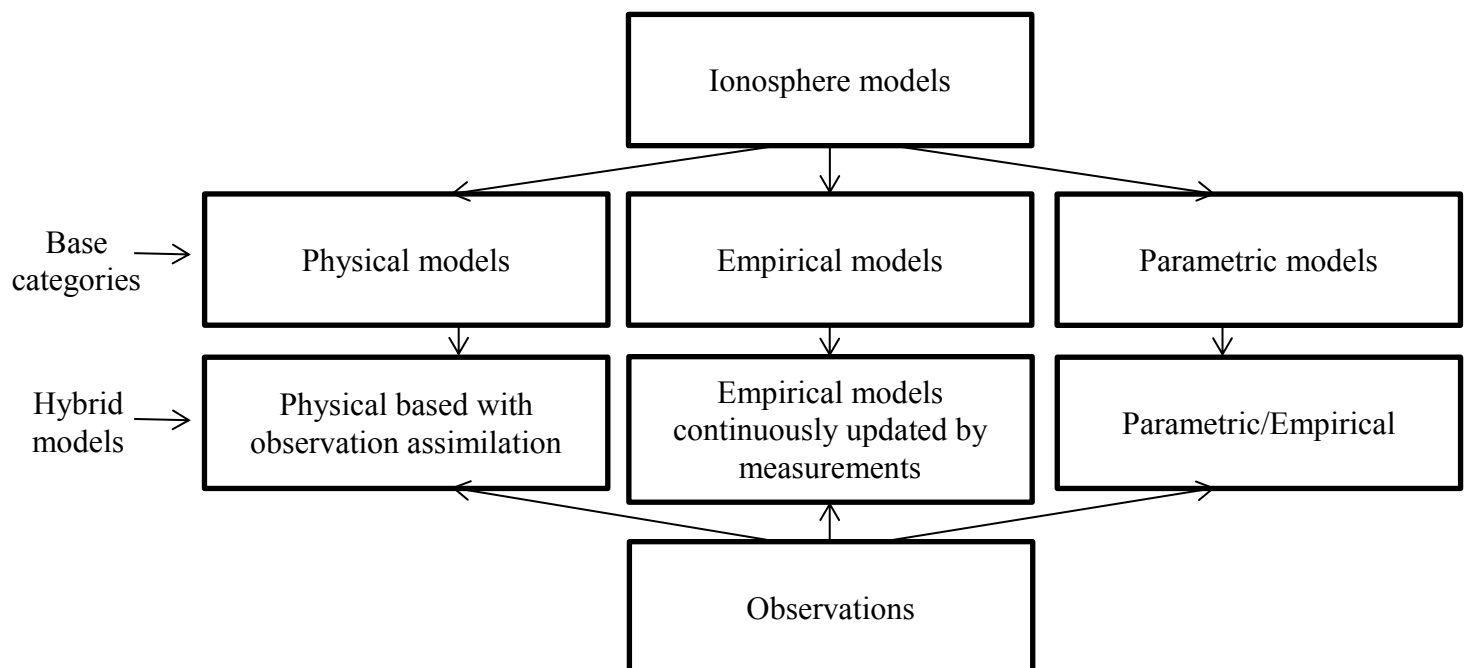


Fig.3.1. Three fundamental ionosphere model types (Marco Limberger, 2015)

Physical models

In physical models are taken into account physical laws and principles (continuity, energy and momentum equations) and they need to be solved by partial differential equations.

These models theoretically allow to detect ionospheric irregularities and to describe Sun-Earth interactions. But the processing effort is high, in particular for global modeling,

making physical models rather unsuitable for operational applications and most geodetic purposes.

Typical physical models are:

- the Time Dependent Ionospheric Model (TDIM) (1986)
- the Coupled Thermosphere-Ionosphere Model (CTIM) (1987)
- the Field Line Interhemispheric Plasma Model (FLIP) (1988)

Empirical models

The second class of models is called empirical. They use measurements, that are provided from one or more multiple observation systems during a long period of time in the past, which must at least cover the minimum and maximum solar radiation. The central role for empirical models plays the aspect of having a sufficient data sensitivity, coverage and sampling to capture at least regular ionospheric structures. As a rule, a set of model coefficients for the description of spatial-temporal ionospheric climatology is determined from the set of input data.

Typical empirical models are:

- the Bent model (1972)
- the International Reference Ionosphere (IRI) (2011)
- Neustrelitz Peak Density Model (NPDM) (2011)

Neustrelitz Peak High Model (NPHM) (2011)

Parametric models

Parametric models are used simple analytic functions for extensive physical computations. These models are simplification of physical models.

Typical parametric models are:

- the Fully Analytical Ionospheric Model (FAIM) (1989)
- the Parameterized Ionospheric Model (PIM) (1995)

Hybrid models

Hybrid models represent the regular ionospheric structures and can resolve irregularities in case they are detected by the assimilated observations. In hybrid models the time delay depends mainly on the measurement availability and the processing effort.

Examples of hybrid models are:

- The Tomographic Ionosphere Model (TOMIOM) (1999)
- JPL model (1999)

- The Electron Density Assimilative Model (EDAM) (2008)
- NeQuick model (2009)
- The Neustrelitz TEC Model (NTCM) (2011)

Empirical modeling including empirical model for the total electron content (TEC) is important for the study of the ionosphere and practical applications. For our research we will use three ionospheric models: the quick run model NeQuick, NPDM (Neustrelitz Peak Density Model) and NPHM (Neustrelitz Peak High).

3.2. NPDM (Neustrelitz Peak Density Model)

The peak electron density of the F2 layer NmF2 is a key parameter for characterizing the ionosphere. Hoque and Jakowski (2012) presented an empirical model approach that allows determining global NmF2 with a limited number of model coefficients. The non-linear approach needs 13 coefficients and a few empirically fixed parameters for describing the NmF2 dependencies on local time, geographic/geomagnetic location and solar irradiance and activity. The model approach is applied to a vast quantity of global NmF2 data derived from GNSS radio occultation measurements by CHAMP, GRACE and COSMIC satellite missions and about 60 years of processed NmF2 data from 177 worldwide ionosonde stations. The NPDM is climatological, i.e., the model describes the average behaviour under quiet geomagnetic conditions. A preliminary comparison with the electron density NeQuick model reveals similar results for NmF2 with RMS deviations in the order of $2 \times 10^{11} \text{ m}^{-3}$ and $5 \times 10^{11} \text{ m}^{-3}$ for low and high solar activity conditions, respectively.

The different terms describing the dependencies from local time, season, geomagnetic field and solar activity are combined in a multiplicative way as

$$NmF2 = F_1 F_2 F_3 F_4 F_5 \quad (1)$$

The main dependencies of NmF2 are described by the factors F_i which contain explicitly the model functions and coefficients. The variation with local time (LT in hours) is splitted into diurnal (D), semi-diurnal (SD) and ter-diurnal (TD) harmonic components. The model function describing the local time variation is given by F_1 as

$$F_1 = \cos \chi^{***} + (c_1 \cos(V_D) + c_2 \cos(V_{SD}) + c_3 \sin(V_{SD}) + c_4 \cos(V_{TD}) + c_5 \sin(V_{TD})) \cdot \cos \chi^{**} + c_6 BO \quad (2)$$

where the angular phases of the diurnal, semi-diurnal and ter-diurnal variations V_D , V_{SD} and V_{TD} are defined by

$$V_D = \frac{2\pi(LT - LT_D)}{24} \quad (3)$$

$$V_{SD} = \frac{2\pi LT}{12} \quad (4)$$

$$V_{TD} = \frac{2\pi LT}{8}, \quad (5)$$

respectively. The daily maximum of NmF2 occurs at 14 LT instead of at 12 LT for most cases. Therefore, we take the phase shift $LT_D = 14$ hours in Eq. (3). The solar zenith angle χ dependency is considered by the following expressions.

$$\cos \chi^* = \sin \varphi \sin \delta + \cos \varphi \cos \delta \quad (6)$$

$$\cos \chi^{**} = \cos \chi^* - \frac{2\varphi}{\pi} \sin \delta \quad (7)$$

$$\cos \chi^{***} = \cos \chi^* + P_{F1} \quad (8)$$

where φ is the geographic latitude and δ is the declination of the sun (all angles in radians). The dependency on the solar zenith angle has been described by three functions $\cos \chi^*$, $\cos \chi^{**}$ and $\cos \chi^{***}$. The function $\cos \chi^*$ is the expression of the solar zenith angle at local noon given by Davies [page 64, 1990]. The value $P_{F1} = 0.4$ in Eq. (8) is chosen in such a way that the term $\cos \chi^{***}$ has always a positive contribution. The so called summer day time bite out (BO) effect in the mid latitude is modelled by the following functions.

$$BO = \exp\left(-\frac{(|\varphi| - \varphi_{BO})^2}{2\sigma_{BO1}^2}\right) \cos\left(\frac{2\pi(doy - doy_{BO})}{365.25}\right) \exp\left(-\frac{(LT - LT_{BO})^2}{2\sigma_{BO2}^2}\right) \frac{\varphi}{|\varphi|} \quad (9)$$

In which

$$LT_{BO} = 13 + 1.5 \cos \left(\frac{2\pi(doy - doy_{BO})}{365.25} \right) \frac{\varphi}{|\varphi|} \quad (10)$$

The parameters determining corresponding geographic latitude and day of year are set as $\varphi_{BO} = 45^\circ$ and $doy_{BO} = 181$, respectively (Hoque M. M., Jakowski N. (2011)). The half widths of Gaussian functions are best fitted as $\sigma_{BO1} = 14^\circ$ and $\sigma_{BO2} = 3$ hours. The seasonal variation of NmF2 is modelled by two components: the annual (A) and the semi-annual (SA) variation by the following expression.

$$F_2 = 1 + c_7 \cos(V_A) + c_8 \cos(V_{SA}) \quad (11)$$

In which

$$V_A = \frac{2\pi(doy - doy_A)}{365.25} \quad (12)$$

$$V_{SA} = \frac{4\pi(doy - doy_{SA})}{365.25} \quad (13)$$

The phase shifts with respect to the beginning of the year are found to be $doy_A = 18$ days and $doy_{SA} = 6$ days for the annual and semi-annual variation, respectively. The geomagnetic field dependency is given by the geomagnetic latitude φ_m dependency

$$F_3 = 1 + c_9 \cos \varphi_m \quad (14)$$

The two ionization crests are modelled by the following expression:

$$F_4 = 1 + c_{10} \exp(EC_1) + c_{11} \exp(EC_2) \quad (15)$$

In which

$$EC_1 = -\frac{(\varphi_m - \varphi_{c1})^2}{2\sigma_c^2} \quad (16)$$

$$EC_2 = -\frac{(\varphi_m - \varphi_{c2})^2}{2\sigma_c^2} \quad (17)$$

$$\sigma_c = 20 - 10 \exp\left(-\frac{(LT-14)^2}{2\sigma_{cLT}^2}\right) \quad (18)$$

where φ_{c1} and φ_{c2} are the northward and southward crests at 16°N and -15°N , respectively. The corresponding half widths are found to be the same and equal to σ_c given by Eq. (18) in which $\sigma_{cLT} = 12$ hour. The strong solar activity dependence of the NmF2 is formulated by

$$F_5 = c_{12} + c_{13} * F10.7 \quad (19)$$

where $F10.7$ is the solar radio flux in flux units ($1 \text{ flux units} = 10^{-22} \text{ Wm}^{-2}\text{Hz}$) and the parameter $\delta_{F10.7}$ is best fitted as $\delta_{F10.7} = 12$. The $F10.7$ is the main driving parameter of the NPDM.

3.3. NPHM (Neustrelitz Peak Height Model)

The F2-layer peak density height $hmF2$ is one of the most important ionospheric parameters characterizing HF propagation conditions. For global $hmF2$ modelling Hoque and Jakowski (2013) present a nonlinear model approach with 13 model coefficients and a few empirically fixed parameters called Neustrelitz Peak Height Model (NPHM). The model approach describes the temporal and spatial dependencies of $hmF2$ on global scale. For determining the 13 model coefficients this model approach is applied to a large quantity of global $hmF2$ observational data obtained from GNSS radio occultation measurements onboard CHAMP, GRACE and COSMIC satellites and data from 69 worldwide ionosonde stations. The NPHM consists of a set of nonlinear equations describing the dependencies of $hmF2$ on local time, season, geomagnetic field and solar activity as

$$hmF2 = F_1 F_2 F_3 F_4 \quad (20)$$

Where the factors $F_1 - 4$ contain explicitly the model functions including model coefficients which describe four main dependencies of $hmF2$. The factor F_1 describes the daily variation with local time (LT in hours) as

$$F_1 = 1 + c_1 \cos \chi^{**} + \left(\begin{array}{l} c_2 \cos(V_D) + c_3 \sin(V_D) + c_4 \cos(V_{SD}) \\ + c_5 \sin(V_{SD}) + c_6 \cos(V_{TD}) + c_7 \sin(V_{TD}) \end{array} \right) \cos \chi^* \quad (21)$$

$$V_D = \frac{2\pi LT}{24}, \quad V_{SD} = \frac{2\pi LT}{12}, \quad V_{TD} = \frac{2\pi LT}{8} \quad (22)$$

Where V_D , V_{SD} and V_{TD} are the angular phases of the diurnal, semi-diurnal and ter-diurnal harmonic components, respectively. The functions $\cos\chi^*$ and $\cos\chi^{**}$ describe the dependency on the solar zenith angle χ as

$$\cos\chi^* = \sin\varphi\sin\delta + \cos\varphi\cos\delta - \frac{2\varphi}{\pi}\sin\delta \quad (23)$$

$$\cos\chi^{**} = \sin\varphi\sin\delta + \cos\varphi\cos\delta + P_{F1} \quad (24)$$

Where φ is the geographic latitude and δ is the declination of the sun. The value $P_{F1} = 0.4$ in Eq. (11) is chosen in such a way that the term $\cos\chi^{**}$ has always a positive contribution. The factor F_2 describes the annual (A) and the semi-annual (SA) variation of hmF2 as given by Eq. (12).

$$F_2 = 1 + c_8 \cos(V_A) + c_9 \cos(V_{SA}) \quad (25)$$

In which

$$V_A = 2\pi \frac{(doy - doy_A)}{365.25}, \quad V_{SA} = 4\pi \frac{(doy - doy_{SA})}{365.25} \quad (26)$$

The phase shifts are best fitted as $doy_A = 181$ days and $doy_{SA} = 49$ days for the annual and the semi-annual variation, respectively.

There is a geomagnetic control over the structure of the peak electron density and its height. Therefore, the peak height depends on the geomagnetic latitude φ_m . For simplicity it was used a simple dipole representation of the Earth's magnetic field instead of using any multi-pole representation such as the International Geomagnetic Reference Field (IGRF) model (Mandea and Macmillan, 2000). The latitudinal distribution of hmF2 shows a maximum at the geomagnetic equator gradually decreasing on both sides of the equator. This investigation shows that the peak over the geomagnetic equator is prominent during daytime but becomes weaker during night time. This modelling latitudinal distribution of hmF2 in connection with the local time variation in such a way that the magnitude of hmF2 peak is maximum at 14 LT and minimum during night time. Thus, the latitudinal distribution of hmF2 is modelled by the following expression:

$$F_3 = 1 + c_{10} \exp\left(-\frac{\varphi_m^2}{2\sigma_{\varphi1}^2}\right) + c_{11} \exp\left(-\frac{\varphi_m^2}{2\sigma_{\varphi2}^2}\right) \exp\left(-\frac{(LT - 14)^2}{2\sigma_{LT}^2}\right) \quad (27)$$

The half widths of the Gaussian function are best fitted as $\sigma_{\phi 1} = 40^\circ$, $\sigma_{\phi 2} = 20^\circ$ and $\sigma_{LT} = 4$ hour.

The strong solar activity dependence of hmF2 is represented by the next equation.

$$F_4 = c_{12} + c_{13} \exp\left(-\frac{F10.7}{\delta_{F10.7}^2}\right) \quad (28)$$

Where F10.7 is the solar radio flux commonly measured in flux units (1flux unit 10^{-22} Wm $^{-2}$ Hz $^{-1}$) and $\delta_{F10.7} = 10.8$ flux units.

Equations (7- 15) explicitly describe the functional dependencies of hmF2 on local time, season, geographic and geomagnetic latitudes, and solar cycle variations. The equations contain 13 unknown polynomial coefficients in addition to a few empirically fixed known parameters.

3.4. NeQuick (quick-run ionospheric electron density model)

All empirical models can be as for global and as regional use. NeQuick is a quick run model for ionospheric applications. This model is incorporated in Galileo receivers [Galileo Information Center, 2006] and the model coefficients are broadcasted as part of the Galileo navigation message. NeQuick has also been adopted as an ITU standard [ITU-R, 2007]. It was developed by the Aeronomy and Radio Propagation Laboratory (ARPL) of the International Centre for Theoretical Physics (ICTP) and by the Institut fur Geophysik, Astrophysik und Meteorologie (IGAM) of the University of Graz (Austria). In NeQuick basic inputs are: position, time and solar flux; the output is the electron concentration at the given location and time. This model used three anchor points: the E layer peak, the F1 peak and the F2 peak, which can be modelled by using the ionosonde parameters (foE, foF1, foF2 and M(3000)F2). All these values can be modelled or experimentally derived. In NeQuick the topside electron density N(h) is represented as a semi-Epstein layer with a height-dependent thickness parameter. The thickness parameters take different values for the bottom side and for the topside of the layers. For the E-layer the thickness parameter take values B_{Ebot} and B_{Etop} and for the F₁-layer – B_{F1bot} and B_{F1top} (3.23-3.27).

$$B_{Ebot} = 5 \quad (3.23)$$

$$B_{Etop} = \max(0.5(hmF1 - hmE), 7) \quad (3.24)$$

$$B_{F1bot} = 0.5(hmF1 - hmE) \quad (3.25)$$

$$B1_{top} = 0.3(hmF2 - hmF1) \quad (3.26)$$

$$B2_{bot} = \frac{0.385NmF2}{(\frac{dN}{dh})_{max}} \quad (3.27)$$

The thickness parameter can be presented by the next equation (3.28):

$$N(h) = \frac{4NmF2}{(1+\exp(z))^2} \exp(z) \quad (3.28)$$

Where z is:

$$z = \frac{h-hmF2}{H_0 \left[1 + \frac{rg(h-hmF2)}{rH_0 + g(h-hmF2)} \right]} \quad (3.29)$$

$r = 100$ and $g = 0.125$ are constant parameters and the scale factor H_0 is defined by equation (3.30):

$$H_0 = \frac{kB2_{bot}}{v} \quad (3.30)$$

Where $B2_{bot}$ is the thickness parameter of the bottom side, k is restricted to $2 \leq k \leq 8$:

- from October to March :

$$k = -7.77 + 0.97 \left(\frac{hmF2}{B2_{bot}} \right)^2 + 0.153NmF2 \quad (3.30)$$

- from April to September:

$$k = 6.705 - 0.014R12 - 0.008hmF2 \quad (3.31)$$

In equations (3.30-3.31) $NmF2$ is given in 10^{11} m^3 , $hmF2$ and $B2_{bot}$ in km and R_{12} is monthly-mean sunspot number.

A quick-run ionospheric electron density model is only useful up to 1000 km. During the night solar activity is very low, that's why some problems can occur.

NeQuick is used for:

- computation ionospheric delays in the Raw Data Generation (RDG) capability of the Galileo System Simulation Facility (GSSF);
- computation the background ionosphere in the Global Ionospheric Scintillation Model (GISM);
- ionospheric corrections in the single frequency operation of the European GALILEO satellite navigation system.

Chapter4. Data resources

4.1. IPS (The Ionospheric Prediction Service)

The Ionosphere Prediction Service (IPS) is a project funded by the European Commission. The main function of the IPS is monitoring ionospheric activity and informing GNSS users, when an upcoming event could disrupt GNSS signals and applications.

The Ionospheric Prediction Service manages the World Data Centre (WDC) for Solar-Terrestrial Science (STS) in Sydney. IPS contributes for users the ionosonde and solar data. The main role of IPS is providing observations and predictions of minimum and maximum ionospheric electron density to support ionospheric based communications. IPS provides near real time nowcasts of HF conditions using a global network of ionosondes. For our research we have used data from the 14 IPS stations (Table 4.1.).

Table 4.1. Station coordinates (IPS)

	Station	Latitude	Longitude	Period
1	alicesps	-23.86	133.83	1985
2	brisbane	-27.53	152.92	1950-2009
3	camden	-34.05	150.67	1980-1984
4	canberra	-35.32	149.00	1950-2009
5	cocos	-12.20	96.80	1961-2009
6	darwin	-12.45	130.95	1982-2009
7	hobart	-42.92	147.32	1950-2009
8	learmonth	-22.30	114.10	2004-2008
9	mundaring	-31.98	116.22	1959-2007
10	norfolk	-29.03	167.97	1964-2009
11	salisbury	-34.70	138.60	1970-1989
12	tenantck	-19.65	134.25	1985
13	townsville	-19.63	146.85	1951-2009
14	watheroo	-30.30	115.90	1950-1959

```
# F10.7/fu/year/dox/US/hour,NmF2obs,NmF2model_,NmF2NeQ [el/1.e+12m^3],StnName= hobart,LatStndegN= -42.92,LongStndegE= 147.32
149 1950 1 6.00 7.93600000e-01 7.0005025050e-01 6.60536000e-01
149 1950 1 7.00 7.544160000e-01 7.0087785050e-01 6.760420000e-01
149 1950 1 8.00 6.790240000e-01 6.8098474080e-01 6.778310000e-01
149 1950 1 9.00 6.076000000e-01 6.3935614850e-01 6.606450000e-01
149 1950 1 13.00 6.428160000e-01 4.9660397760e-01 5.308710000e-01
149 1950 1 14.00 4.921560000e-01 4.7146468480e-01 4.783010000e-01
149 1950 1 15.00 3.483160000e-01 4.3632202460e-01 4.098510000e-01
149 1950 1 16.00 2.292760000e-01 3.7523012850e-01 3.395280000e-01
149 1950 1 18.00 2.977240000e-01 2.9971890360e-01 2.609350000e-01
149 1950 1 19.00 4.921560000e-01 3.3267285600e-01 2.847710000e-01
149 1950 1 20.00 6.428160000e-01 4.2257499240e-01 3.550060000e-01
152 1950 3 13.00 6.428160000e-01 5.0451477770e-01 5.475230000e-01
152 1950 3 14.00 5.566360000e-01 4.7889870170e-01 4.933380000e-01
152 1950 3 15.00 4.921560000e-01 4.4310275340e-01 4.225470000e-01
152 1950 3 16.00 4.028760000e-01 3.8094251930e-01 3.507150000e-01
152 1950 3 17.00 3.483160000e-01 3.2558938600e-01 2.934560000e-01
152 1950 3 18.00 4.171360000e-01 3.0411201070e-01 2.685700000e-01
152 1950 3 19.00 5.903640000e-01 3.3764668010e-01 2.907540000e-01
152 1950 3 20.00 6.790240000e-01 4.2912897450e-01 3.618570000e-01
```

Fig.4.1. Example of IPS file (NmF2)

4.2. SPIDR (Space Physics Interactive Data Resource)

The SPIDR system was an online system to search, browse and access space weather data sets archived at National Geophysical Data Center (NGDC) and the colocated World Data Center for Solar-Terrestrial Physics. But in May 2016 it was decommissioned on the ngdc.noaa.gov domain. The data sets included ionospheric data, geomagnetic data and Defense Meteorological Satellite Program (DMSP) satellite images during time period from 1950 to 2009 year.

4.3. IRO (Ionospheric radio occultation measurements)

All atmospheric parameters are based on satellite measurement of Global Navigation Satellite System (GNSS) signals. The GPS signal is influenced by the ionosphere and neutral atmosphere because the refractive index is not constant and the path is bent due to the refractive index gradients in the atmosphere.

Radio Occultation is a relative new method for indirect measurement of atmospheric parameters, such as temperature, pressure, water vapor in the troposphere and stratosphere. It is based on using the radio signals broadcasted from the Global Navigation Satellite System satellites, which are orbiting the Earth at the altitude of about 20 000 km above the surface. One of the main factors, which influence the GNSS radio signals, is the electron density in the ionosphere.

Various radio occultation missions have achieved varying degrees of performance according to their design and implementation:

Radio occultation missions:

- On 3rd of April 1995 was tested for the first time the GPS radio occultation technique with the launch of the GPS/MET mission. It was managed by the University Corporation of Atmospheric Research (UCAR). GPS/MET satellite had a limited memory on-board and not enough coverage from ground GPS stations, that's why the number of occultations obtained from it varied between 100-150 occultations per day. This mission ended on the 5th of May 1995.
- Challenging Mini-Satellite Payload (CHAMP) was a small satellite mission for geoscientific and atmospheric research. It was managed by GFZ (Deutsches GeoForschungsZentrum). This mission became the most significant data provider for the International Decade of Geopotential Research. For the first time simultaneously high-precision gravimetric and magnetic field measurements over a period of over 10 years were generated. Also both spatial and temporal variations of both fields were

recorded. CHAMP with its very good infrastructure and radio occultation measurements on board became an exemplary mission for weather forecasting, ionospheric research and space weather observation. After more than 10 years in orbit the satellite burnt up on the 19th of September 2010 over the sea of Okhotsk.

- Scientific Application Satellite-C (SAC-C) was an international cooperative Earth observation mission of Argentina, USA, Brazil, Denmark, Italy and France with CONAE (Comisión Nacional de Actividades Espaciales) of Buenos Aires (CONAE is the Space Agency of Argentina) and NASA as the main partners. This mission had started on the 21 of November 2000. The main objective was to explore the structure and dynamics of the Earth's surface, atmosphere, ionosphere and geomagnetic field.
- Gravity Recovery and Climate Experiment mission (GRACE) was a project between the National Aeronautics and Space Administration (NASA) and Deutsches Zentrum für Luft- und Raumfahrt (DLR). The main scientific goal of GRACE was measuring the Earth's gravity field and its time fluctuation with very high accuracy. This mission has ended on the 27th of October, the reason was that the spacecraft ran out of fuel.
- The ROCSat-3/COSMIC (Republic of China Satellite-3 / Constellation Observing System for Meteorology, Ionosphere and Climate) is an international collaborative project between National Space Program Office (NSPO) of Taiwan and University Corporation for Atmospheric Research (UCAR) of the United States of America. The first goal of this mission is extending the low-cost research approach of refractive GPS radio occultation measurements. The second goal is to show the benefits of atmospheric/ionospheric limb soundings in operational weather prediction, space weather monitoring and space geodesy. In USA this satellite program is known under the name of COSMIC (Constellation Observing System for Meteorology, Ionosphere and Climate).

Ionospheric radio occultation (IRO) data are very important for monitoring the ionospheric behavior on global scale for now- and forecasting the ionospheric impact on radio systems. In the present investigation we have used IRO data from COSMIC, GRACE and CHAMP.

4.4. NGDC (National Geophysical Data Center)

The National Geophysical Data Center (NGDC) is a part of the US Department of Commerce (USDOC), National Oceanic & Atmospheric Administration (NOAA), National

Environmental Satellite, Data and Information Service (NESDIS). NGDC is one of three NOAA National Data Centers (<https://www.ngdc.noaa.gov/>).

For our research we have chosen data from three stations JR055 (JULIUSRUH/RUGEN), RL052 (CHILTON) and RO041 (ROME).

Chapter 5. Model validation using ground based data (Ionosonde)

In this chapter we provide analysis of results of the recent described NPDM and NeQuick models.

For our research we have used data from the Ionospheric Prediction Service (IPS), Space Physics Interactive Data Resource (SPIDR) and National Geophysical Data Center (NGDC). We have used historical NmF2 data of 91 ionosonde stations from the Space Physics Interactive Data Resource (SPIDR) (available at <http://spidr.ngdc.noaa.gov/spidr/>) archive and 14 ionosonde stations from the Ionospheric Prediction Service (IPS). All available data from 1950 to 2010 for SPIDR and from 1950 to 2004 for IPS have been used for the selected stations.

In addition for time series analysis we have used onosonde data from three stations: JR055 (JULIUSRUH/RUGEN), RL052 (CHILTON) and RO041 (ROME).

5.1. Analysis of the peak electron density NmF2

Figures (5.1-5.24.) shows NmF2 comparisons among the Ionosonde data, NPDM results and NeQuick estimates as a function of Universal Time (UT) and Day of Year at high, mid and low geographic latitudes at different solar activity. SPIDR provides data for northern and southern hemisphere and IPS only for southern hemisphere.

Table 5.1. The validation strategy

Region	Low solar activity (F10.7 60-100 flux units)	Midium solar activity (F10.7 100-150 flux units)	High solar activity (F10.7 150-200 flux units)
60-90° N		14	
30-60° N		38	
0-30° N		16	
0-30° S		11	
30-60° S		8	
60-90° S		4	

Table 5.2. Geographic coordinates of ionosonde stations from SPIDR at high latitude

Region 60-90° North		
Station name/Id	Latitude /deg	Longitude /deg
LE061	60.1	-1.2
NU159(NURMIJARVI)	60.5	24.6
NQJ61(NARSSARSSUAQ)	61.2	-45.4

AN761(ANCHORAGE)	61.2	-149.9
YA462(YAKUTSK)	62.0	129.6
RKA64(REYKJAVIK)	64.1	-21.8
PD664(PROVIDENIYA_BAY)	64.4	-173.4
WE667(WELLEN)	66.2	-169.8
SO166(SODANKYLA)	67.4	26.6
LS168	68.0	33.0
CE669(CAPE_SCHMIDT)	68.8	179.5
NO369(NORILSK)	69.4	88.1
BW771(BARROW)	71.3	-156.8
TX471(TIKSI_BAY)	71.6	128.9

Table 5.3. Geographic coordinates of ionosonde stations from SPIDR at medium latitude

Region 30 – 60° North		
Station name/Id	Latitude /deg	Longitude /deg
YG431(YAMAGAWA)	31.2	130.6
WS832(WHITE_SANDS)	32.3	-106.5
NC136(NICOSIA)	35.1	33.2
EA036(EL ARENOSILLO)	37.1	-6.7
AN438(ANYANG)	37.4	127.0
GM037(GIBILMANNA)	37.6	14.0
AT138(ATHEENS)	38.0	23.5
LE038(LISBONNE)	38.7	-9.3
WA938(WASHINGTON)	38.7	-77.1
TB142(TBILISI)	41.7	44.8
RO041(ROME)	41.8	12.5
AA343(ALMA_ATA)	43.2	76.9
BE145(BEOGRAD)	44.8	20.5
OT945(OTTAWA)	45.4	-75.9
NK246(NOVOKAZALINSK)	45.5	62.1
SZ045(SCHWARZENBURG)	46.6	6.7
PT046(POITIERS)	46.6	0.3
BH148(BEKESCSABA)	46.7	21.2
GZ146(GRAZ)	47.1	15.5
SJJ47(ST_JOHNS)	47.6	-52.7
SC047(PARIS-SACLAY)	48.1	2.3
FR048(FREIBURG)	48.1	7.6
LN047(LANNION)	48.8	-3.4
KB548(KHABAROVSK)	48.5	135.1
KR250(KARAGADA)	49.8	73.1
PQ052(PRUHONICE)	50.0	14.6
DB049(DOURBES)	50.1	4.6
KV151(KIEV)	50.5	30.5
AD651(ADAK)	51.9	-176.6
CX452(CHITA)	52.0	113.5
DT053(DE_BILT)	52.1	5.2

MZ152(MIEDZESZYN)	52.2	21.2
PE054(ST_PETER-ORDING)	54.3	8.6
KL154(KALININGRAD)	54.7	20.6
GK156(GORKY)	56.1	44.3
SV256(SVERDLOVSK)	56.4	58.6
TK356(TOMSK)	56.5	84.9
FCJ58(FORT_CHIMO)	58.1	-68.4

Table 5.4. Geographic coordinates of ionosonde stations from SPIDR at low latitude

Region 0-30° North		
Station name/Id	Latitude /deg	Longitude /deg
SI301(SINGAPORE)	1.3	103.8
BGJ05(BOGOTA)	4.5	74.2
TM308(TRIVANDRUM)	8.5	77.0
KO310(KODAIKANAL)	10.2	77.5
DJ111(DJIBOUTI)	11.5	42.8
OU012(OUAGADOUGOU)	12.4	-1.5
MN414(MANILA)	14.7	121.1
DKA14(DAKAR)	14.8	-17.4
HA149	18.3	109.3
ND61R(NIUE)	19.1	169.9
MA720(MAUI)	20.8	-156.5
AH223(AHMEDABAD)	23.0	72.6
CD923(CUBA)	23.0	-82.0
CU322(CALCUTTA)	23.0	88.6
GB926(GRAND_BAHAMA)	26.6	-78.2
DH328(DELHI)	28.6	77.2

Table 5.5. Geographic coordinates of ionosonde stations from SPIDR at low latitude

Region 0 – 30° South		
Station name/Id	Latitude /deg	Longitude /deg
VA50L(VANIMO)	-2.7	141.3
TA90M(TALAR)	-4.6	-81.3
AS00Q(ASCENSION)	-7.9	-14.4
JI91J(JICAMARCA)	-12.1	-77.0

LPJ1O(LA_PAZ)	-16.5	-68.1
TT71P(TAHITI)	-17.7	-149.3
LR22J(LA_REUNION)	-21.1	55.9
MU12K(MADIMBU)	-22.4	30.9
JO12O(JOHANNESBURG)	-26.1	28.1
TUJ2O(TUCUMAN)	-26.9	65.4
LV12P(LOUISVALE)	-28.5	21.2

Table 5.6. Geographic coordinates of ionosonde stations from SPIDR at medium latitude

Region 30 – 60° South		
Station name/Id	Latitude /deg	Longitude /deg
MU43K(MUNDARING)	-32.0	116.4
HE13N(HERMANUS)	-34.4	19.2
SR53M(SALISBURY)	-34.7	136.8
CB53N(CANBERRA)	-35.3	149.1
CPJ3O(CONCEPCION)	-36.6	-73.0
AU63P(AUCKLAND)	-37.0	175.0
GH64L(CHRISTCHURCH)	-43.6	172.8
SGA5M(SOUTH_GEORGIA)	-54.3	-36.5

Table 5.7. Geographic coordinates of ionosonde stations from SPIDR at high latitude

Region 60 – 90° South		
Station name/Id	Latitude /deg	Longitude /deg
AIJ6N(ARGENTINE_IS)	-65.2	-64.3
MW26P(MAWSON)	-67.6	62.9
DV36Q(DAVIS)	-68.6	77.9
ZS36R(ZHONG-SHAN)	-69.4	76.4

Table 5.8. Geographic coordinates of ionosonde stations from IPS at low latitude

Region 0 – 30° South		
Station name/Id	Latitude /deg	Longitude /deg
cocos	-12.20	96.80
darwin	-12.45	130.95
townsville	-19.63	146.85
tenantck	-19.65	134.25
learmonth	-22.30	114.10

alicesps	-23.86	133.83
brisbane	-27.53	152.92
norfolk	-29.03	167.97

Table 5.9. Geographic coordinates of ionosonde stations from IPS at medium latitude

Region 30 – 60° South		
Station name/Id	Latitude /deg	Longitude /deg
watheroo	-30.30	115.90
mundaring	-31.98	116.22
camden	-34.05	150.67
canberra	-35.32	149.00
salisbury	-34.70	138.60
hobart	-42.92	147.32

All plots are generated using NPDM and NeQuick models at different latitudes during different solar activities. Also we have used filter for $NmF2_{obs}$, $0.01 \leq NmF2_{obs} \leq 15$ [1.e+12 el/m³]. For the analysis were used mean values. Local time is presented in range from 0 to 24. On the plots red color represent the ionosonde data ($NmF2_{obs}$), blue – the NPDM model ($NmF2_{mod}$), green – the NeQuick model and standard deviation (σ).

1. Model comparison at high latitude (60-90°N)
 - Low solar activity ($F10.7 = 60-100$ flux units)

SPIDR

At high latitude for diurnal variations at low solar activity, the NPDM model approximates to the ionosonde data (provided by SPIDR) better than the NeQuick model. Regarding to the seasonal variations, NeQuick model approximates to the ionosonde data better than NPDM model.

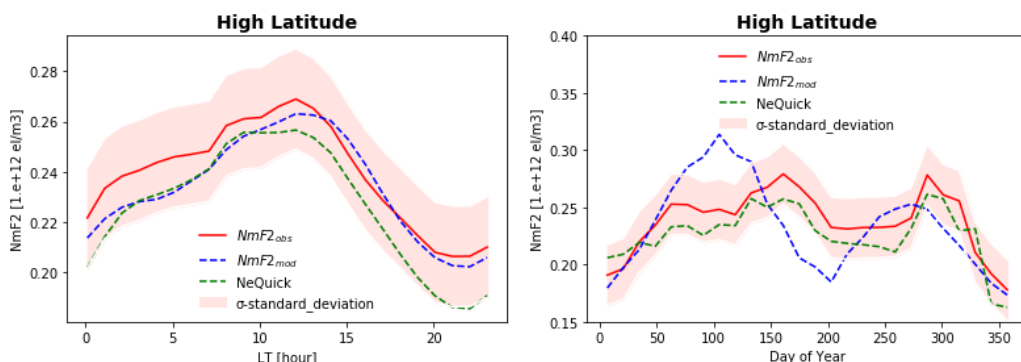


Fig.5.1. Diurnal and seasonal variations at high latitude at low solar activity

- Medium solar activity ($F_{10.7} = 100\text{-}150$ flux units)

SPIDR

At high latitude for diurnal variations at medium solar activity, the NPDM model approximates to the ionosonde data (provided by SPIDR) better than NeQuick model. And for the seasonal variations NeQuick model approximates to the ionosonde data better than NPDM model.

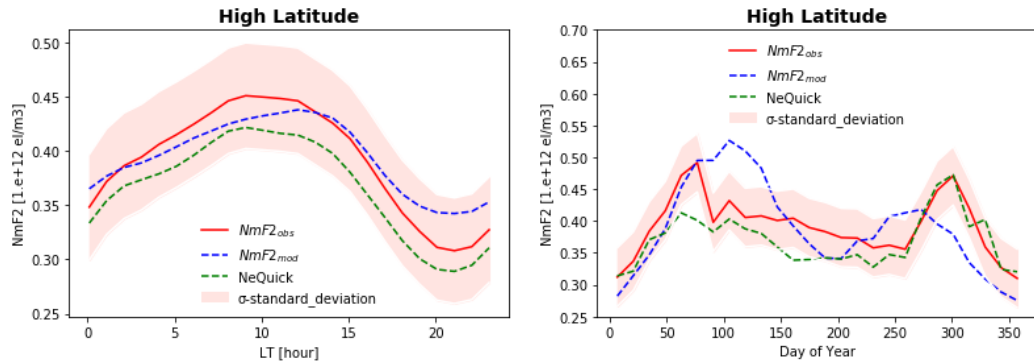


Fig.5.2. Diurnal and seasonal variations at high latitude at medium solar activity

- High solar activity ($F_{10.7} = 150\text{-}200$ flux units)

SPIDR

At high latitude for diurnal variations at high solar activity, the NeQuick model approximates to the ionosonde data (provided by SPIDR) better than NPDM model. Regarding to the seasonal variations NeQuick model approximates to the ionosonde data better.

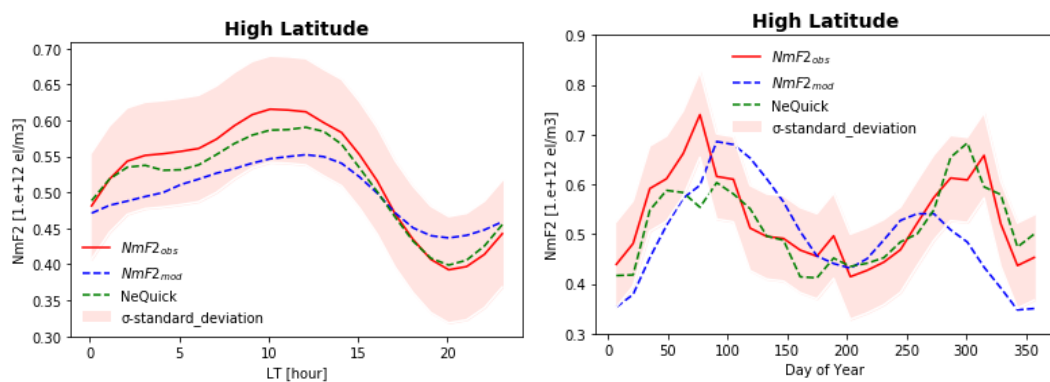


Fig.5.3. Diurnal and seasonal variations at high latitude at high solar activity

2. Model comparison at medium latitude ($30\text{-}60^\circ\text{N}$)

- Low solar activity ($F_{10.7} = 60\text{-}100$ flux units)
- SPIDR

At medium latitude for diurnal variations at low solar activity, both models are similar to the ionosonde data (provided by SPIDR). Regarding to the seasonal variations, NeQuick model approximates to the ionosonde data better.

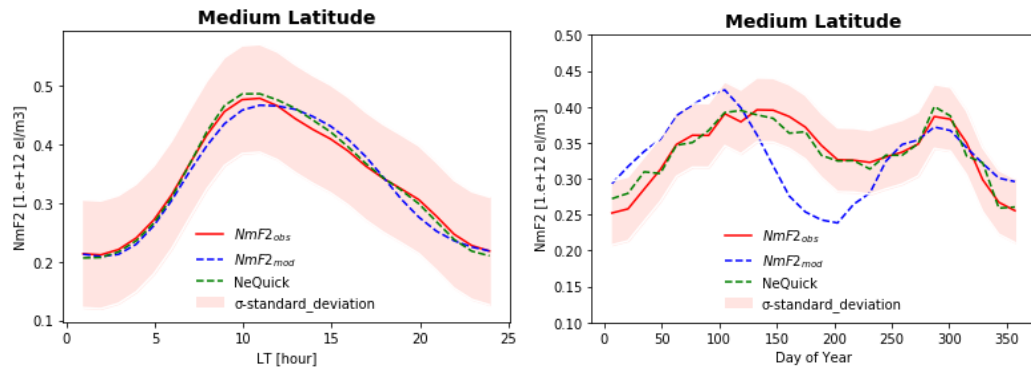


Fig.5.4. Diurnal and seasonal variations at medium latitude at low solar activity

- Medium solar activity ($F_{10.7} = 100\text{-}150$ flux units)
- SPIDR

At medium latitude for diurnal variations at medium solar activity, both models are similar to the ionosonde data (provided by SPIDR). And for the seasonal variations NeQuick model approximates to the ionosonde data better.

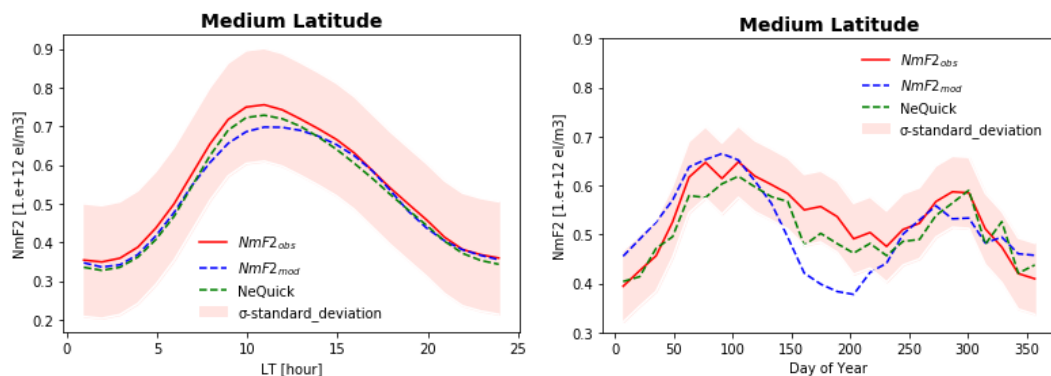


Fig.5.5. Diurnal and seasonal variations at medium latitude at medium solar activity

- High solar activity ($F_{10.7} = 150\text{-}200$ flux units)
- SPIDR

At medium latitude for diurnal variations at high solar activity, the NeQuick model approximates to the ionosonde data (provided by SPIDR) better than NPDM model. Regarding to the seasonal variations NeQuick model approximates to the ionosonde data better.

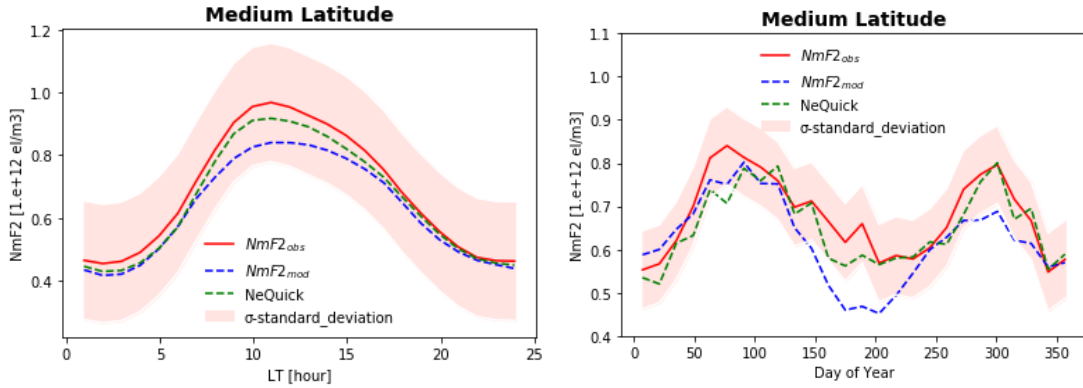


Fig.5.6. Diurnal and seasonal variations at medium latitude at high solar activity

3. Model comparison at low latitude (0-30°N)

- Low solar activity ($F_{10.7} = 60-100$ flux units)
 - SPIDR

At low latitude for diurnal variations at low solar activity, the NeQuick model approximates to the ionosonde data (provided by SPIDR) better than NPDM model. And for the seasonal variations NeQuick model approximates to the ionosonde data better too.

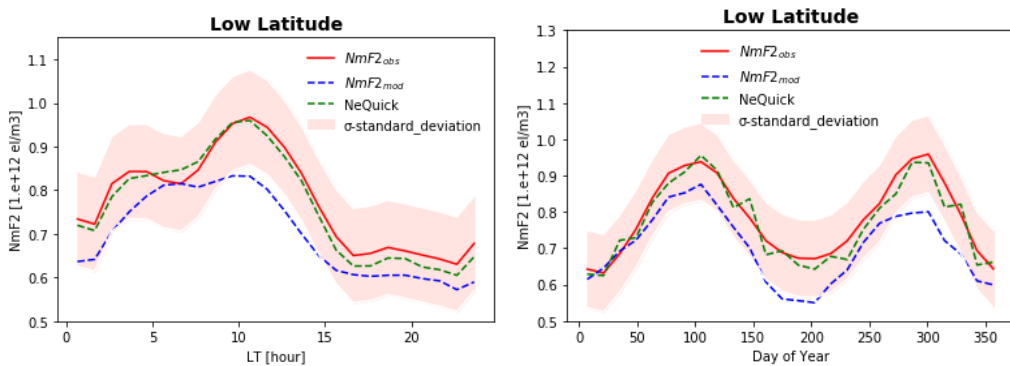


Fig.5.7. Diurnal and seasonal variations at low latitude at low solar activity

- Medium solar activity ($F_{10.7} = 100-150$ flux units)
 - SPIDR

At low latitude for diurnal variations at medium solar activity the NeQuick model approximates to the ionosonde data (provided by SPIDR) better than NPDM model. Regarding to the seasonal variations both models is similar to the ionosonde data.

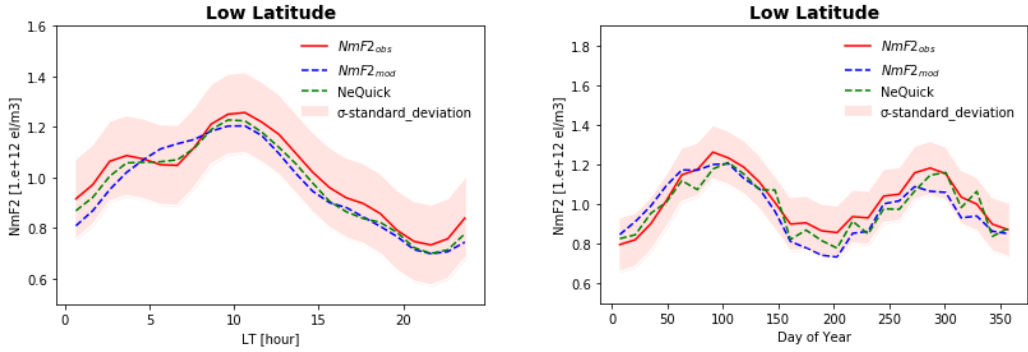


Fig.5.8. Diurnal and seasonal variations at low latitude at medium solar activity

- High solar activity ($F_{10.7} = 150\text{-}200$ flux units)

SPIDR

At low latitude for diurnal and seasonal variations at high solar activity, NeQuick and NPDM models are almost similar to the ionosonde data (provided by SPIDR).

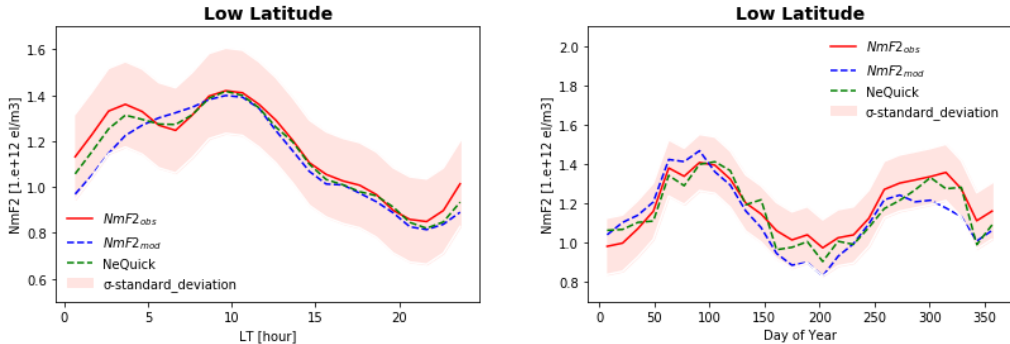


Fig.5.9. Diurnal and seasonal variations at low latitude at high solar activity

4. Model comparison at low latitude ($0\text{-}30^\circ\text{S}$)

- Low solar activity ($F_{10.7} = 60\text{-}100$ flux units)

SPIDR

At low latitude for diurnal and seasonal variations at low solar activity, the NeQuick model approximates to the ionosonde data (provided by SPIDR) better than NPDM model.

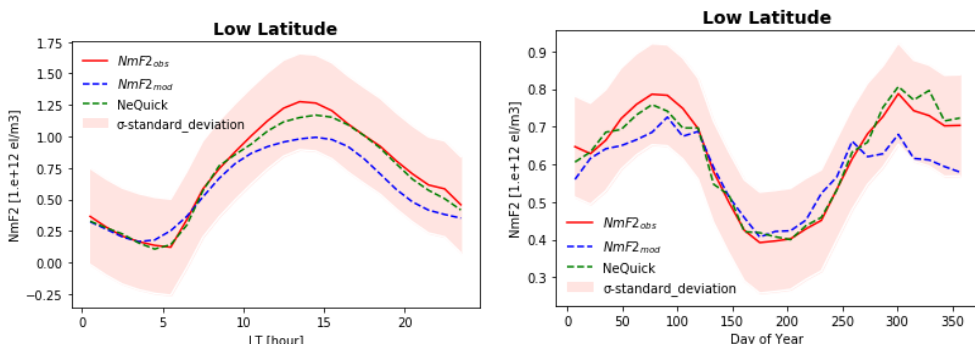


*Fig.5.10. Diurnal and seasonal variations at low latitude at low solar activity (SPIDR)
IPS*

At low latitude for diurnal variations at low solar activity, NPDM and NeQuick models are similar to the ionosonde data (provided by IPS). Regarding to the seasonal variations NeQuick model approximates to the ionosonde data better than NPDM model.

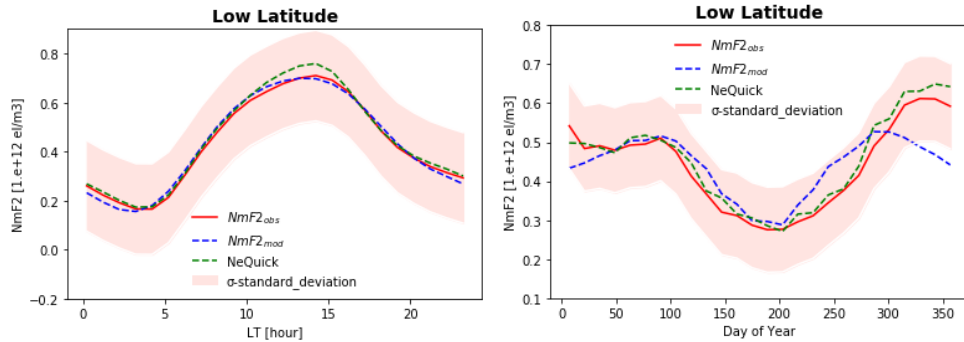


Fig.5.11. Diurnal and seasonal variations at low latitude at low solar activity (IPS)
➤ Medium solar activity ($F_{10.7} = 100\text{-}150$ flux units)
SPIDR

At low latitude for diurnal variations at medium solar activity, NeQuick model approximates to the ionosonde data (provided by SPIDR) better than NPDM model. Regarding to the seasonal variations, NPDM model approximates to the ionosonde data better than NeQuick model.

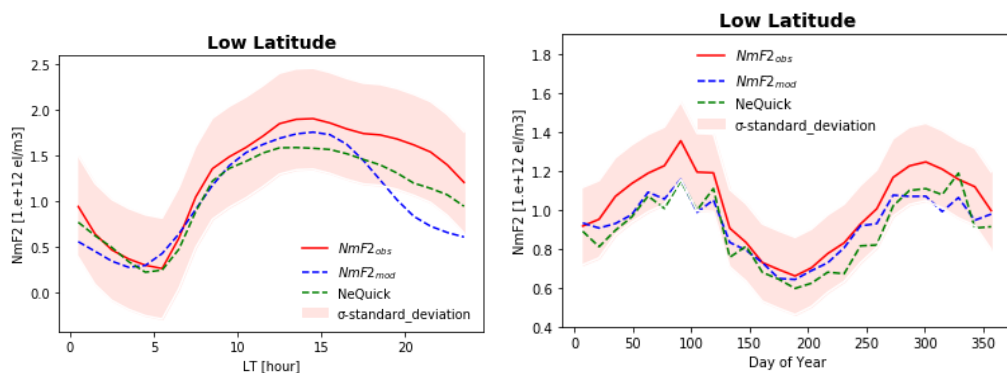


Fig.5.12. Diurnal and seasonal variations at low latitude at medium solar activity (SPIDR)

IPS

At low latitude for diurnal variations at medium solar activity, NPDM and NeQuick models are similar to the ionosonde data (provided by IPS). Regarding to the seasonal variations NeQuick model approximates to the ionosonde data better than NPDM model.

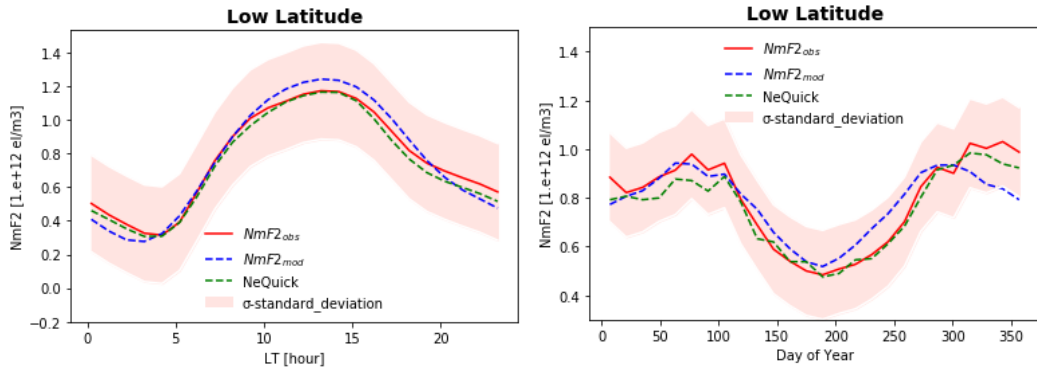


Fig.5.13. Diurnal and seasonal variations at low latitude at medium solar activity (IPS)

- High solar activity ($F_{10.7} = 150\text{-}200$ flux units)

SPIDR

At low latitude for diurnal variations, NeQuick model approximates to the ionosonde data (provided by SPIDR) better than NPDM. Regarding to the seasonal variations NPDM model approximates to the ionosonde data a little bit better than NeQuick model.

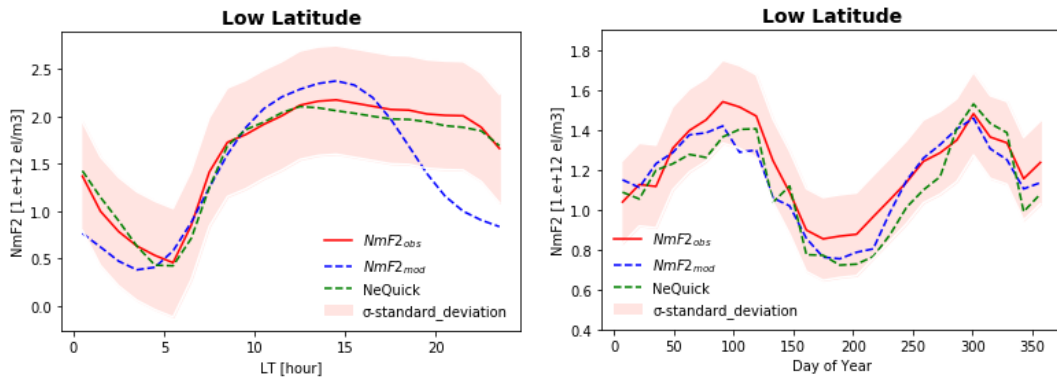


Fig.5.14. Diurnal and seasonal variations at low latitude at high solar activity (SPIDR)

IPS

At low latitude for diurnal and seasonal variations at high solar activity, NeQuick model approximates to the ionosonde data (provided by IPS) better than NPDM.

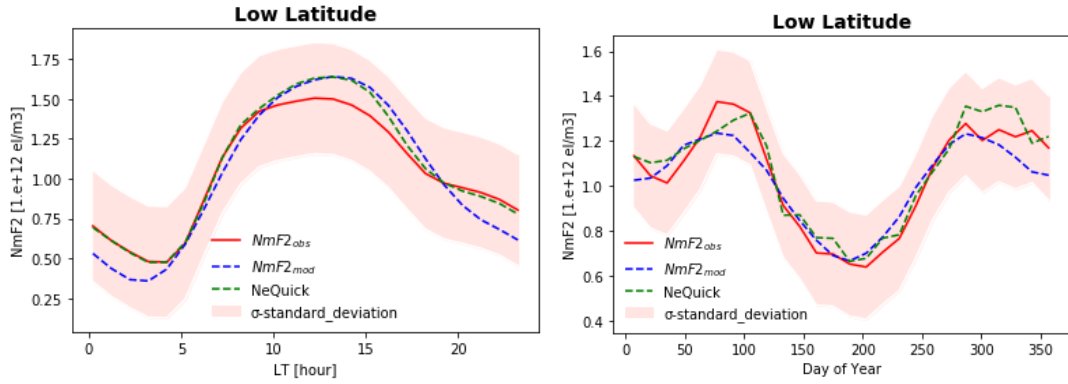


Fig.5.15. Diurnal and seasonal variations at low latitude at high solar activity (IPS)

5. Model comparison at medium latitude (30-60°S)

- Low solar activity ($F_{10.7} = 60\text{-}100$ flux units)

SPIDR

At low latitude for diurnal and seasonal variations at low solar activity, NeQuick model approximates to the ionosonde data (provided by SPIDR) better than NPDM model.

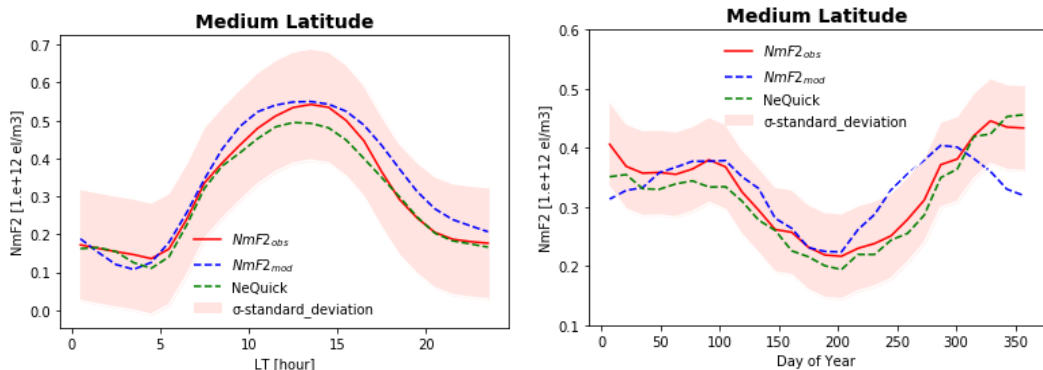


Fig.5.16. Diurnal and seasonal variations at medium latitude at low solar activity (SPIDR)

IPS

At medium latitude for diurnal variations at low solar activity both models are very similar to the ionosonde data (provided by IPS). Regarding to the seasonal variations NeQuick model approximates to the ionosonde data better than NPDM model.

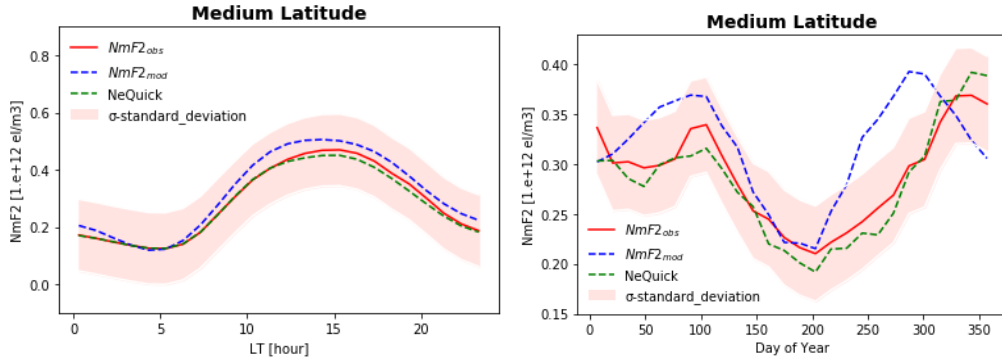


Fig.5.17. Diurnal and seasonal variations at medium latitude at low solar activity (IPS)

- Medium solar activity ($F10.7 = 100-150$ flux units)

SPIDR

At medium latitude for diurnal variations at medium solar activity, NeQuick model approximates to the ionosonde data (provided by SPIDR) better than NPHM. Regarding to the seasonal variations NPDM model approximates to the ionosonde data a little bit better than NeQuick model.

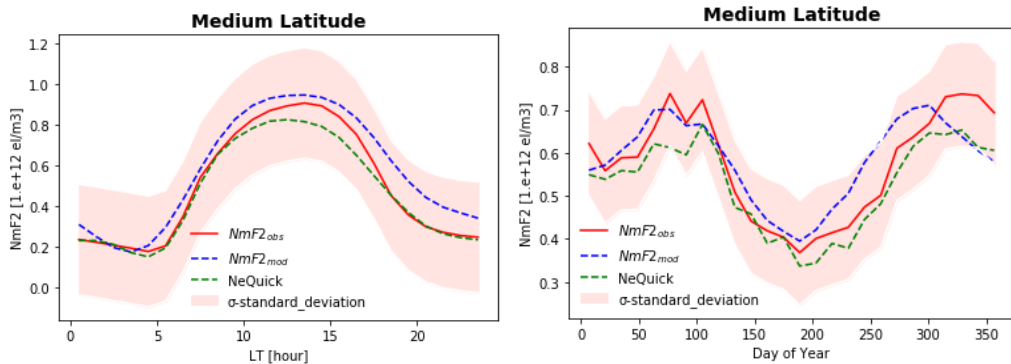


Fig.5.18. Diurnal and seasonal variations at medium latitude at medium solar activity (SPIDR)

IPS

At medium latitude for diurnal variations at medium solar activity both models are very similar to the ionosonde data (provided by IPS). Regarding to the seasonal variations NeQuick model approximates to the ionosonde data better than NPDM model.

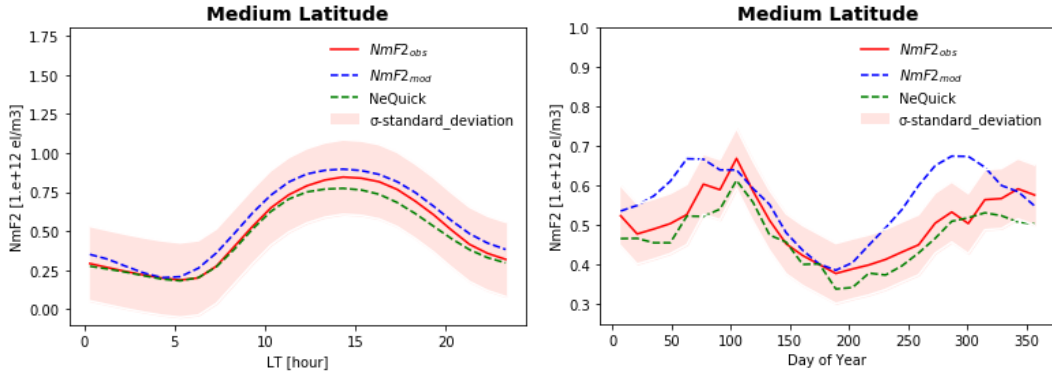


Fig.5.19. Diurnal and seasonal variations at medium latitude at medium solar activity (IPS)

- High solar activity ($F_{10.7} = 150\text{-}200$ flux units)

SPIDR

At medium latitude for diurnal variations at high solar activity both models are very similar to the ionosonde data (provided by IPS). Regarding to the seasonal variations NeQuick model approximates to the ionosonde data better than NPDM model.

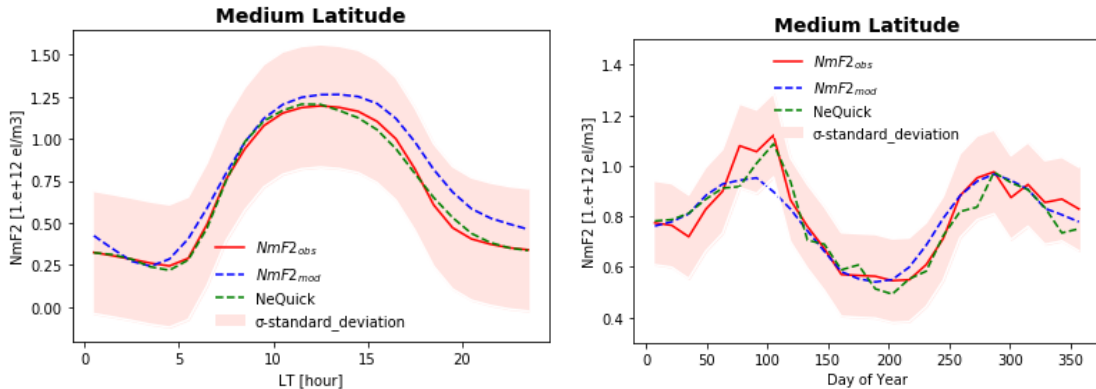


Fig.5.20. Diurnal and seasonal variations at medium latitude at high solar activity (SPIDR) IPS

IPS

At medium latitude for diurnal variations at high solar activity both models are very similar to the ionosonde data (provided by IPS). Regarding to the seasonal variations NeQuick model approximates to the ionosonde data better than NPDM model.

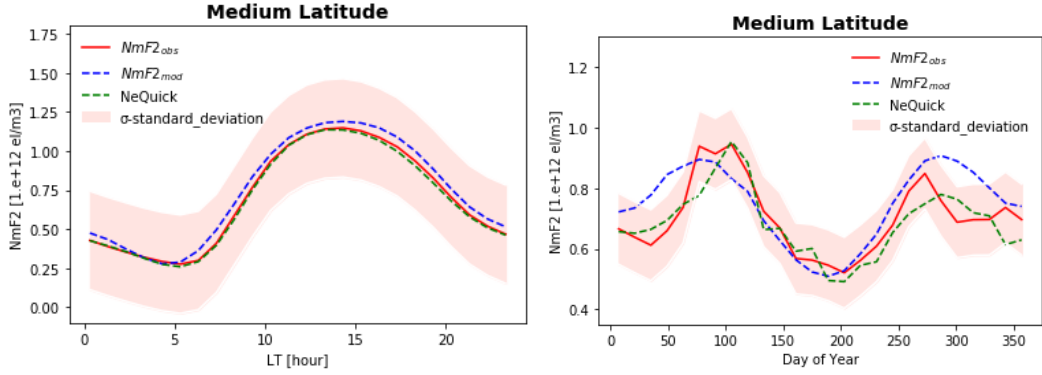


Fig.5.21. Diurnal and seasonal variations at medium latitude at high solar activity (IPS)

6. Model comparison at high latitude (60-90°S)

- Low solar activity ($F_{10.7} = 60-100$ flux units)

SPIDR

At high latitude for diurnal variations at low solar activity both models have differences to the ionosonde data (provided by SPIDR). Regarding to the seasonal variations NeQuick model approximates to the ionosonde data better than NPDM model.

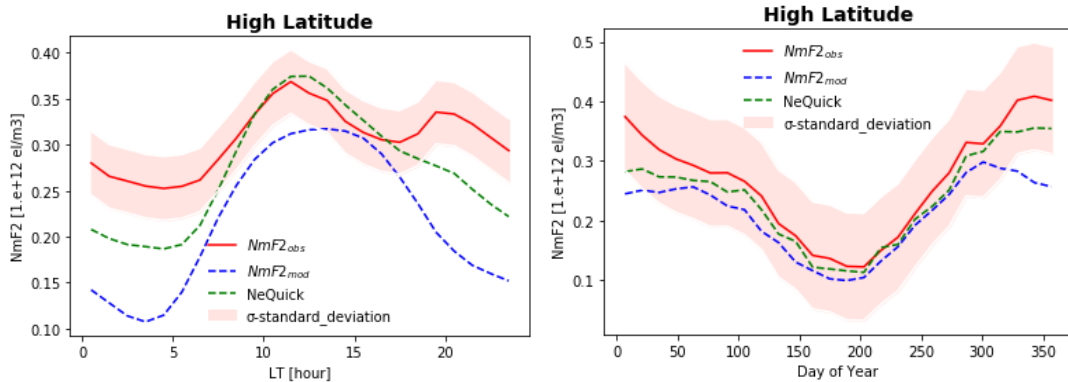


Fig.5.22. Diurnal and seasonal variations at high latitude at low solar activity (SPIDR)

- Medium solar activity ($F_{10.7} = 100-150$ flux units)

SPIDR

At high latitude for diurnal variations at medium solar activity both models have differences to the ionosonde data (provided by SPIDR). Regarding to the seasonal variations NeQuick model approximates to the ionosonde data a little bit better than NPDM model.

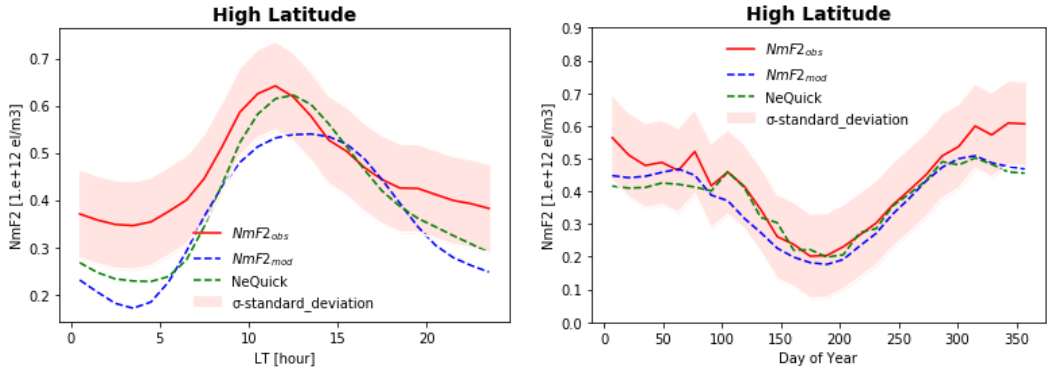


Fig.5.23. Diurnal and seasonal variations at high latitude at medium solar activity (SPIDR)

- High solar activity ($F_{10.7} = 150\text{-}200$ flux units)
- SPIDR

At high latitude for diurnal variations at high solar activity both models have differences to the ionosonde data (provided by SPIDR). Regarding to the seasonal variations NeQuick model approximates to the ionosonde data a little bit better than NPDM model.

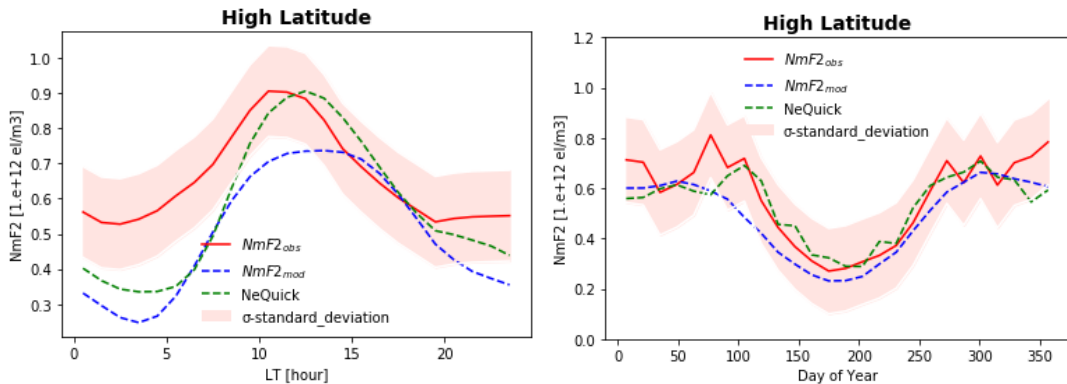


Fig.5.24. Diurnal and seasonal variations at high latitude at high solar activity (SPIDR)

5.2. Analysis of the peak height hmF2

Table.5.10. The validation strategy

Region	Low solar activity ($F_{10.7}$ 60-100 flux units)	Medium solar activity ($F_{10.7}$ 100-150 flux units)	High solar activity ($F_{10.7}$ 150-200 flux units)
60-90° N		3	
30-60° N		14	
0-30° N		1	
0-30° S		8	

30-60° S	No data
60-90° S	No data

Table 5.11. Geographic coordinates of ionosonde stations from SPIDR at high latitude

Region 60-90° North		
Station name/Id	Latitude /deg	Longitude /deg
NQJ61(NARSSARSSUAQ)	61.2	-45.4
TR170(TROMSO)	69.6	19.2
TR169(TROMSO)	69.7	19.0

Table 5.12. Geographic coordinates of ionosonde stations from SPIDR at medium latitude

Region 30 – 60° North		
Station name/Id	Latitude /deg	Longitude /deg
BJJ32(BERMUDA)	32.2	-64.4
EA036(EL ARENOSILLO)	37.1	-6.7
SN437	37.1	127.0
AN438(ANYANG)	37.4	127.0
AT138(ATHENS)	38.0	23.5
BC840(BOULDER)	40.0	-105.3
EB040(ROQUETES)	40.8	0.3
RO041(ROME)	41.8	12.5
BL841	41.9	-111.5
MHJ45(MILLSTONE_HILL)	42.6	-71.5
AFJ49(ARGENTIA)	47.3	-54.0
PQ052(PRUHONICE)	50.0	14.6
DB049(DOURBES)	50.1	4.6
JR055(JULIUSRUH/RUGEN)	54.6	13.4

Table 5.13. Geographic coordinates of ionosonde stations from SPIDR at low latitude

Region 0-30° North		
Station name/Id	Latitude /deg	Longitude /deg
KJ609(KWAJALEIN)	9.0	167.2

Table 5.14. Geographic coordinates of ionosonde stations from SPIDR at low latitude

Region 0 – 30° South		
Station name/Id	Latitude /deg	Longitude /deg
FZA0M(FORTALEZA)	-3.8	-38.0
AS00Q(ASCENSION)	-7.9	-14.4

JI91J(JICAMARCA)	-12.1	-77.0
DW41K(DARWIN)	-12.5	131.0
LM42B(LEARMONTH)	-21.9	114.0
MU12K(MADIMBU)	-22.4	30.9
TUJ2O(TUCUMAN)	-26.9	-65.4
LV12P(LOUISVALE)	-28.5	21.2

Figures (5.25-5.34) shows hmF2 comparisons among the Ionosonde data, NPHM results and NeQuick estimates as a function of Universal Time (UT) and Day of Year at high, mid and low geographic latitudes at different solar activity.

All plots are generated using NPHM and NeQuick models at different latitudes at different solar activity. Also we have used filter for $hmF2_{obs}$, $200 \leq hmF2_{obs} \leq 600$ [km]. For analysis were used mean values. Bin size for day is 14. Local time is presented in range from 0 to 24. On the plots red color represent the ionosonde data ($hmF2_{obs}$), blue – the NPHM model ($hmF2_{mod}$), green – the NeQuick model and standard deviation (σ).

We see that at medium and high latitudes NPHM model performs better than the NeQuick model for diurnal variation. At low latitudes, the NPHM model approximates the ionosonde data better during medium solar activity, compared to the low solar activity conditions.

For seasonal variations NPHM model performs better than NeQuick model at mid latitudes. The best results NPHM model shows at medium latitude at low and medium solar activity.

1. Model comparison at high latitude (60-90°N)
 - Low solar activity ($F10.7 = 60-100$ flux units)

SPIDR

At high latitude for diurnal variations at low solar activity, the NPHM and NeQuick models have differences to the ionosonde data (provided by SPIDR) between 08:00 and 17:00 LT. Regarding to the seasonal variations, NeQuick model approximates to the ionosonde data (provided by SPIDR) a little bit better than NPDM model.

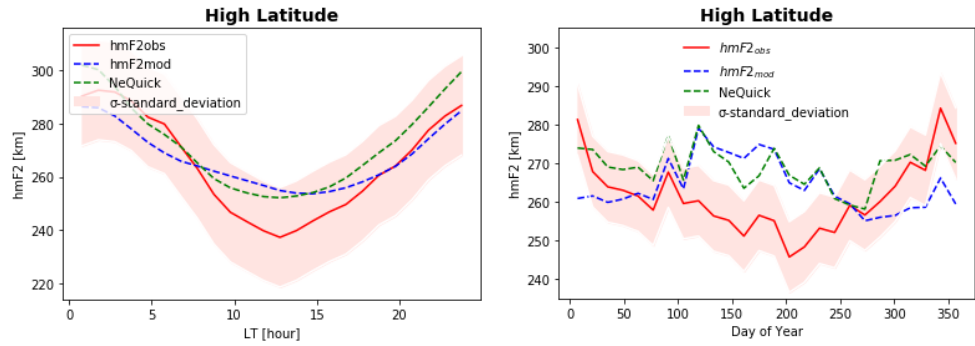


Fig.5.25. Diurnal and seasonal variations at high latitude at low solar activity

- Medium solar activity ($F_{10.7} = 100\text{-}150$ flux units)

SPIDR

At high latitude for diurnal variations at medium solar activity, the NPHM model approximates to the ionosonde data (provided by SPIDR) better than NeQuick model. Regarding to the seasonal variations, NeQuick and NPHM models have differences to the ionosonde data.

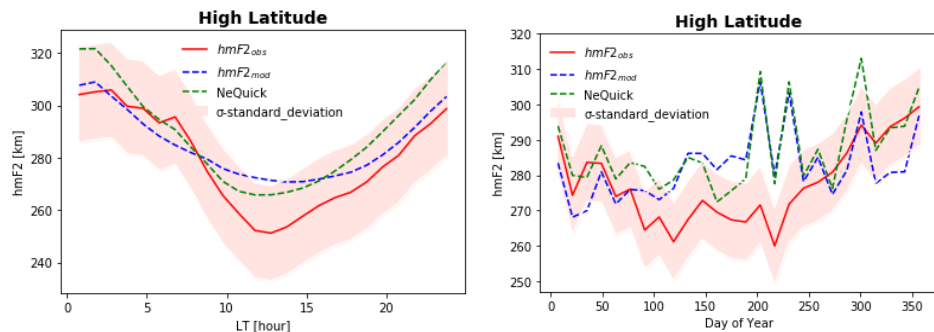


Fig.5.26. Diurnal and seasonal variations at high latitude at medium solar activity

- High solar activity ($F_{10.7} = 150\text{-}200$ flux units)

SPIDR

At high latitude for diurnal variations at high solar activity, the NPHM model approximates to the ionosonde data (provided by SPIDR) better than NeQuick model. Regarding to the seasonal variations, NPHM model approximates to the ionosonde data better than NeQuick model, but during summer period there are differences also.

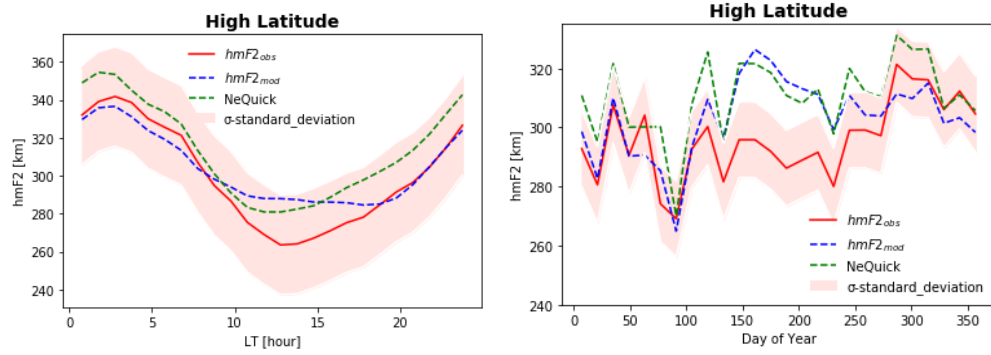


Fig.5.27. Diurnal and seasonal variations at high latitude at high solar activity

2. Model comparison at medium latitude (30-60°N)

- Low solar activity ($F_{10.7} = 60\text{-}100$ flux units)

SPIDR

At medium latitude for diurnal and seasonal variations at low solar activity, the NPHM model approximates to the ionosonde data (provided by SPIDR) better than NeQuick model.

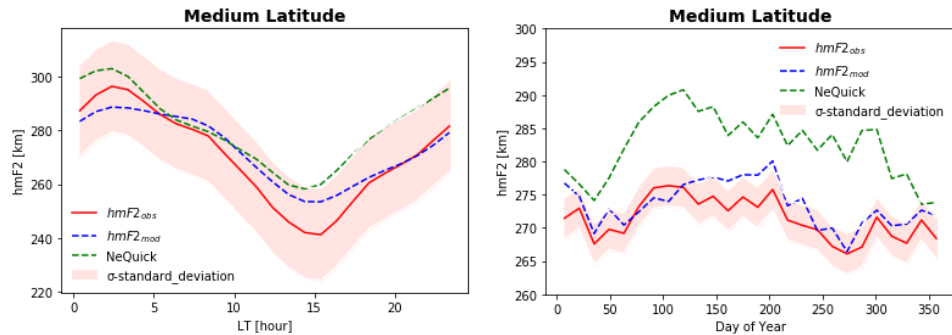


Fig.5.28. Diurnal and seasonal variations at medium latitude at low solar activity

- Medium solar activity ($F_{10.7} = 100\text{-}150$ flux units)

SPIDR

At medium latitude for diurnal and seasonal variations at medium solar activity, the NPHM model approximates to the ionosonde data (provided by SPIDR) better than NeQuick model.

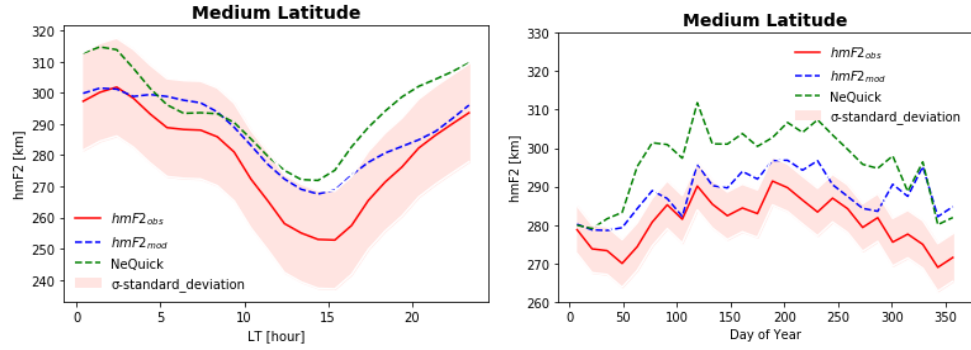


Fig.5.29. Diurnal and seasonal variations at medium latitude at medium solar activity

- High solar activity ($F_{10.7} = 150\text{-}200$ flux units)

SPIDR

At medium latitude for diurnal and seasonal variations at high solar activity, the NPHM model approximates to the ionosonde data (provided by SPIDR) better than NeQuick model.

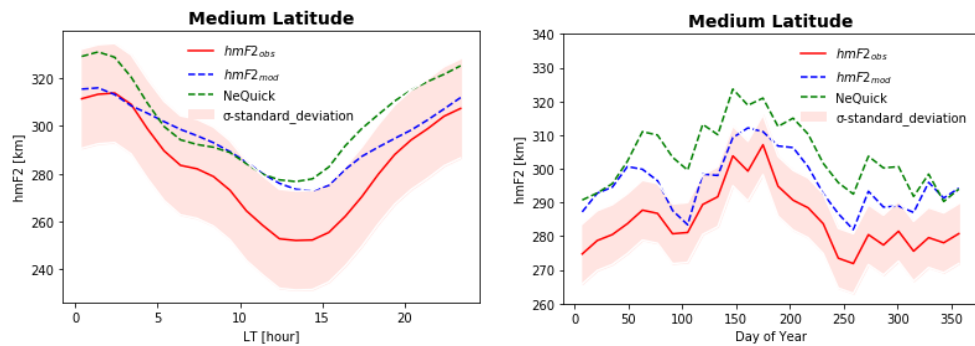


Fig.5.30. Diurnal and seasonal variations at medium latitude at high solar activity

3. Model comparison at low latitude ($0\text{-}30^\circ\text{N}$)

- Low solar activity ($F_{10.7} = 60\text{-}100$ flux units)

SPIDR

At low latitude for diurnal and seasonal variations at low solar activity, the NeQuick model approximates to the ionosonde data (provided by SPIDR) a little bit better than NPHM model, but there are also differences.

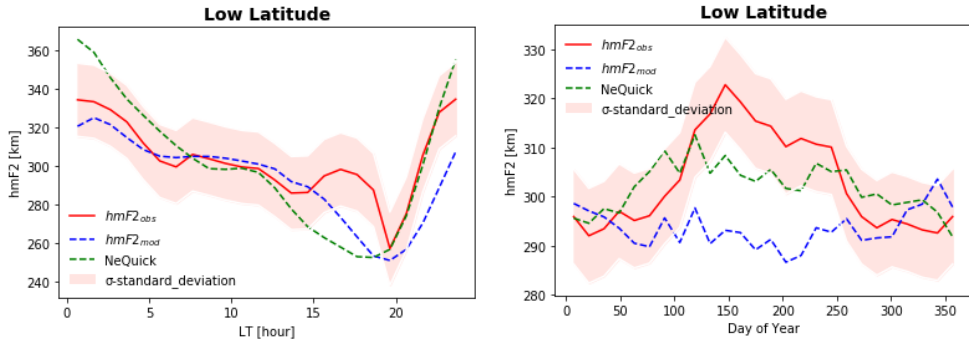


Fig.5.31. Diurnal and seasonal variations at low latitude at low solar activity

- Medium solar activity ($F_{10.7} = 100\text{-}150$ flux units)
 - No data
- High solar activity ($F_{10.7} = 150\text{-}200$ flux units)
 - No data
- 4. Model comparison at low latitude ($0\text{-}30^\circ\text{S}$)
 - Low solar activity ($F_{10.7} = 60\text{-}100$ flux units)

SPIDR

At low latitude for diurnal variations at low solar activity, the NPHM model approximates to the ionosonde data (provided by SPIDR) better than NeQuick model. Regarding to the seasonal variations, NPHM model approximates to the ionosonde data better than NeQuick model, but during summer period there are differences also.

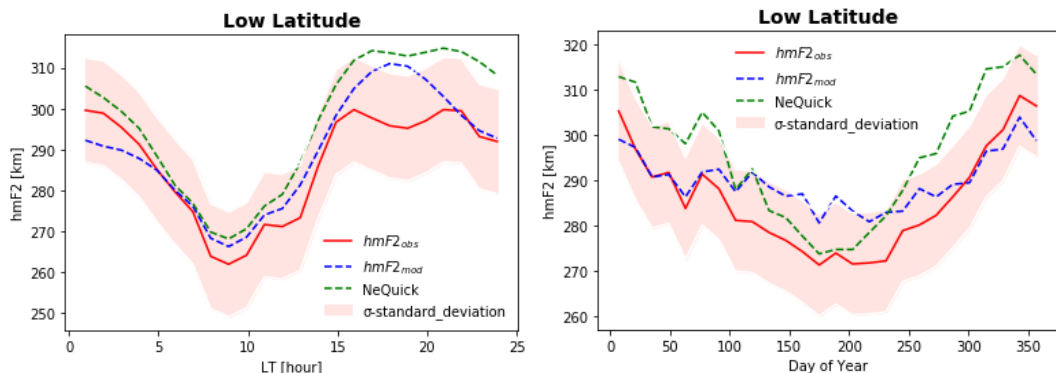


Fig.5.32. Diurnal and seasonal variations at low latitude at low solar activity

- Medium solar activity ($F_{10.7} = 100\text{-}150$ flux units)

SPIDR

At low latitude for diurnal variations at medium solar activity, the NPHM model approximates to the ionosonde data (provided by SPIDR) better than NeQuick model. Regarding to the seasonal variations, NeQuick model approximates to the ionosonde data better than NPHM model.

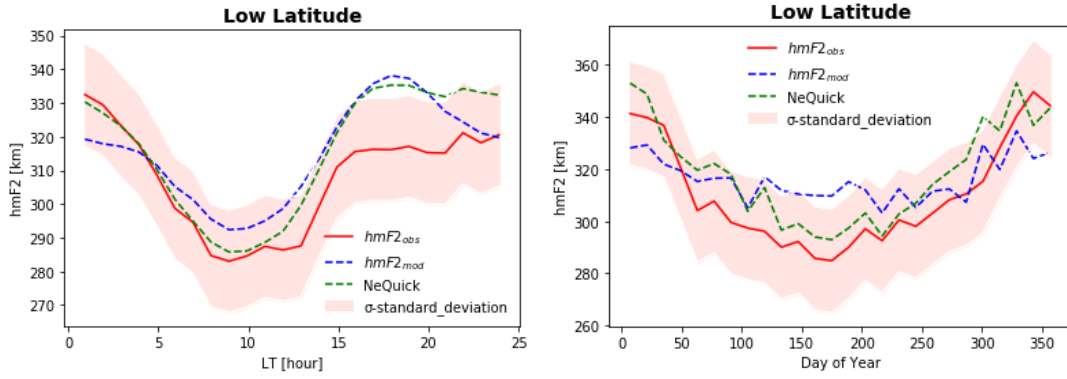


Fig.5.33. Diurnal and seasonal variations at low latitude at medium solar activity

- High solar activity ($F_{10.7} = 150\text{-}200$ flux units)

SPIDR

At low latitude for diurnal variations at high solar activity, the NPHM model approximates to the ionosonde data (provided by SPIDR) better than NeQuick model. Regarding to the seasonal variations, both model have differences to the ionosonde data.

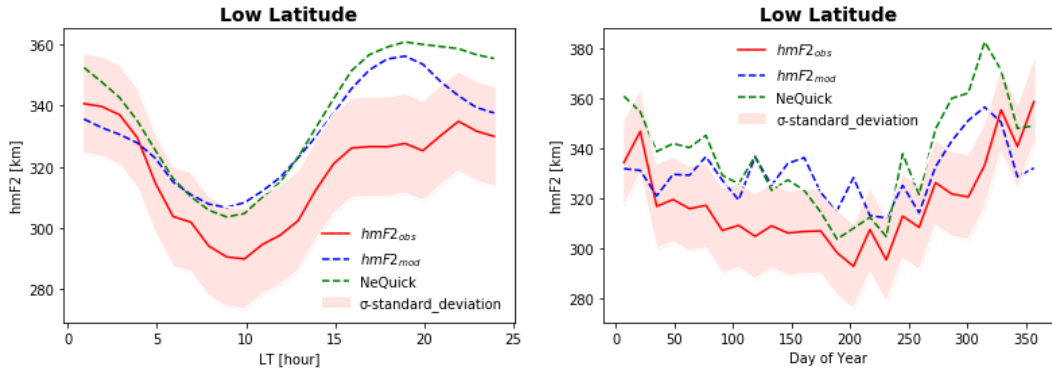


Fig.5.34. Diurnal and seasonal variations at low latitude at high solar activity

5. Model comparison at medium latitude ($30\text{-}60^\circ\text{S}$)

No data

6. Model comparison at high latitude ($60\text{-}90^\circ\text{S}$)

No data

5.3. Time series analysis of the Ionosonde data (2009-2018 years)

Figures (5.35-5.37) show NmF2 comparisons among the Ionosonde data, NPDM, NPHM results and NeQuick estimates as a function of Universal Time (UT) and Day of Year for different LT period.

Table 5.15. Number of obs. used

Year	Stations		
	JR055 (JULIUSRUH/RUGEN)	RL052 (CHILTON)	RO041 (ROME)
2009	30362	47481	24687
2010	32886	47850	26257
2011	26819	43986	23185
2012	-	47924	-
2013	1174	47175	30172
2014	32179	46196	26700
2015	33563	48521	27823
2016	74281	46114	26219
2017	71883	46991	26422
2018	31795	12739	10135

5.3.1. JR055 (JULIUSRUH/RUGEN)

All plots are generated using NPDM and NeQuick models for different years at different LT periods: 06:00-08:00 LT, 12:00-14:00 LT, 18:00-20:00 LT, 22:00-24:00 LT. Also we have used filter for $NmF2_{obs}$, $0.01 \leq NmF2_{obs} \leq 15$ [1.e+12 el/m³]. For analysis were used mean values. Bin size for day is 14. On the plots red color represent the ionosonde data ($NmF2_{obs}$), blue – the NPDM model ($NmF2_{mod}$), green – the NeQuick model. The last panel represents the F10.7.

The maximum of solar radio flux parameter for the station JR055 (JULIUSRUH/Rügen) during period 2009-2018 years were:

2009 year: 320-321days, F10.7 = 80 fu.

2011 year: 67day, F10.7 = 164 fu; 267day, F10.7 = 191fu.

2017 year: 310day, F10.7 = 180fu.

2018 year: 44day, F10.7 = 76 fu; 120-121days, F10.7 = 76fu.

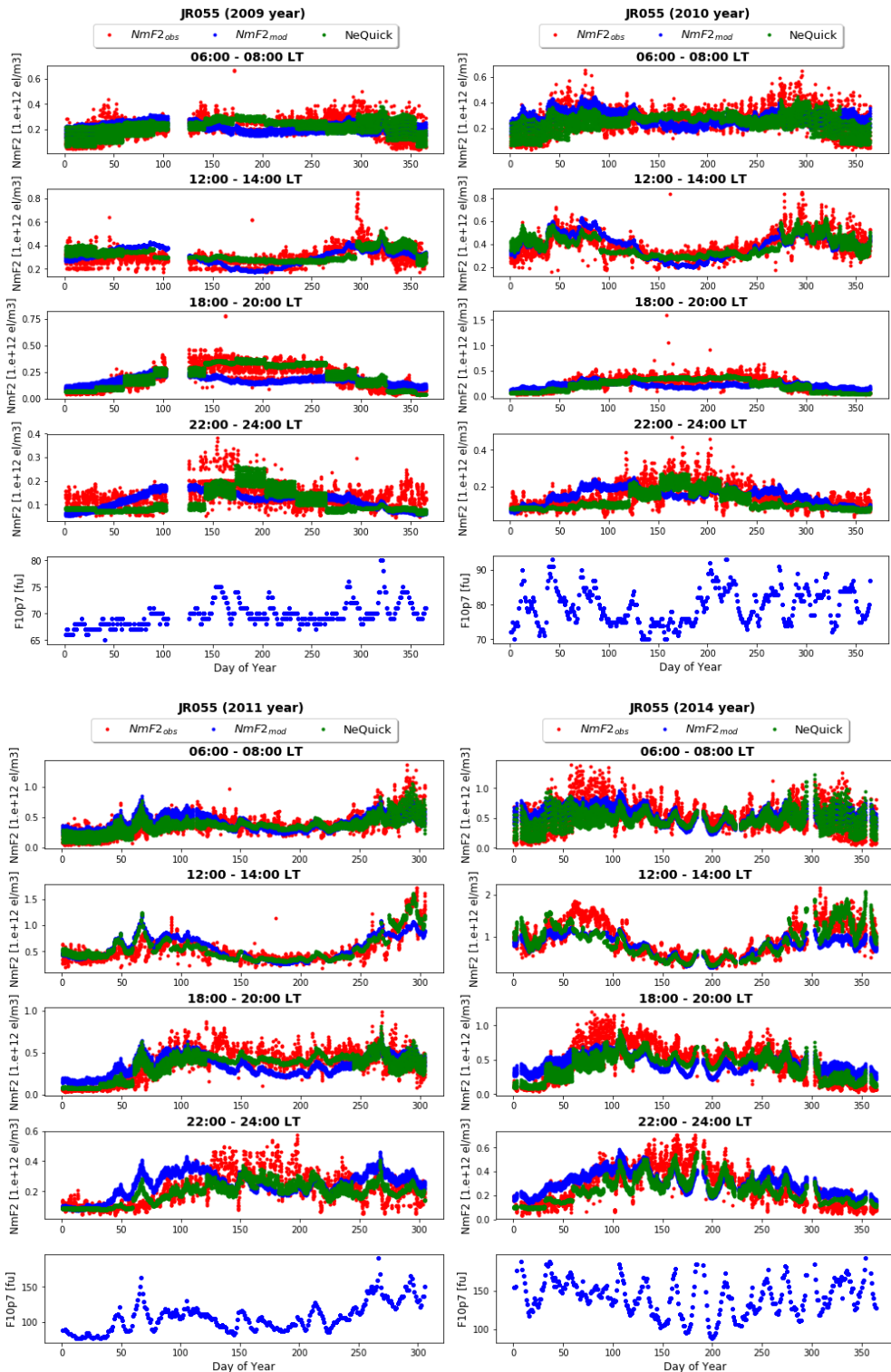


Fig.5.35. Seasonal variation NmF2 and F10p7 for station JR055 (2009-2011, 2014)

The NeQuick model follows the observation better than NPDM model during 22:00-24:00 LT period.

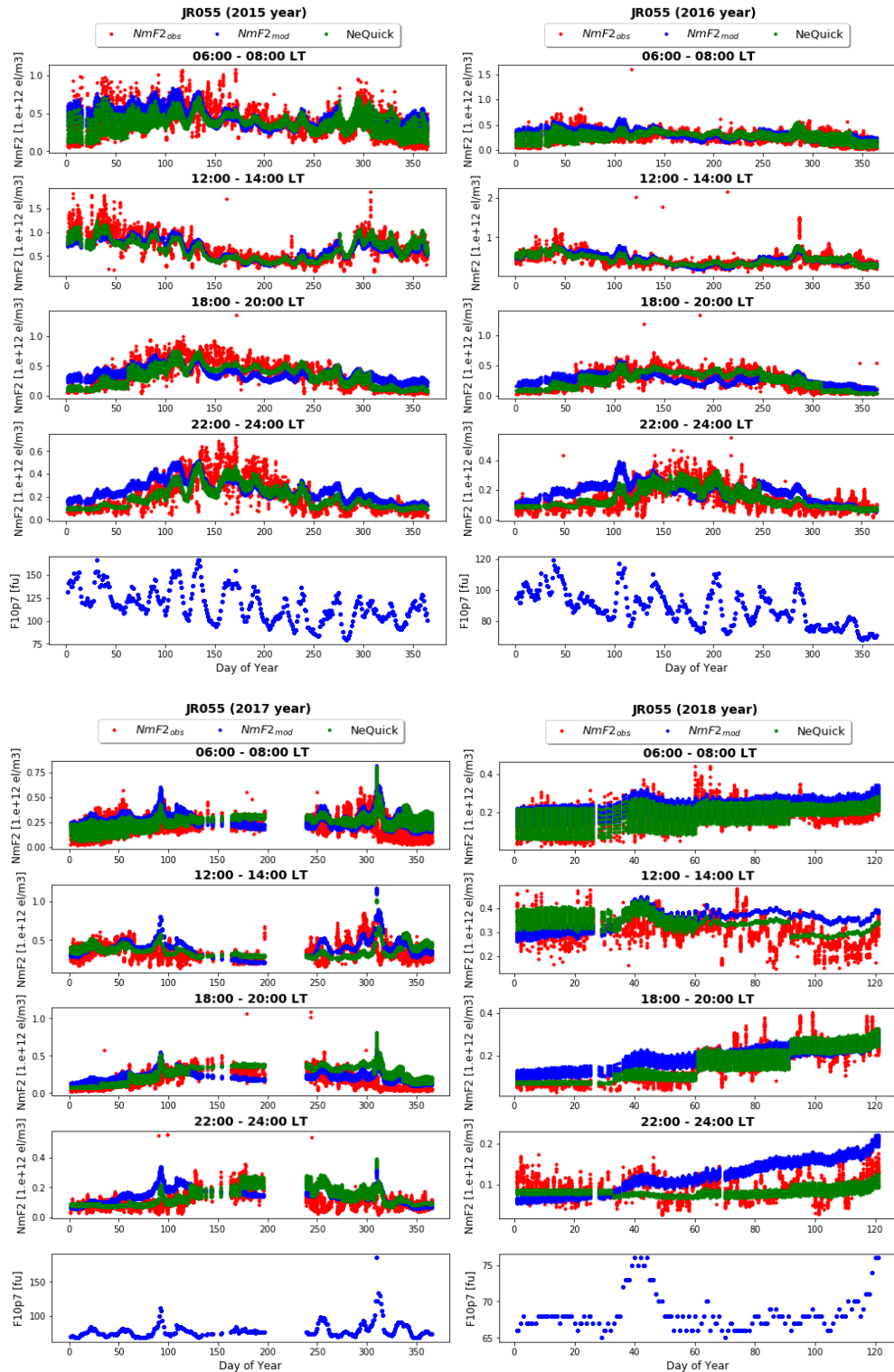


Fig.5.36. Seasonal variation NmF2 and F10p7 for station JR055 (2015-2018)

The NeQuick model follows the observation better than NPDM model during 22:00-24:00 LT period.

5.3.2. RL052 (CHILTON)

All plots are generated using NPDM and NeQuick models for different years at different LT periods: 1) 06:00-08:00 LT, 12:00-14:00 LT, 18:00-20:00 LT, 22:00-24:00 LT.

Also we have used filter for $NmF2_{obs}$, $0.01 \leq NmF2_{obs} \leq 15$ [$1.e+12$ el/m³]. For analysis were used mean values. Bin size for day is 14. On the plots red color represent the ionosonde data ($NmF2_{obs}$), blue – the NPDM model ($NmF2_{mod}$), green – the NeQuick model. The last panel represents the F10.7.

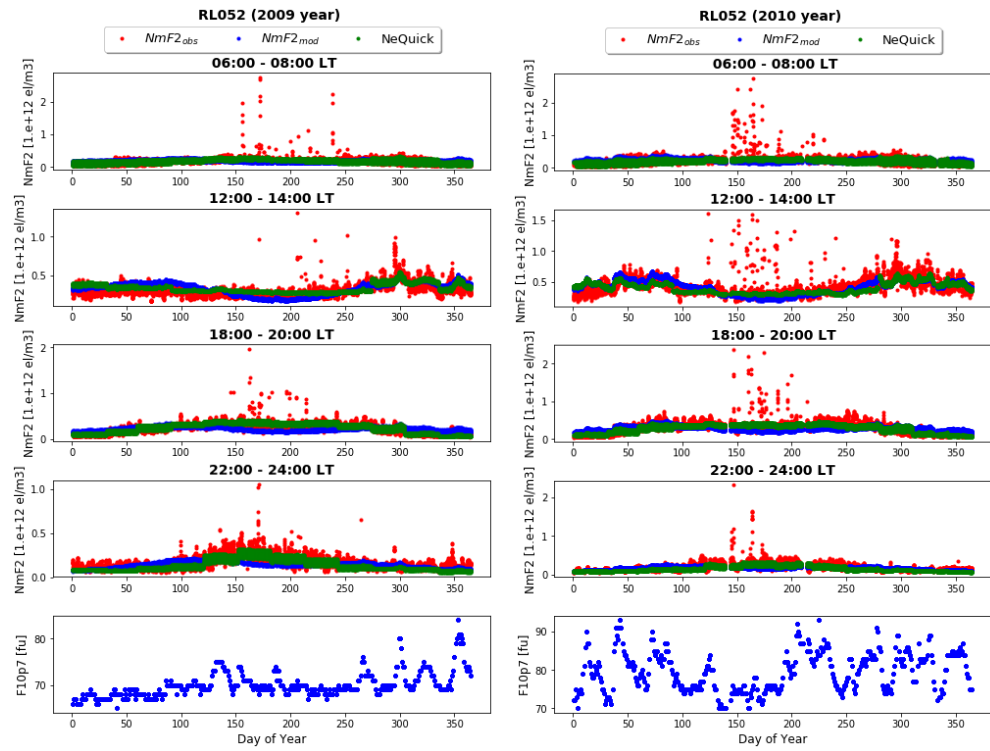
The maximum of solar radio flux parameter for the station RL052 (CHILTON) during period 2009-2018 years were:

2009 year: 300day, F10.7 = 80fu; 353day, F10.7 = 84fu.

2011 year: 71day, F10.7 = 164 fu; 287day, F10.7 = 191 fu.

2017 year: 253day, F10.7 = 185 fu.

2018 year: 44day, F10.7 = 76 fu.



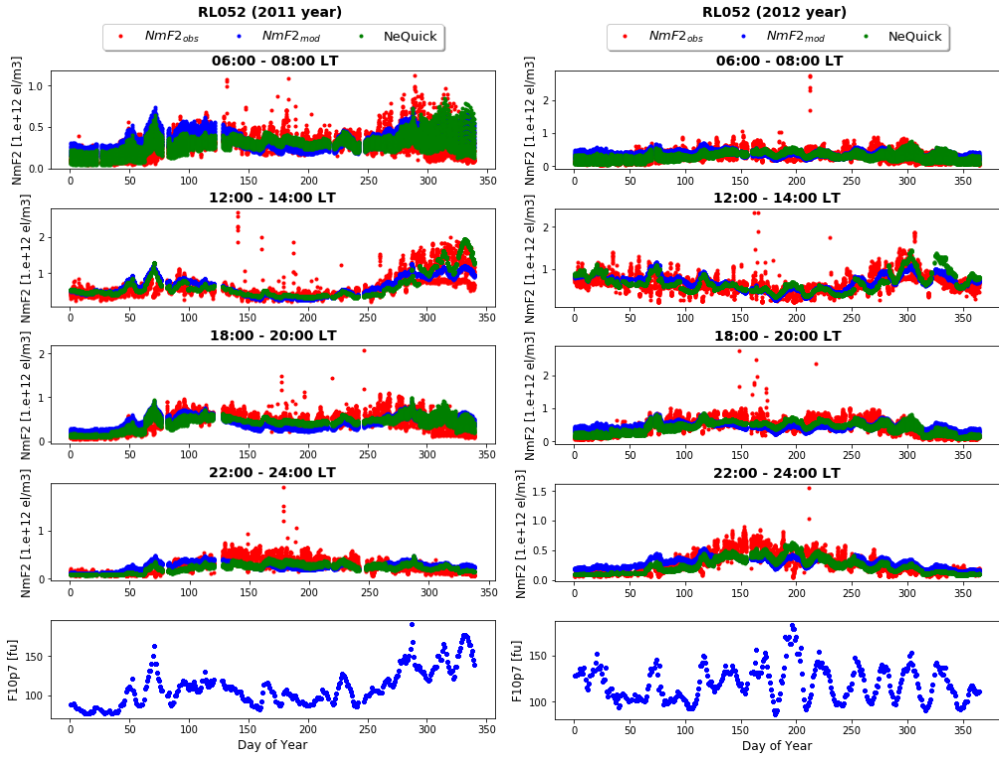
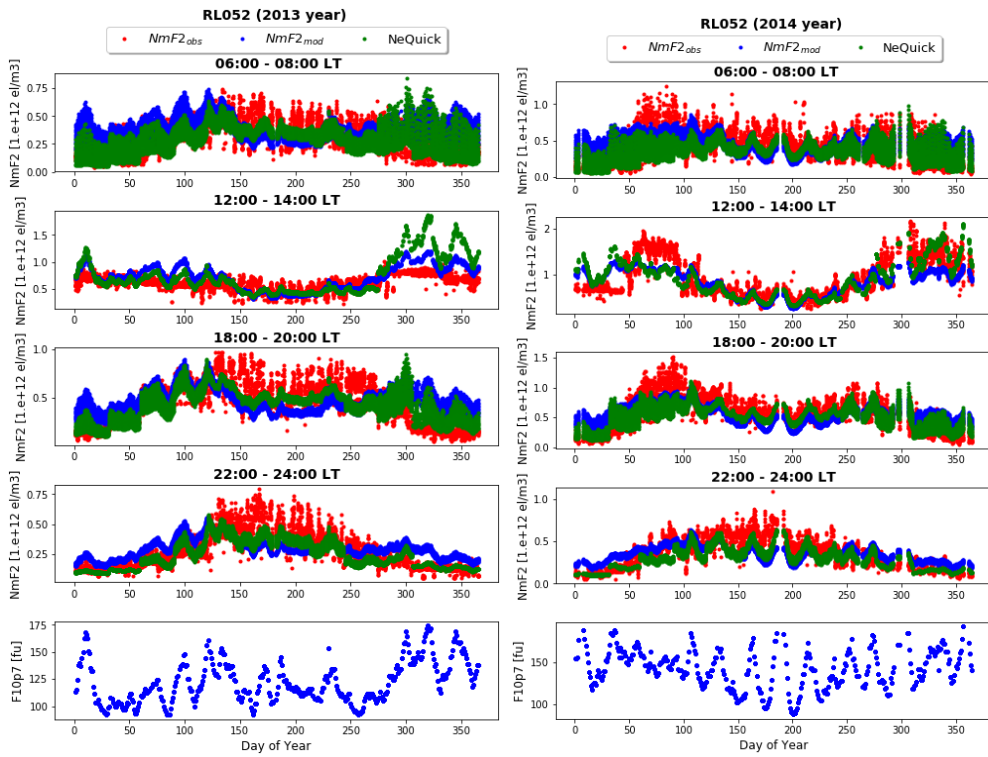


Fig.5.37. Seasonal variation NmF2 and F10p7 for station JR055 (2009-2012)

The NeQuick model follows the observation better than NPDM model during 22:00-24:00 LT period.



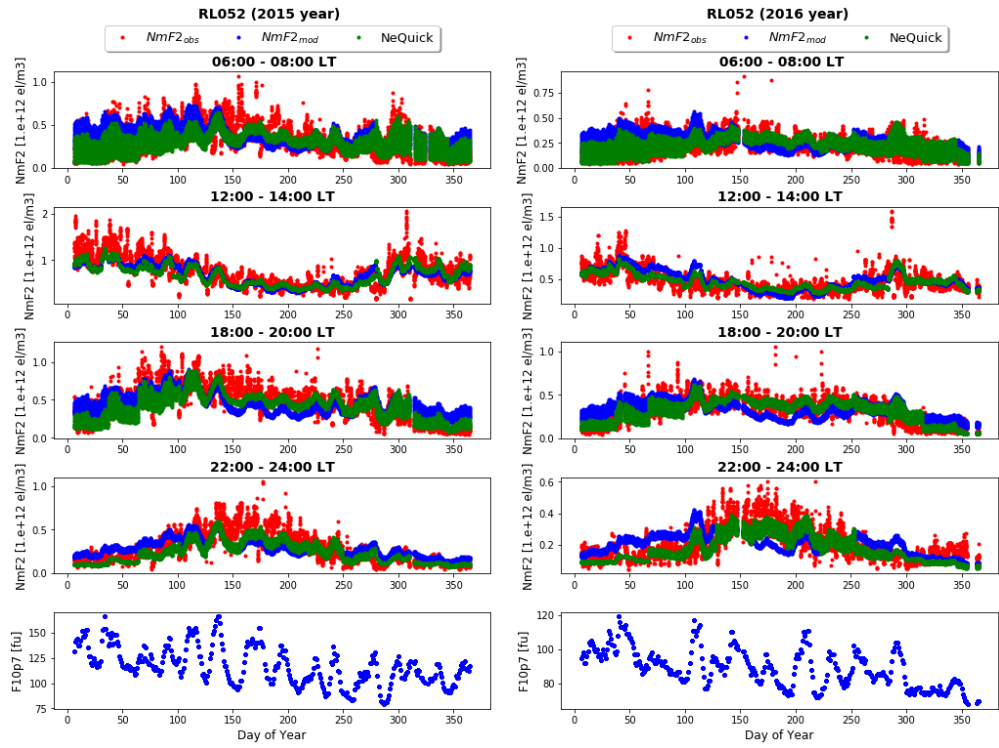


Fig.5.38. Seasonal variation NmF2 and F10p7 for station JR055 (2013-2016)

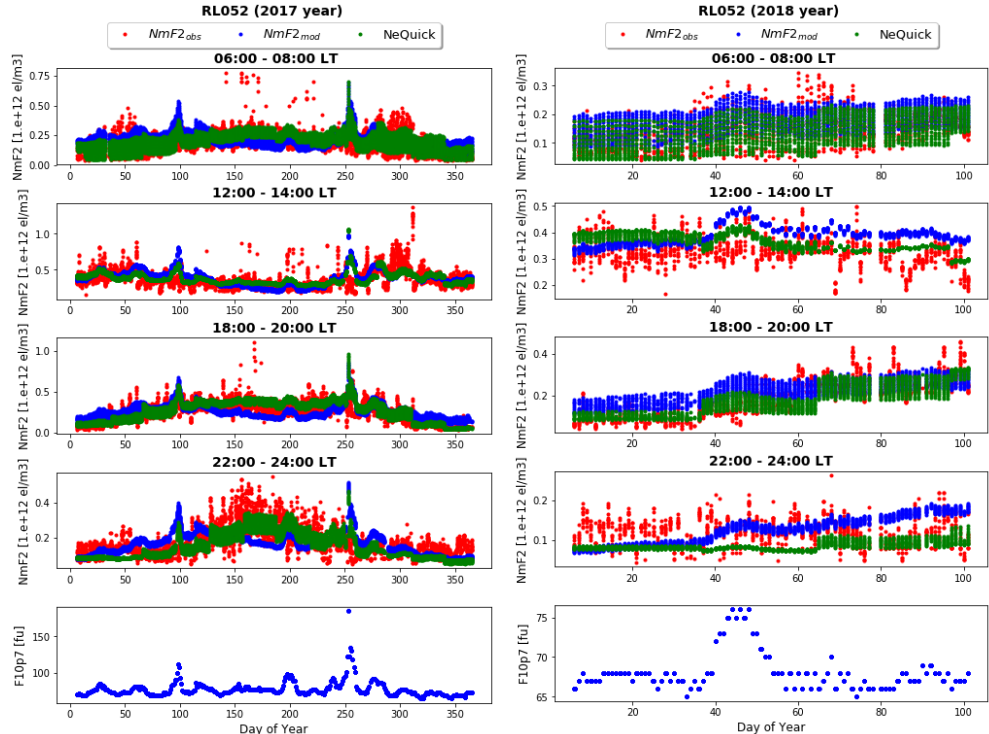


Fig.5.39. Seasonal variation NmF2 and F10p7 for station RL052 (2017-2018)

The NeQuick model follows the observation better than NPDM model during 22:00-24:00 LT period.

5.3.3. RO041 (ROME)

The maximum of solar radio flux parameter for the station RO041 (ROME) during period 2009-2018 years were:

2009 year: 301day, $F_{10p7} = 80.30$ f.u; 353day, $F_{10p7} = 84.20$ f.u.

2011: 70day, $F_{10.7} = 164.30$ f.u; 272day, $F_{10.7} = 191.60$ f.u.

2017: 92day, $F_{10.7} = 111.90$ f.u; 249day, $F_{10.7} = 134.90$ f.u.

2018: 41day, $F_{10.7} = 76.90$ f.u; 122day $F_{10.7} = 76.90$ f.u.

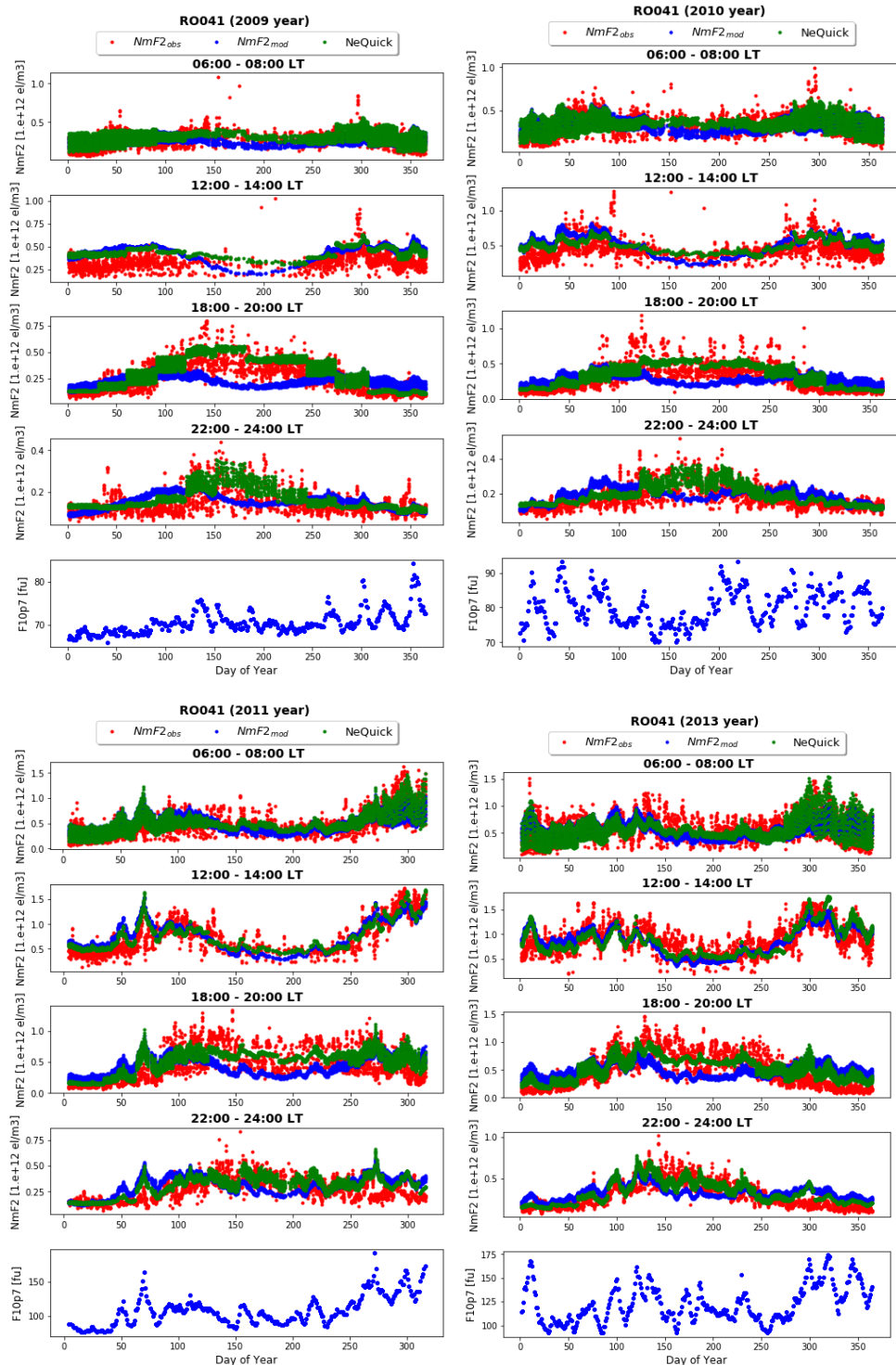


Fig.5.40. Seasonal variation $NmF2$ and F_{10p7} for station RL052 (2009-2011, 2013)

The NeQuick model follows the observation better than NPDM model during 22:00-24:00 LT period.

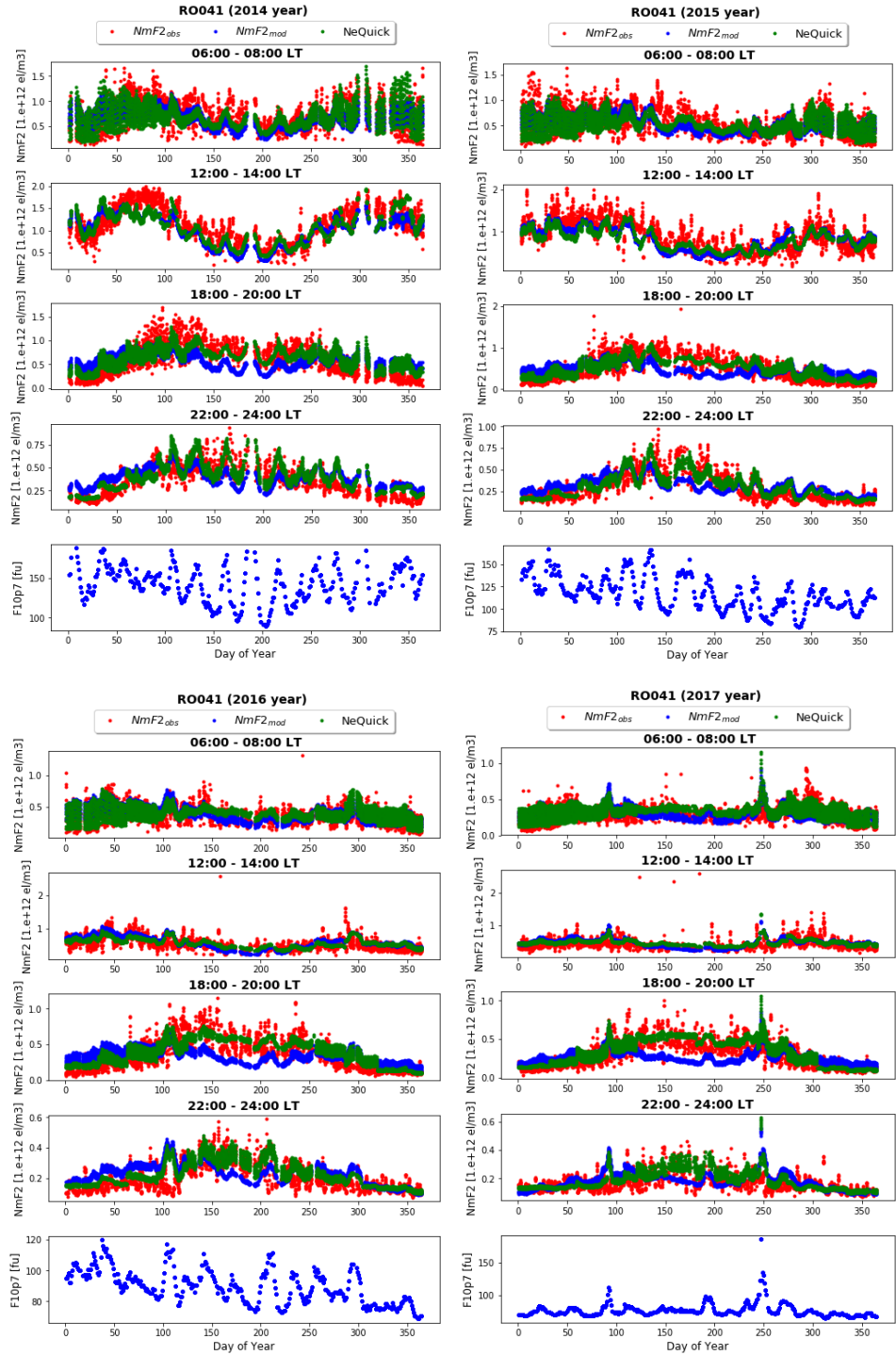


Fig.5.41. Seasonal variation NmF2 and F10p7 for station RL052 (2014-2017)

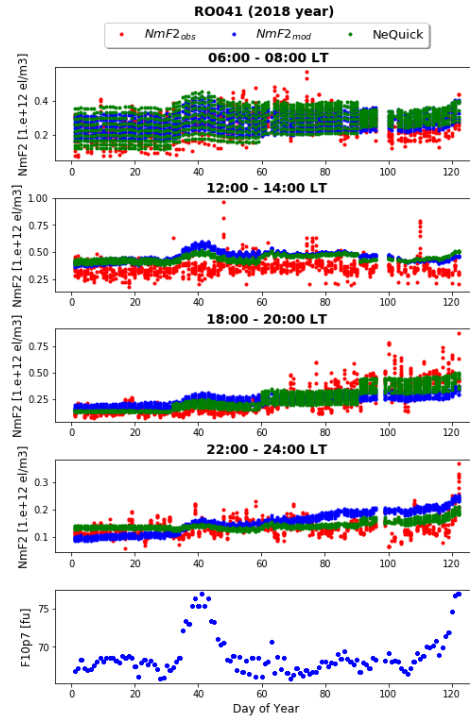


Fig.5.42. Seasonal variation $NmF2$ and $F10p7$ for station RO041 (2018)

The NeQuick model follows the observation better than NPDM model during 22:00-24:00 LT period, but there is a gap in data during 97-99 days.

5.4. The statistic for $NmF2_{mod}$ - $NmF2_{obs}$ and $hmF2_{mod}$ - $hmF2_{obs}$

To compare again both models performance, we have computed the differences between ionosonde observation and model results for all hourly values (of $NmF2$ and $hmF2$) and estimated the RMS of differences at each verification station for the selected periods.

The NTCM and NeQuick $NmF2_{mod}$ - $NmF2_{obs}$ and $hmF2_{mod}$ - $hmF2_{obs}$ estimates are calculated for comparison at the same location and time window. The histograms of differences are shown in Fig. (5.38-5.55). The corresponding RMS, mean deviation and standard deviation of $NmF2_{mod}$ - $NmF2_{obs}$ and $hmF2_{mod}$ - $hmF2_{obs}$ differences are also given in Fig.(5.38-5.55).

The plots are generated using NPDM, NPHM and NeQuick models at different latitudes at different solar activity. In histogram plots are drawn model residual, one panel represent statistic for $NmF2$, second one – for $hmF2$. The red color represents $NeQuick-NmF2_{obs}$ ($NeQuick-hmF2_{obs}$) and green $NPDM-NmF2_{obs}$ ($NPHM-hmF2_{obs}$). Bins for residuals are 400.

Table.5.16. RMS values for ionosonde data at different latitudes at different solar activity

	rms [$1e+11 el/m^3$] NmF2		rms [km] hmF2	
	NeQ	NPDM	NeQ	NPHM
60-90°N				
Low solar activity (F10.7 = 60-100 flux units)	0.9	0.7	45.92	41.97
Medium solar activity (F10.7 = 100-150 flux units)	1.5	1.1	45.23	42.97
High solar activity (F10.7 = 150-200 flux units)	No data		42.49	42.39
30-60°N				
Low solar activity (F10.7 = 60-100 flux units)	2.4	1.9	36.31	36.01
Medium solar activity (F10.7 = 100-150 flux units)	3.6	3.2	37.57	41.1
High solar activity (F10.7 = 150-200 flux units)	2.2	2.0	45.13	49.79
0-30°N				
Low solar activity (F10.7 = 60-100 flux units)	3.1	2.2	No data	
Medium solar activity (F10.7 = 100-150 flux units)	4.6	3.2	No data	
High solar activity (F10.7 = 150-200 flux units)	5.7	3.5	No data	
0-30°S				
Low solar activity (F10.7 = 60-100 flux units)	3.6	3.1	45.64	42.27
Medium solar activity (F10.7 = 100-150 flux units)	6.0	5.0	53.39	47.45
High solar activity (F10.7 = 150-200 flux units)	6.6	4.6	No data	
30-60°S				
Low solar activity (F10.7 = 60-100 flux units)	1.3	1.2	No data	
Medium solar activity (F10.7 = 100-150 flux units)	2.2	2.0	No data	
High solar activity (F10.7 = 150-200 flux units)	2.8	2.4	No data	
60-90°S				
Low solar activity (F10.7 = 60-100 flux units)	2.1	1.5	No data	
Medium solar activity (F10.7 = 100-150 flux units)	3.0	2.5	No data	
High solar activity (F10.7 = 150-200 flux units)	4.2	3.6	No data	

1) Model statistics at low latitude (60-90°N)

- Low solar activity ($F_{10.7} = 60\text{-}100$ flux units)

At high latitude at low solar activity the statistic parameters root mean square (rms), standard deviation (std) have almost the same values for the NeQuick and NPDM models. Comparing NPHM and NeQuick models, we see that for the NPHM model standard deviation and mean values are less.

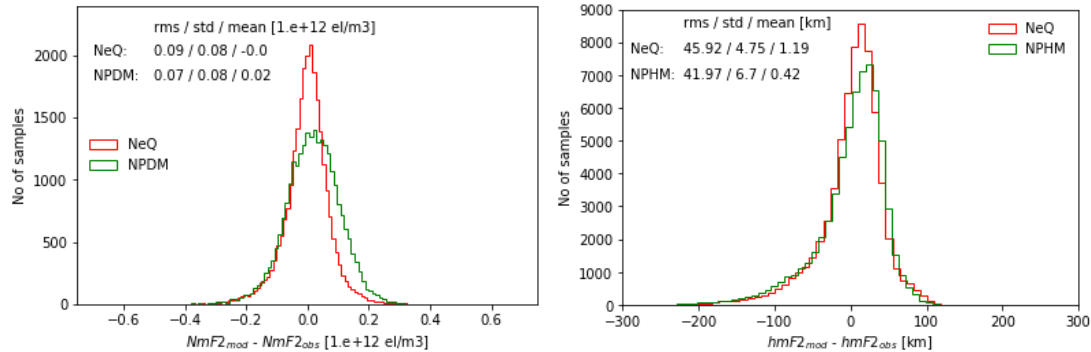


Fig. 5.43. Histogram $NmF2_{mod}-NmF2_{obs}$ and $hmF2_{mod}-hmF2_{obs}$ at high latitude at low solar activity

- Medium solar activity ($F_{10.7} = 100\text{-}150$ flux units)

At high latitude at medium solar activity the residual statistic such as root mean square (rms), standard deviation (std) are less better for the NeQuick, than for NPDM models. Comparing NPHM and NeQuick models, we see that for NPHM statistic parameters have better (less) values.

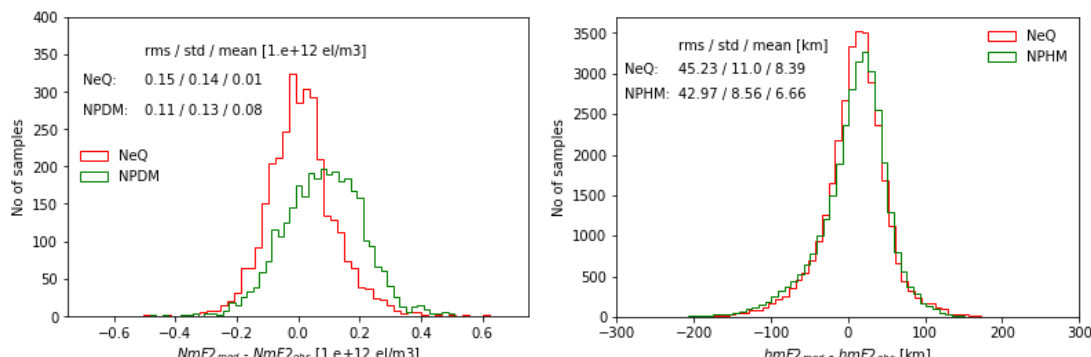


Fig. 5.44. Histogram $NmF2_{mod}-NmF2_{obs}$ and $hmF2_{mod}-hmF2_{obs}$ at high latitude at medium solar activity

- High solar activity ($F_{10.7} = 150\text{-}200$ flux units)

At high latitude at high solar activity the statistic parameters root mean square (rms), standard deviation (std) and mean value (mean) NPHM model has better statistic than NeQuick model.

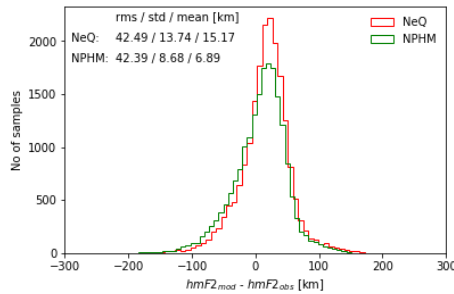


Fig.5.45. Histogram $hmF2_{mod} - hmF2_{obs}$ at high latitude at high solar activity

2) Model statistics at medium latitude (30-60°N)

- Low solar activity ($F10.7 = 60-100$ flux units)

At medium latitude at low solar activity the statistic parameter standard deviation (std) have the same values for the NeQuick and NPDM models, but root mean square (rms) is less for NPDM model. Comparing the NPHM and NeQuick models, we see that for the NPHM root mean square and standard deviation values are better.

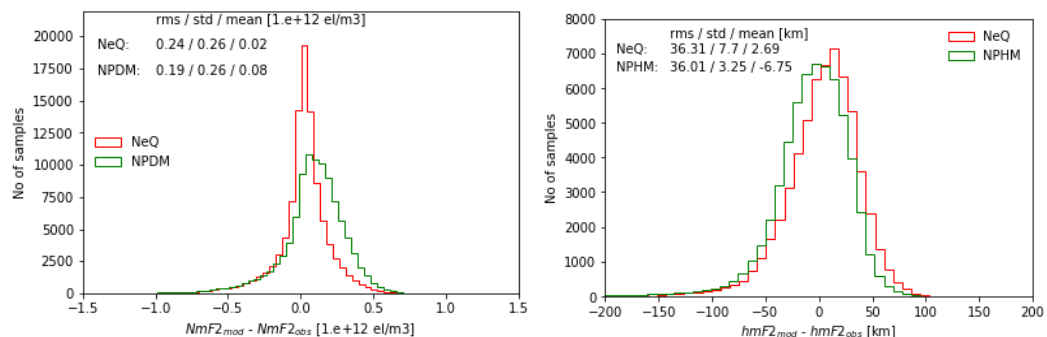


Fig.5.46. Histogram $NmF2_{mod} - NmF2_{obs}$ and $hmF2_{mod} - hmF2_{obs}$ at medium latitude at low solar activity

- Medium solar activity ($F10.7 = 100-150$ flux units)

At medium latitude at low solar activity the statistic parameters standard deviation (std) and mean have less value for NeQuick model. Comparing the NPHM and NeQuick models, we see that for the NeQuick models has better values of statistic parameters such as standard deviation and mean.

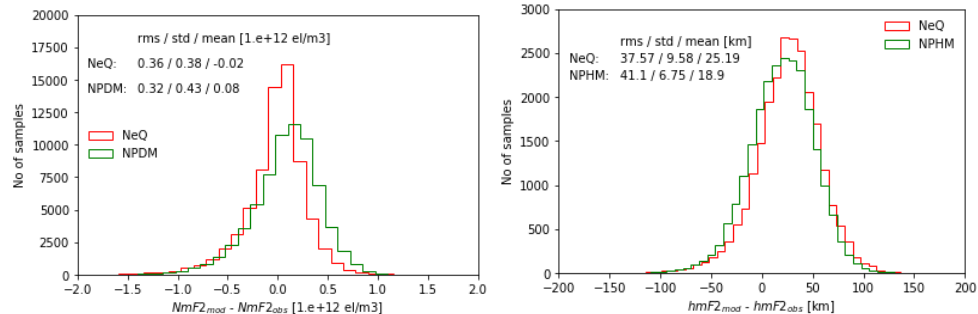


Fig.5.47. Histogram $NmF2_{mod}$ - $NmF2_{obs}$ and $hmF2_{mod}$ - $hmF2_{obs}$ at medium latitude at medium solar activity

- High solar activity ($F10.7 = 150\text{-}200$ flux units)

At medium latitude at high solar activity the statistic parameters showed better results for NeQuick model. Comparing the NPHM and NeQuick models, we see that for the NeQuick root mean square value is less than for the NPHM model.

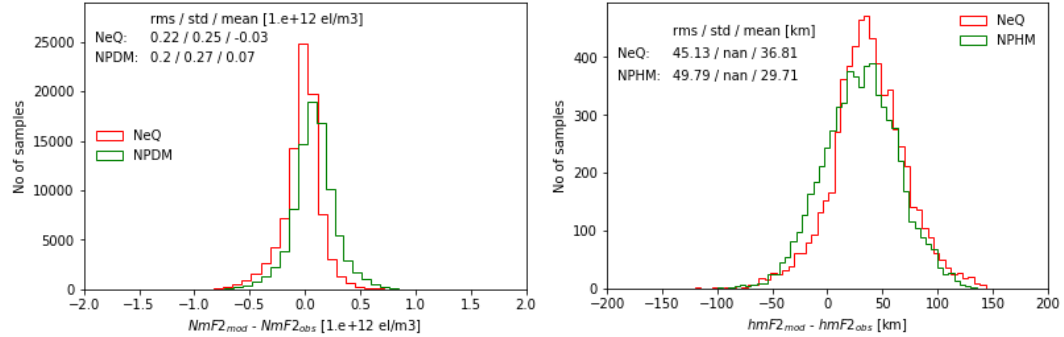


Fig.5.48. Histogram $NmF2_{mod}$ - $NmF2_{obs}$ and $hmF2_{mod}$ - $hmF2_{obs}$ at medium latitude at high solar activity

- 3) Model statistics at low latitude (0-30°N)
- Low solar activity ($F10.7 = 60\text{-}100$ flux units)

At low latitude at low solar activity the statistic parameters root mean square (rms) and standard deviation (std) are less for the NPDM model.

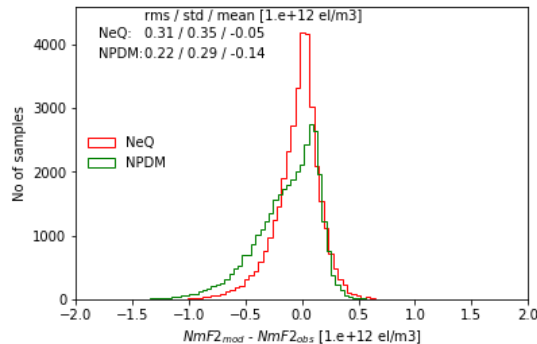


Fig.5.49. Histogram $NmF2_{mod}$ - $NmF2_{obs}$ at low latitude at low solar activity

- Medium solar activity ($F10.7 = 100\text{-}150$ flux units)

At low latitude at medium solar activity the statistic parameters standard deviation (std) and mean value (mean) have better values for the NeQuick model.

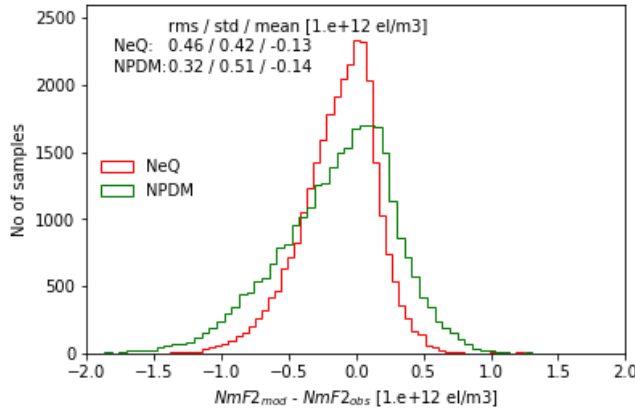


Fig.5.50. Histogram $NmF2_{mod} - NmF2_{obs}$ at low latitude at medium solar activity

➤ High solar activity ($F10.7 = 150\text{-}200$ flux units)

At low latitude at high solar activity the statistic parameters standard deviation (std) and mean value (mean) are less for NeQuick model.

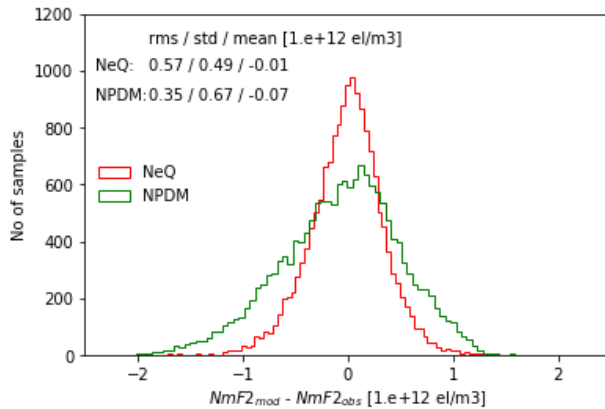


Fig.5.51. Histogram $NmF2_{mod} - NmF2_{obs}$ at low latitude at high solar activity

4) Model statistics at low latitude ($0\text{-}30^\circ S$)

➤ Low solar activity ($F10.7 = 60\text{-}100$ flux units)

At low latitude at low solar activity the statistic parameters root mean square (rms) and standard deviation (std) are better for the NPDM model. Comparing the NPHM and NeQuick models, we see that for the NPHM root mean square and mean values are less than for the NeQuick model.

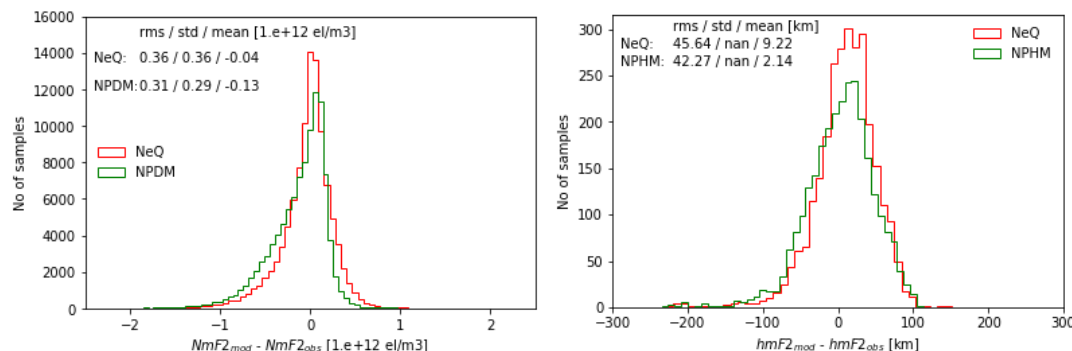


Fig.5.52. Histogram $NmF2_{mod}$ - $NmF2_{obs}$ and $hmF2_{mod}$ - $hmF2_{obs}$ at low latitude at low solar activity

- Medium solar activity ($F10.7 = 100\text{-}150$ flux units)

At low latitude at medium solar activity the statistic parameters standard deviation (std) and mean are better for the NeQuick. Comparing the NPHM and NeQuick models, we see that for the NPHM model mean value is less for the NeQuick model.

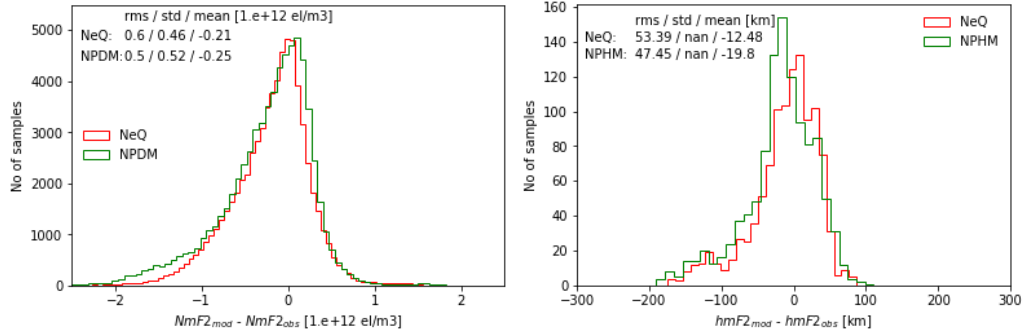


Fig.5.53. Histogram $NmF2_{mod}$ - $NmF2_{obs}$ and $hmF2_{mod}$ - $hmF2_{obs}$ at low latitude at medium solar activity

- High solar activity ($F10.7 = 150\text{-}200$ flux units)

At low latitude at high solar activity the statistic parameters standard deviation and mean are less for the NeQuick model.

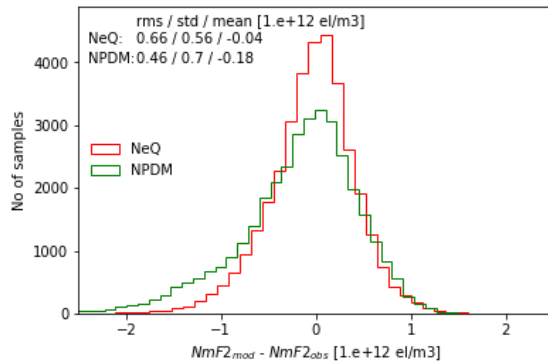


Fig.5.54. Histogram $NmF2_{mod}$ - $NmF2_{obs}$ at low latitude at high solar activity

5) Model statistics at medium latitude ($30\text{-}60^{\circ}\text{S}$)

- Low solar activity ($F10.7 = 60\text{-}100$ flux units)

At medium latitude at low solar activity the statistics parameters have almost the same values for both models.

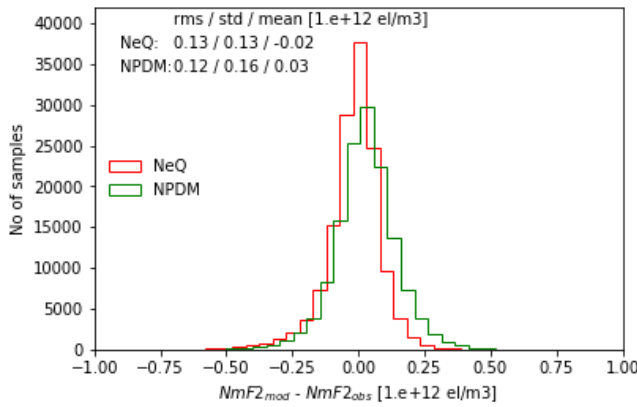


Fig.5.55. Histogram $NmF2_{mod} - NmF2_{obs}$ at medium latitude at low solar activity

- Medium solar activity ($F10.7 = 100\text{-}150$ flux units)

At medium latitude at medium solar activity NeQuick model has better values of the statistics parameters.

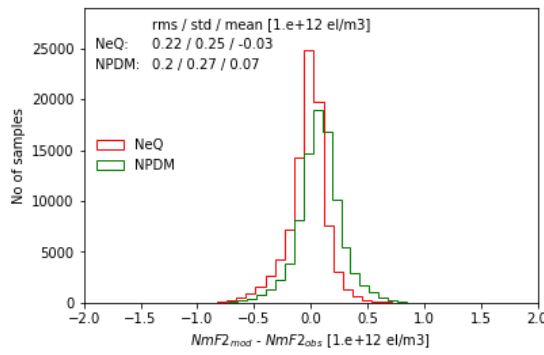


Fig.5.56. Histogram $NmF2_{mod} - NmF2_{obs}$ at medium latitude at medium solar activity

- High solar activity ($F10.7 = 150\text{-}200$ flux units)

At medium latitude at high solar activity NeQuick model has better values of the statistics parameters.

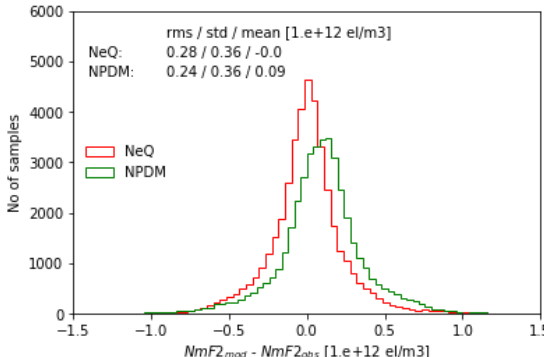


Fig.5.57. Histogram $NmF2_{mod} - NmF2_{obs}$ at medium latitude at high solar activity

6) Model statistics at high latitude ($60\text{-}90^\circ\text{S}$)

- Low solar activity ($F10.7 = 60\text{-}100$ flux units)

At high latitude at low solar activity the statistic parameters standard deviation (std) and mean value (mean) are better values for the NeQuick model.

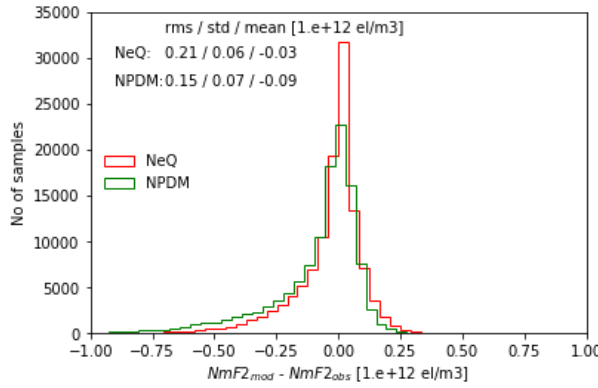


Fig.5.58. Histogram $NmF2_{mod} - NmF2_{obs}$ at high latitude at low solar activity

- Medium solar activity ($F10.7 = 100-150$ flux units)

At high latitude at medium solar activity the statistic parameters have almost the same values for both models.

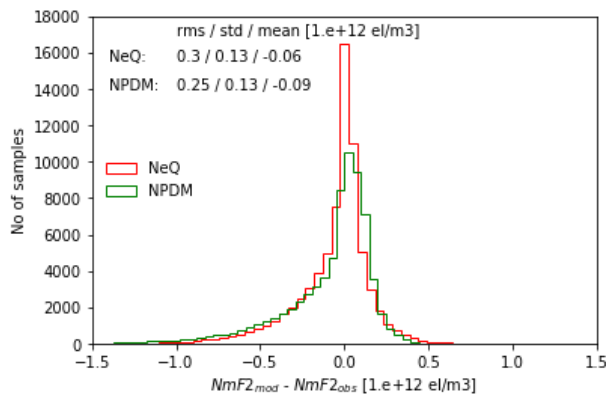


Fig.5.59. Histogram $NmF2_{mod} - NmF2_{obs}$ at high latitude at medium solar activity

- High solar activity ($F10.7 = 150-200$ flux units)

At high latitude at high solar activity the statistic parameters root mean square (rms) and standard deviation (std) are less for the NPDM model.

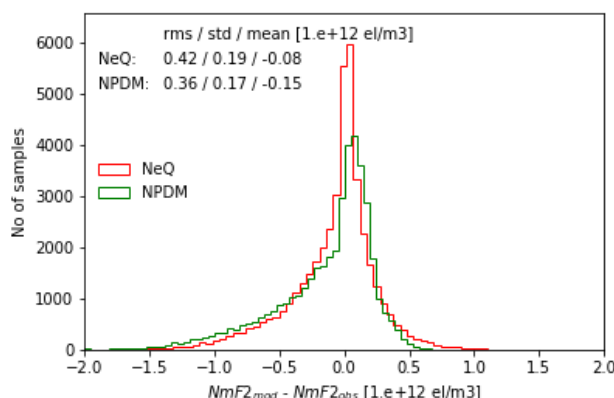


Fig.5.60. Histogram $NmF2_{mod} - NmF2_{obs}$ at high latitude at high solar activity

Chapter6. Model validation using space based data (IRO)

In this chapter we provide analysis of results of the recent described NPDM, NPHM and NeQuick models.

For our research we have used Ionospheric Radio Occultations (IRO) data during the time period from 2006 to 2017 years.

Mission	Periods
CHAMP	2011 – 2008
GRACE	2010 – 2010
COSMIC	2006 – 2017

6.1. Analysis of the peak electron density NmF2

Figures (6.1-6.18) show NmF2 comparisons among the IRO data, NPDM results and NeQuick estimates as a function of Universal Time (UT) and Day of Year at high, mid and low geographic latitudes at different solar activity.

All plots are generated using NPDM and NeQuick models at different latitudes at different solar activity. Also we have used filter for $NmF2_{obs}$, $0.01 \leq NmF2_{obs} \leq 15$ [$1.e+12 el/m^3$]. For analysis were used mean values. Bin size for day is 14. Local time is presented in range from 0 to 25. On the plots red color represent the ionosonde data ($NmF2_{obs}$), blue – the NPDM model ($NmF2_{mod}$), green – the NeQuick model and mistyrose – standard deviation (σ).

1. Model comparison at high latitude (60-90°N)
 - Low solar activity ($F10.7 = 60-100$ flux units)

At high latitude for diurnal and seasonal variations at low solar activity, the NeQuick model approximates to the RO data better than NPDM model.

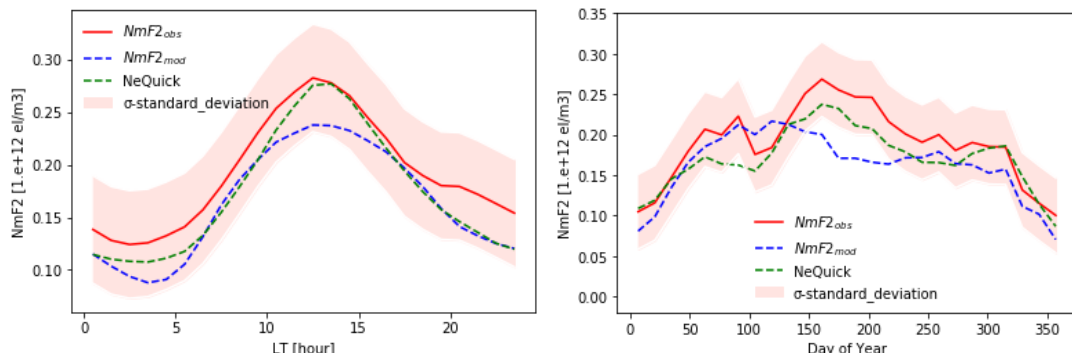


Fig.6.1. Diurnal and seasonal variations at high latitude at low solar activity

- Medium solar activity ($F10.7 = 100-150$ flux units)

At high latitude for diurnal variations at medium solar activity, the NPDM model approximates to the RO data better than NeQuick model. Regarding to the seasonal variations, both models have differences to the RO data.

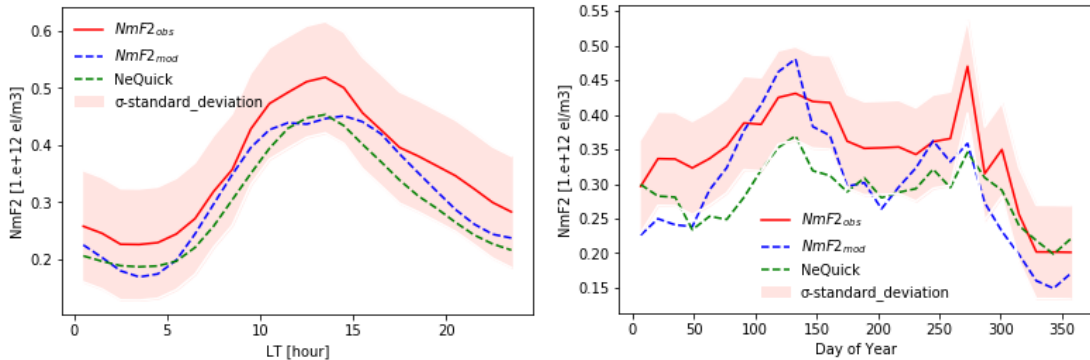


Fig.6.2. Diurnal and seasonal variations at high latitude at medium solar activity

- High solar activity ($F_{10.7} = 150\text{-}200$ flux units)

At high latitude for diurnal variations at high solar activity, NeQuick and NPDM models are similar to the RO data. Regarding to the seasonal variations, both models have some differences to the RO data.

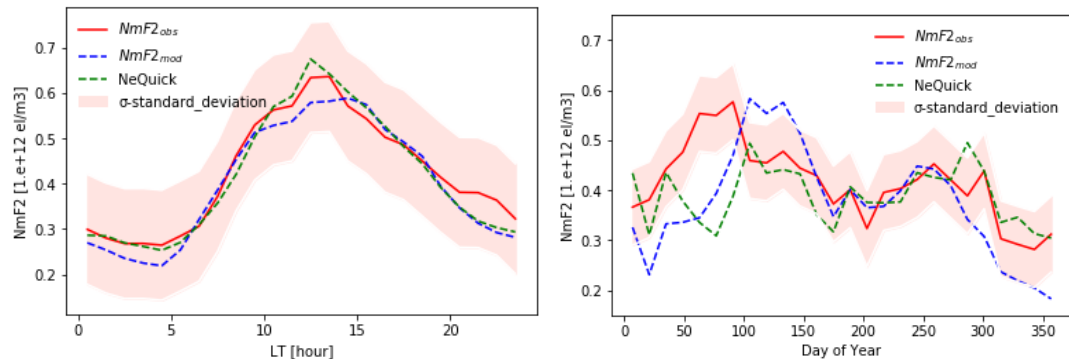


Fig.6.3. Diurnal and seasonal variations at high latitude at high solar activity

2. Model comparison at medium latitude ($30\text{-}60^\circ\text{N}$)

- Low solar activity ($F_{10.7} = 60\text{-}100$ flux units)

At medium latitude for diurnal variations at low solar activity, both models are very similar to the RO data. Regarding to the seasonal variations, NeQuick model approximates to the ionosonde data better than NPDM model, but there are some differences during summer period.

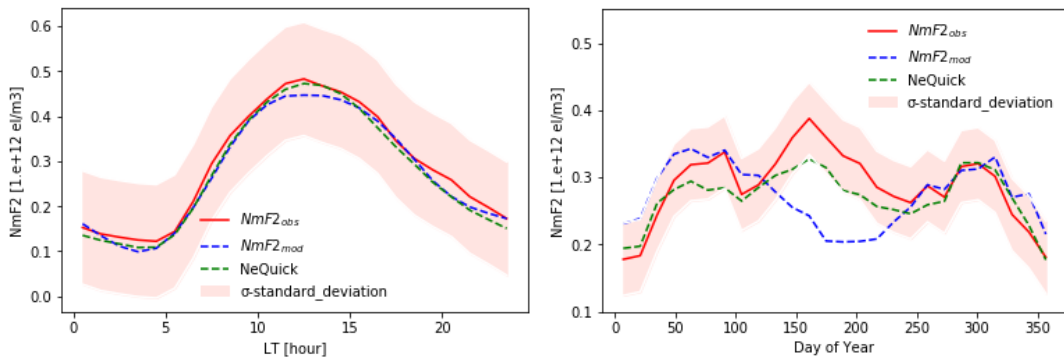


Fig.6.4. Diurnal and seasonal variations at medium latitude at low solar activity

- Medium solar activity ($F_{10.7} = 100\text{-}150$ flux units)

At medium latitude for diurnal variations at medium solar activity, the NeQuick and NPDM models are similar to the RO data. Regarding to the seasonal variations, both models have some differences to the RO data.

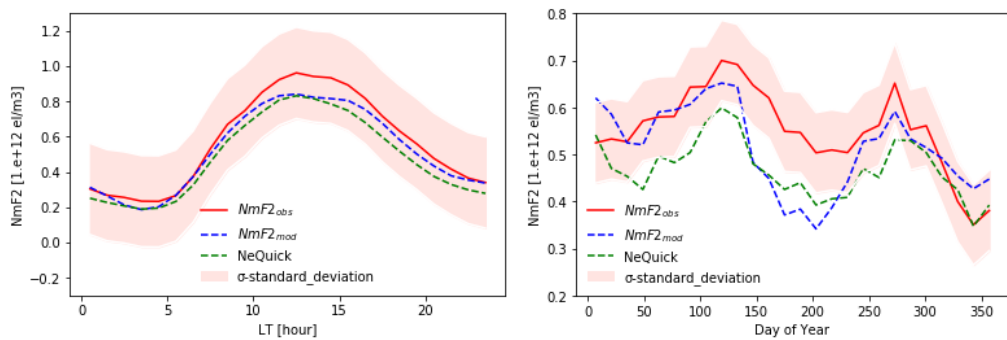


Fig.6.5. Diurnal and seasonal variations at medium latitude at medium solar activity

- High solar activity ($F_{10.7} = 150\text{-}200$ flux units)

At high latitude for diurnal variations at high solar activity both models are very similar to the RO data. Regarding to the seasonal variations, NeQuick and NPDM models have differences to the IRO data.

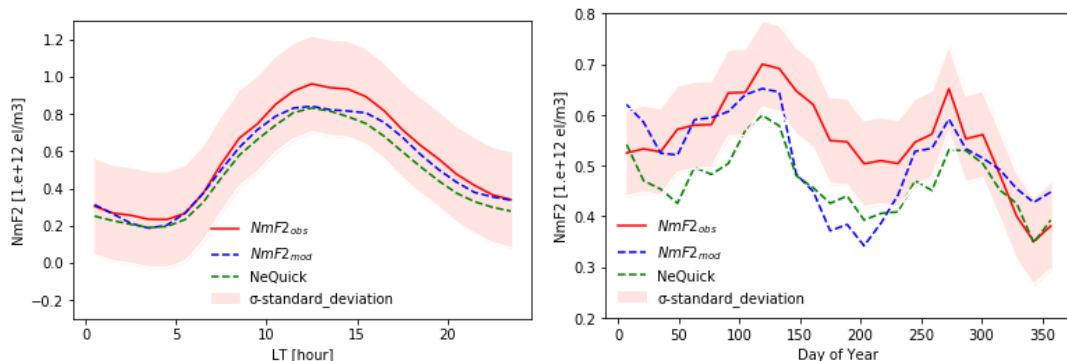


Fig.6.6. Diurnal and seasonal variations at medium latitude at high solar activity

3. Model comparison at low latitude (0-30°N)

- Low solar activity ($F_{10.7} = 60\text{-}100$ flux units)

At low latitude for diurnal and seasonal variations at low solar activity, the NPDM model approximates to the RO data better than NeQuick model.

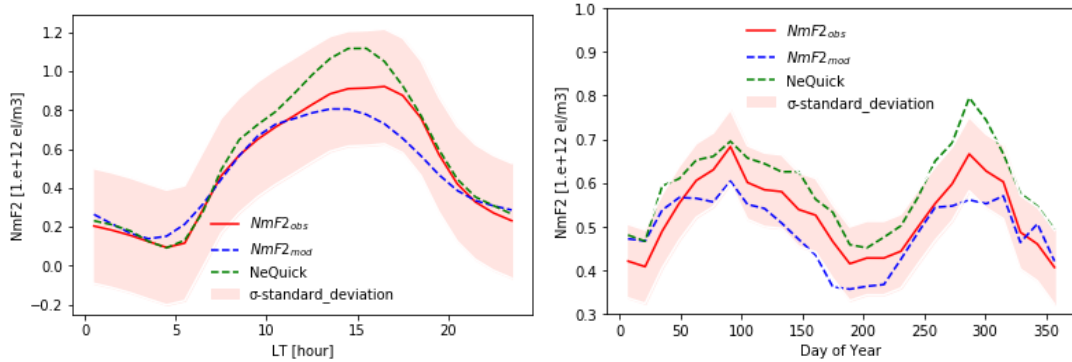


Fig.6.7.Diurnal and seasonal variations at low latitude at low solar activity

- Medium solar activity ($F_{10.7} = 100\text{-}150$ flux units)

At low latitude for diurnal variations at medium solar activity, the NeQuick model approximates to the RO data better than NPDM model. Regarding to the seasonal variations, NeQuick model approximates to the RO data better than NPDM model.

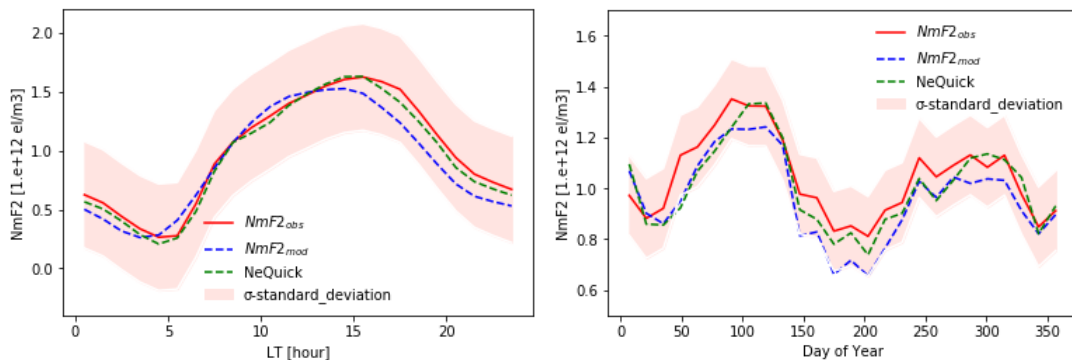


Fig.6.8. Diurnal and seasonal variations at low latitude at medium solar activity

- High solar activity ($F_{10.7} = 150\text{-}200$ flux units)

At low latitude for diurnal and seasonal variations at high solar activity, the NPDM model approximates to the RO data better than NeQuick model.

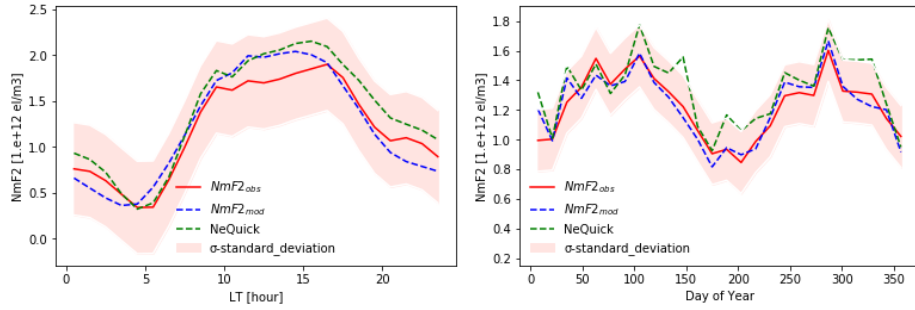


Fig.6.9. Diurnal and seasonal variations at low latitude at high solar activity

4. Model comparison at low latitude (0-30°S)

- Low solar activity ($F_{10.7} = 60\text{-}100$ flux units)

At low latitude for diurnal and seasonal variations at low solar activity, the NeQuick and NPDM models are similar to the RO data.

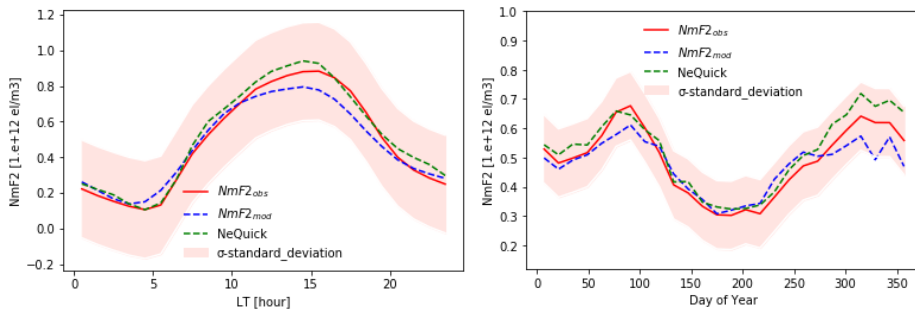


Fig.6.10. Diurnal and seasonal variations at low latitude at low solar activity

- Medium solar activity ($F_{10.7} = 100\text{-}150$ flux units)

At low latitude for diurnal and seasonal variations at medium solar activity, both models are similar to the RO data.

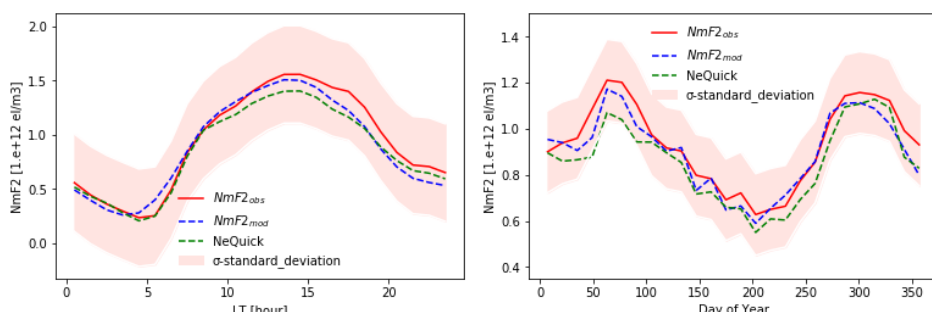


Fig.6.11. Diurnal and seasonal variations at low latitude at medium solar activity

- High solar activity ($F_{10.7} = 150\text{-}200$ flux units)

At low latitude for diurnal variations at high solar activity, the NeQuick model approximates to the RO data better than NPDM model. Regarding to the seasonal variations, NPDM model approximates to the RO data better than NeQuick model.

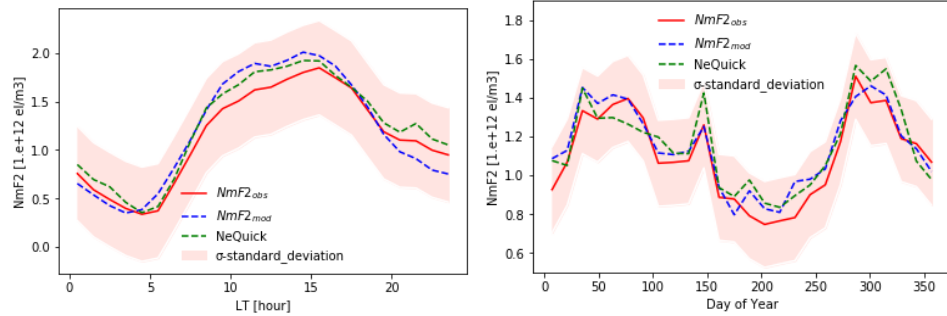


Fig.6.12. Diurnal and seasonal variations at low latitude at high solar activity

5. Model comparison at medium latitude ($30\text{-}60^\circ\text{S}$)

- Low solar activity ($F_{10.7} = 60\text{-}100$ flux units)

At medium latitude for diurnal variations at low solar activity, the NeQuick and NPDM models are similar to the RO data. Regarding to the seasonal variations, NeQuick model approximates to the RO data better than NPDM model.

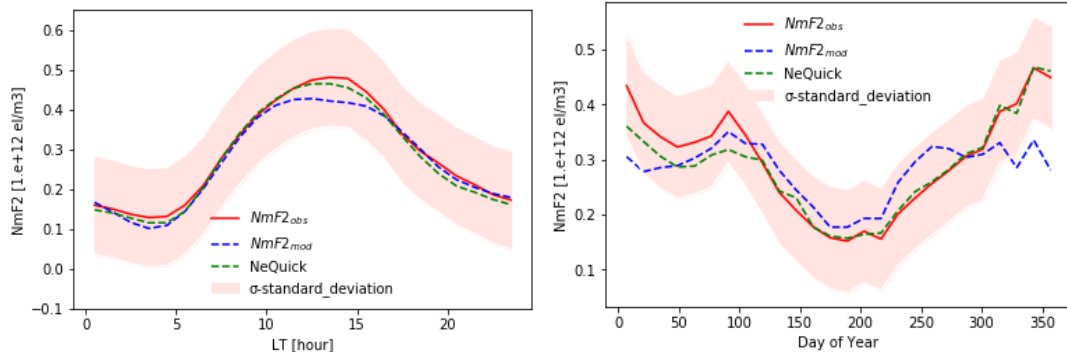


Fig.6.13. Diurnal and seasonal variations at medium latitude at low solar activity

- Medium solar activity ($F_{10.7} = 100\text{-}150$ flux units)

At medium latitude for diurnal variations at medium solar activity, the NPDM model approximates to the RO data better than NeQuick model. Regarding to the seasonal variations, both models have differences to the RO data.

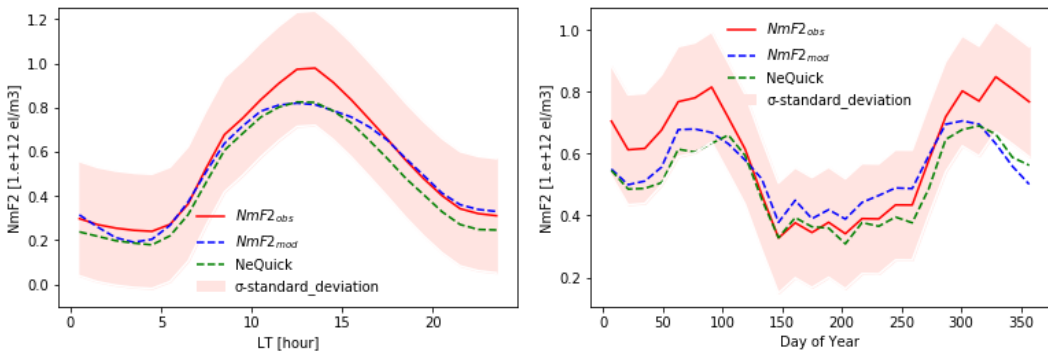


Fig.6.14. Diurnal and seasonal variations at medium latitude at medium solar activity

- High solar activity ($F_{10.7} = 150\text{-}200$ flux units)

At medium latitude for diurnal variations at high solar activity, the NeQuick model approximates to the RO data better than NPDM model. Regarding to the seasonal variations, the NeQuick and NPDM models have differences to the RO data..

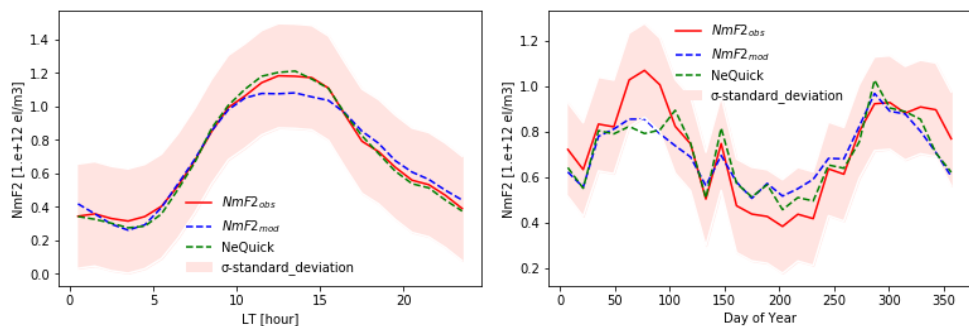


Fig.6.15. Diurnal and seasonal variations at medium latitude at high solar activity

6. Model comparison at high latitude ($60\text{-}90^\circ\text{S}$)

- Low solar activity ($F_{10.7} = 60\text{-}100$ flux units)

At high latitude for diurnal and seasonal variations at low solar activity, the NeQuick model approximates to the RO data better than NPDM model.

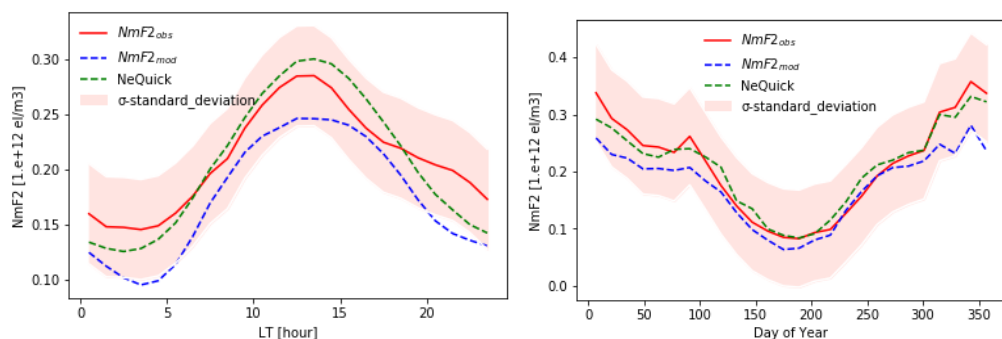


Fig.6.16. Diurnal and seasonal variations at high latitude at low solar activity

- Medium solar activity ($F_{10.7} = 100\text{-}150$ flux units)

At high latitude for diurnal variations at medium solar activity both models have differences to the RO data. Regarding to the seasonal variations, NPDM model approximates to the RO data better than NeQuick model.

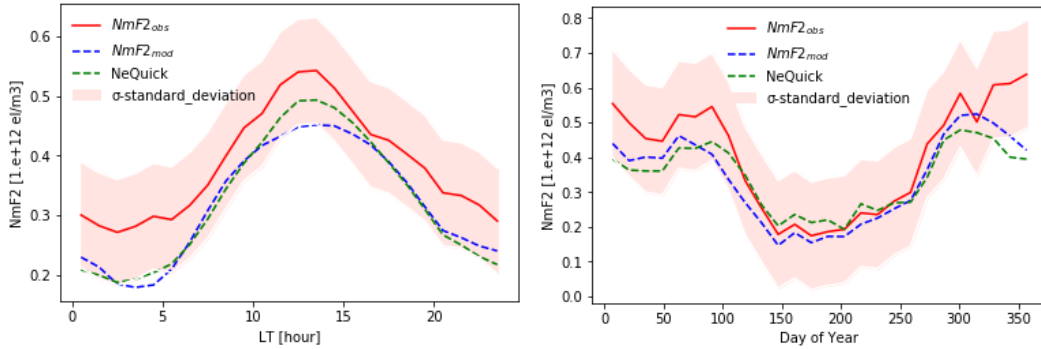


Fig.6.17. Diurnal and seasonal variations at high latitude at medium solar activity

- High solar activity ($F_{10.7} = 150\text{-}200$ flux units)

At high latitude for diurnal and seasonal variations at high solar activity, both models have differences to the RO data.

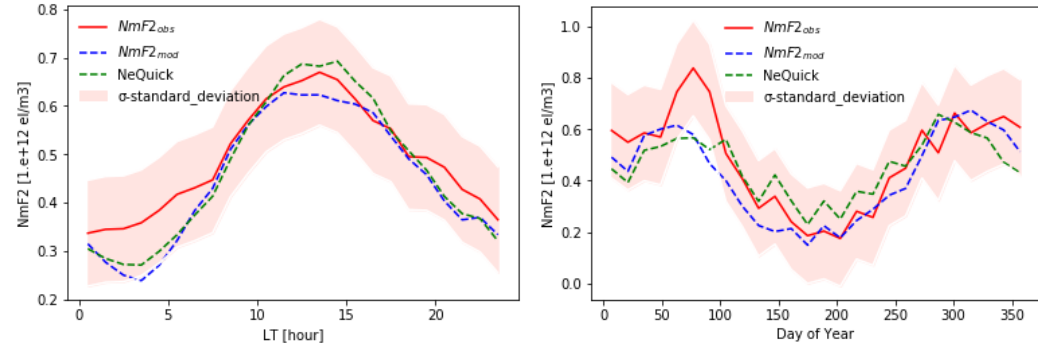


Fig.6.18. Diurnal and seasonal variations at high latitude at high solar activity

6.2. Analysis of the high peak electron density hmF2

Figures (6.19-6.36) show hmF2 comparisons among the IRO data, NPHM results and NeQuick estimates as a function of Universal Time (UT) and Day of Year at high, mid and low geographic latitudes at different solar activity.

1. Model comparison at high latitude ($60\text{-}90^\circ\text{N}$)

- Low solar activity ($F_{10.7} = 60\text{-}100$ flux units)

At high latitude for diurnal and seasonal variations at low solar activity, the NPHM model approximates to the RO data better than NeQuick model.

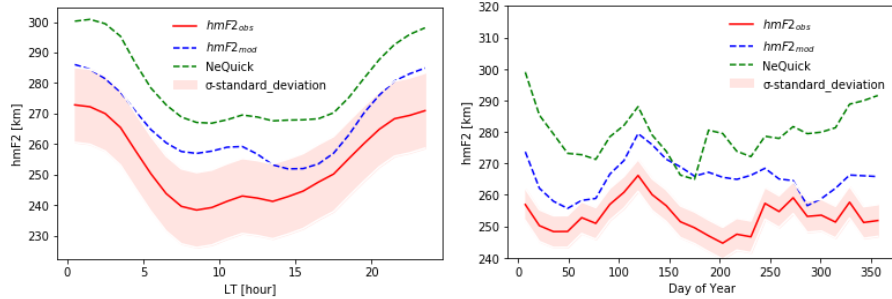


Fig.6.19. Diurnal and seasonal variations at high latitude for low solar activity

- Medium solar activity ($F_{10.7} = 100\text{-}150$ flux units)

At high latitude for diurnal and seasonal variations at medium solar activity, the NPHM model approximates to the RO data better than NeQuick model.

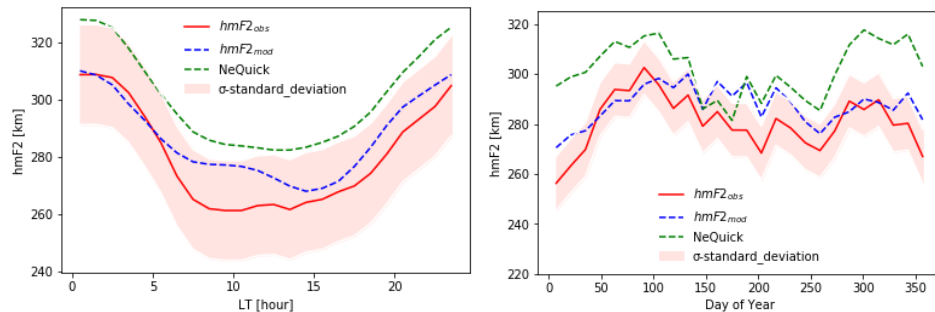


Fig.6.20. Diurnal and seasonal variations at high latitude for medium solar activity

- High solar activity ($F_{10.7} = 150\text{-}200$ flux units)

At high latitude for diurnal and seasonal variations at high solar activity, the NPHM model approximates to the RO data better than NeQuick model.

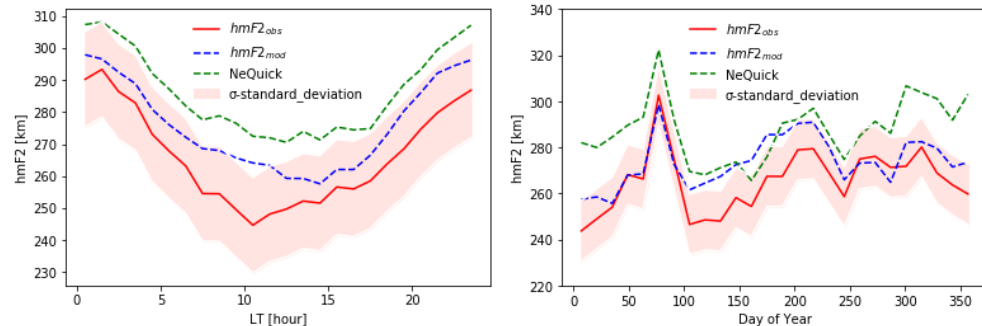


Fig.6.21. Diurnal and seasonal variations at high latitude for high solar activity

2. Model comparison at medium latitude ($30\text{-}60^\circ\text{N}$)

- Low solar activity ($F_{10.7} = 60\text{-}100$ flux units)

At medium latitude for diurnal and seasonal variations at low solar activity, the NPHM model approximates to the RO data better than NeQuick model.

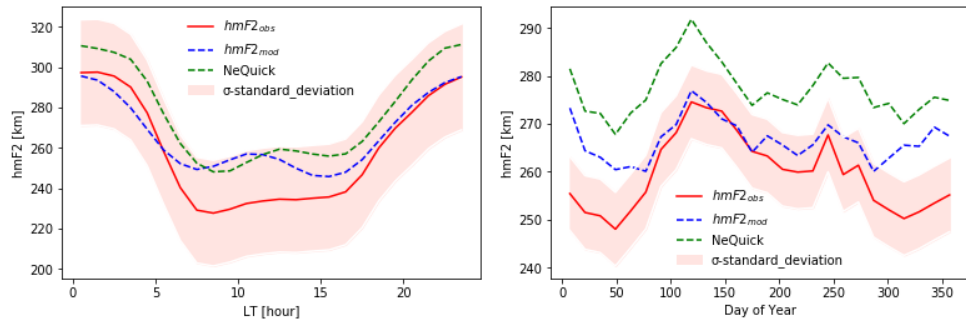


Fig.6.22. Diurnal and seasonal variations at medium latitude for low solar activity

- Medium solar activity ($F_{10.7} = 100\text{-}150$ flux units)

At medium latitude for diurnal and seasonal variations at medium solar activity, the NPHM model approximates to the RO data better than NeQuick model.

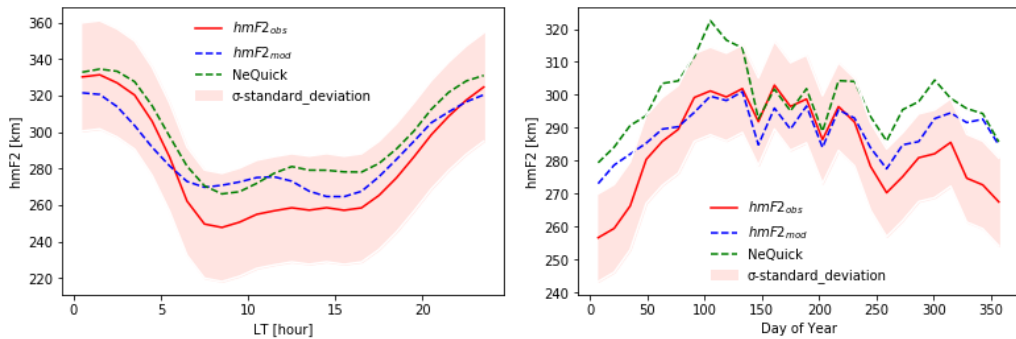


Fig.6.23. Diurnal and seasonal variations at medium latitude for medium solar activity

- High solar activity ($F_{10.7} = 150\text{-}200$ flux units)

At medium latitude for diurnal variations at high solar activity, the NPHM model approximates to the RO data better than NeQuick model. Regarding to the seasonal variations, NPHM model approximates to the RO data better than NeQuick model too.

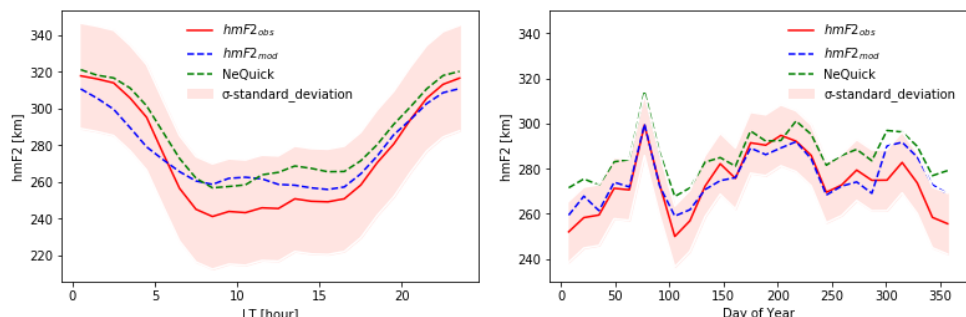


Fig.6.24. Diurnal and seasonal variations at medium latitude for high solar activity

3. Model comparison at low latitude ($0\text{-}30^\circ\text{N}$)

- Low solar activity ($F_{10.7} = 60\text{-}100$ flux units)

At low latitude for diurnal variations at low solar activity, the NPHM model approximates to the RO data better than NeQuick model. Regarding to the seasonal variations, NeQuick model approximates to the RO data better than NPHM model.

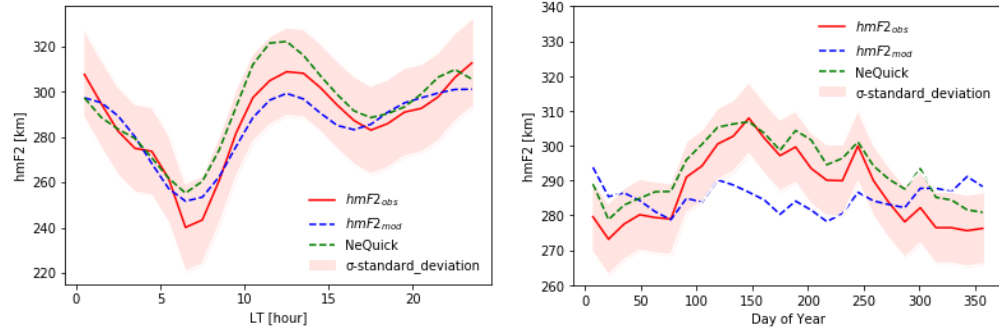


Fig.6.25. Diurnal and seasonal variations at low latitude for low solar activity

- Medium solar activity ($F_{10.7} = 100\text{-}150$ flux units)

At low latitude for diurnal variations at medium solar activity, the NeQuick model approximates to the RO data better than NPHM model. Regarding to the seasonal variations, NeQuick model approximates to the RO data better than NPHM model too.

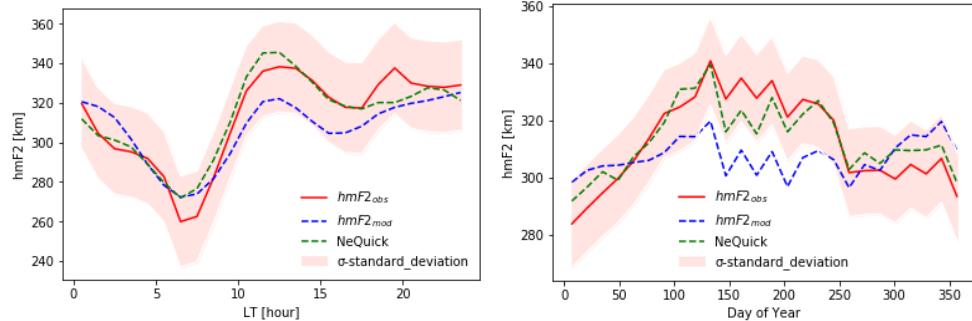


Fig.6.26. Diurnal and seasonal variations at low latitude for medium solar activity

- High solar activity ($F_{10.7} = 150\text{-}200$ flux units)

At low latitude for diurnal and seasonal variations at high solar activity, the NeQuick model approximates to the RO data better than NPHM model.

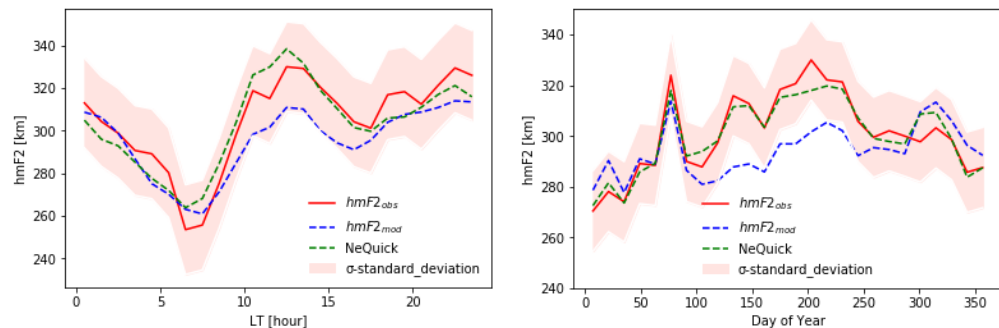


Fig.6.27. Diurnal and seasonal variations at low latitude for high solar activity

- 4. Model comparison at low latitude (0-30°S)
- Low solar activity ($F_{10.7} = 60\text{-}100$ flux units)

At low latitude for diurnal variations at low solar activity, the NPHM model approximates to the RO data better than NeQuick model. Regarding to the seasonal variations, NeQuick model approximates to the RO data better than NPHM model.

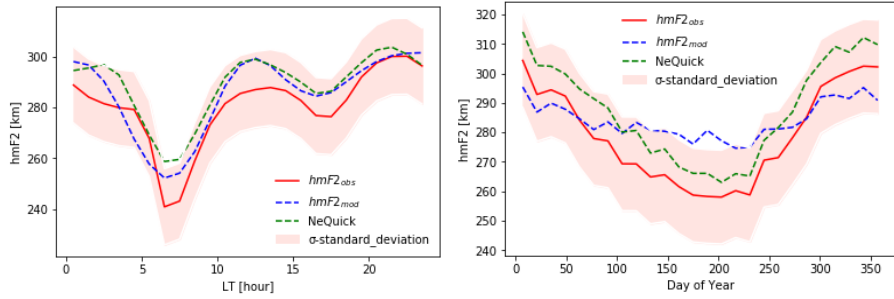


Fig.6.28. Diurnal and seasonal variations at low latitude for low solar activity

- Medium solar activity ($F_{10.7} = 100\text{-}150$ flux units)

At low latitude for diurnal variations at medium solar activity, the NeQuick model approximates to the RO data better than NPHM model. Regarding to the seasonal variations, NeQuick model approximates to the RO data better than NPHM model.

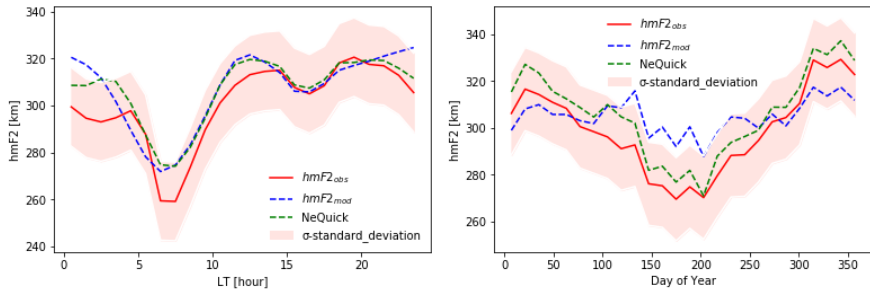


Fig.6.29. Diurnal and seasonal variations at low latitude for medium solar activity

- High solar activity ($F_{10.7} = 150\text{-}200$ flux units)

At low latitude for diurnal and seasonal variations at high solar activity, the NeQuick model approximates to the RO data better than NPHM model.

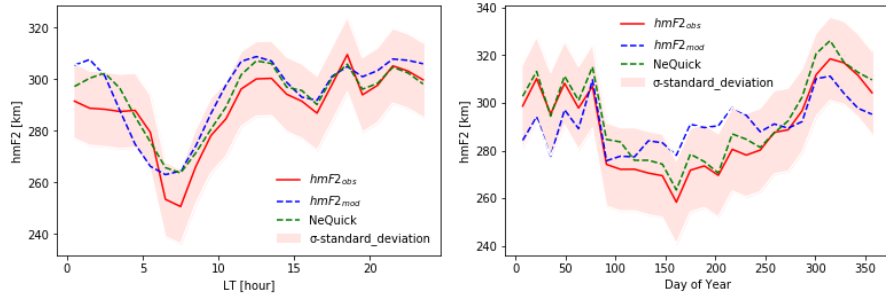


Fig.6.30. Diurnal and seasonal variations at low latitude for high solar activity

5. Model comparison at medium latitude (30-60°S)

- Low solar activity (F10.7 = 60-100 flux units)

At medium latitude for diurnal and seasonal variations at low solar activity, the NPHM model approximates to the RO data better than NeQuick model.

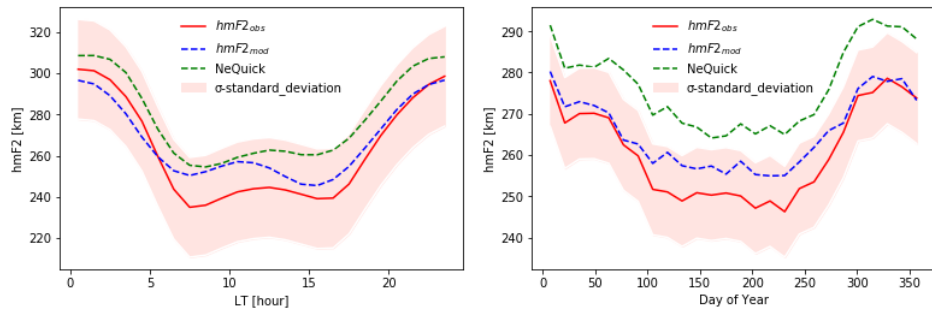


Fig.6.31. Diurnal and seasonal variations at medium latitude for low solar activity

- Medium solar activity (F10.7 = 100-150 flux units)

At medium latitude for diurnal variations at medium solar activity, the NPHM model approximates to the RO data better than NeQuick model. Regarding to the seasonal variations, NPHM model approximates to the RO data better than NeQuick model too.

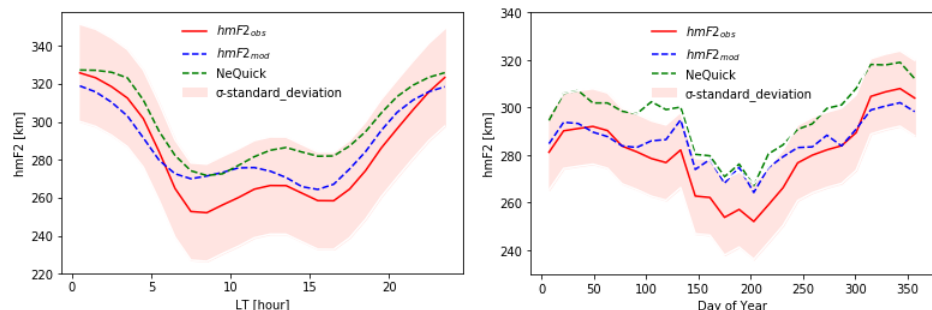


Fig.6.32. Diurnal and seasonal variations at medium latitude for medium solar activity

- High solar activity (F10.7 = 150-200 flux units)

At medium latitude for diurnal and seasonal variations at high solar activity, the NPHM model approximates to the RO data better than NeQuick model.

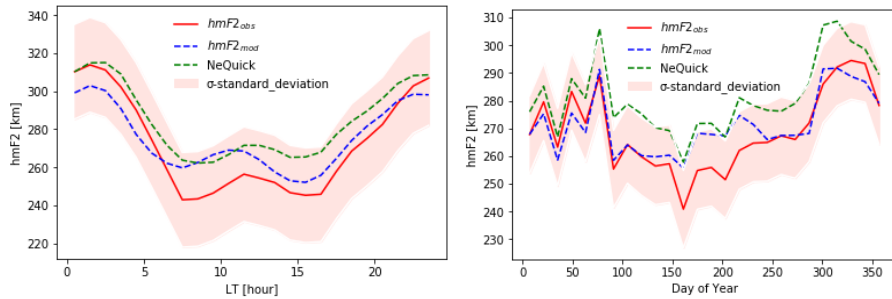


Fig.6.33. Diurnal and seasonal variations at medium latitude for high solar activity

6. Model comparison at high latitude (60-90°S)

- Low solar activity ($F_{10.7} = 60\text{-}100$ flux units)

At high latitude for diurnal and seasonal variations at low solar activity, the NPHM model approximates to the RO data better than NeQuick model.

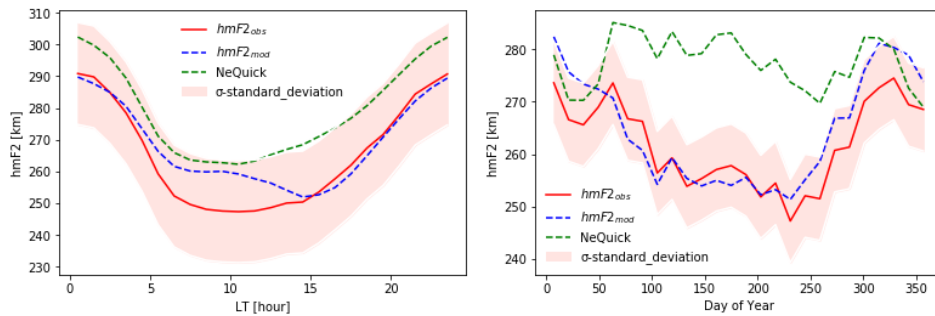


Fig.6.34. Diurnal and seasonal variations at high latitude for low solar activity

- Medium solar activity ($F_{10.7} = 100\text{-}150$ flux units)

At high latitude for diurnal and seasonal variations at medium solar activity, the NPHM model approximates to the RO data better than NeQuick model.

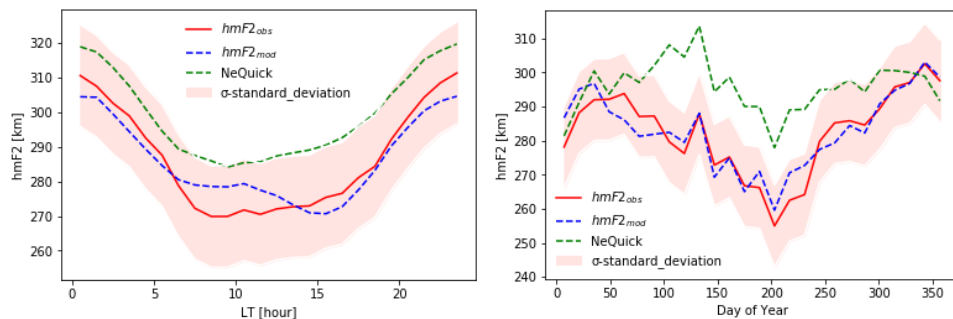


Fig.6.35. Diurnal and seasonal variations at high latitude for medium solar activity

- High solar activity ($F_{10.7} = 150\text{-}200$ flux units)

At high latitude for diurnal and seasonal variations at high solar activity, the NPHM model approximates to the RO data better than NeQuick model.

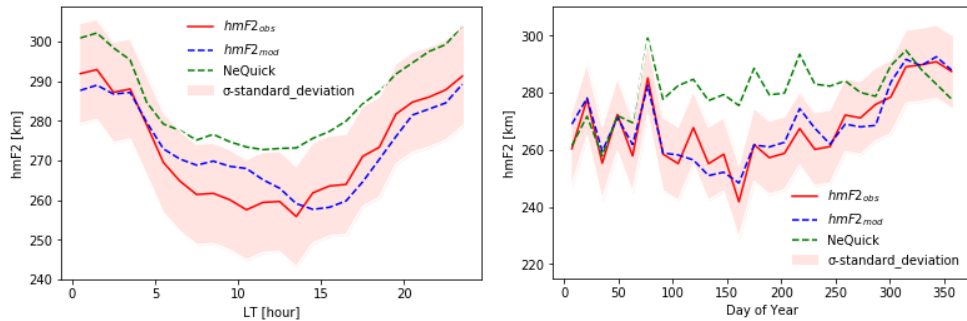


Fig.6.36. Diurnal and seasonal variations at high latitude for high solar activity

6.3. The statistic for $NmF2_{mod}$ - $NmF2_{obs}$ and $hmF2_{mod}$ - $hmF2_{obs}$

To compare again both models performance, we have computed the differences between RO data and model results for all hourly values (of $NmF2$ and $hmF2$) and estimated the RMS of differences at each selected geographic region for the selected periods.

The NPDM, NPHM and NeQuick $NmF2_{mod}$ - $NmF2_{obs}$ and $hmF2_{mod}$ - $hmF2_{obs}$ estimates are calculated at the same location and time window for comparison. The histograms of differences are shown in Fig. (6.36-6.53). The corresponding RMS, mean deviation and standard deviation of $NmF2_{mod}$ - $NmF2_{obs}$ and $hmF2_{mod}$ - $hmF2_{obs}$ differences are also given in Fig.(6.36-6.53).

Table.5.17. RMS values for IRO data at different latitudes at different solar activity

	rms [$1e+11 el/m^3$] $NmF2$		rms [km] $hmF2$	
	NeQ	NPDM	NeQ	NPHM
60-90°N				
Low solar activity ($F10.7 = 60-100$ flux units)	1.8	1.8	30.35	38.34
Medium solar activity ($F10.7 = 100-150$ flux units)	2.6	2.5	33.23	38.02
High solar activity ($F10.7 = 150-200$ flux units)	3.0	2.8	31.46	35.7
30-60°N				
Low solar activity ($F10.7 = 60-100$ flux units)	2.5	2.4	27.32	29.15
Medium solar activity ($F10.7 = 100-150$ flux units)	3.2	3.1	29.86	29.51
High solar activity ($F10.7 = 150-200$ flux units)	3.4	3.2	28.98	27.87
0-30°N				
Low solar activity ($F10.7 = 60-100$ flux units)	3.1	3.1	37.8	33.57
Medium solar activity ($F10.7 = 100-150$ flux units)	4.2	3.9	43.03	35.68

High solar activity (F10.7 = 150-200 flux units)	5.1	5.2	41.7	35.45
0-30°S				
Low solar activity (F10.7 = 60-100 flux units)	3.0	2.9	36.35	34.38
Medium solar activity (F10.7 = 100-150 flux units)	3.8	3.6	40.51	35.56
High solar activity (F10.7 = 150-200 flux units)	4.7	4.5	39.47	34.59
30-60°S				
Low solar activity (F10.7 = 60-100 flux units)	2.6	2.4	29.77	30.82
Medium solar activity (F10.7 = 100-150 flux units)	3.2	3.0	34.15	33.01
High solar activity (F10.7 = 150-200 flux units)	3.7	3.3	33.13	31.49
60-90°S				
Low solar activity (F10.7 = 60-100 flux units)	1.7	1.6	38.13	37.68
Medium solar activity (F10.7 = 100-150 flux units)	2.6	2.5	43.2	41.37
High solar activity (F10.7 = 150-200 flux units)	3.1	2.9	39.8	39.3

7) Model statistics at low latitude (60-90°N)

➤ Low solar activity (F10.7 = 60-100 flux units)

At high latitude at low solar activity the statistic parameters root mean square (rms), standard deviation (std) and mean value (mean) have almost the same values for the NeQuick and NPDM models. Comparing NPHM and NeQuick models, we see that for the NPHM model standard deviation and mean values are less.

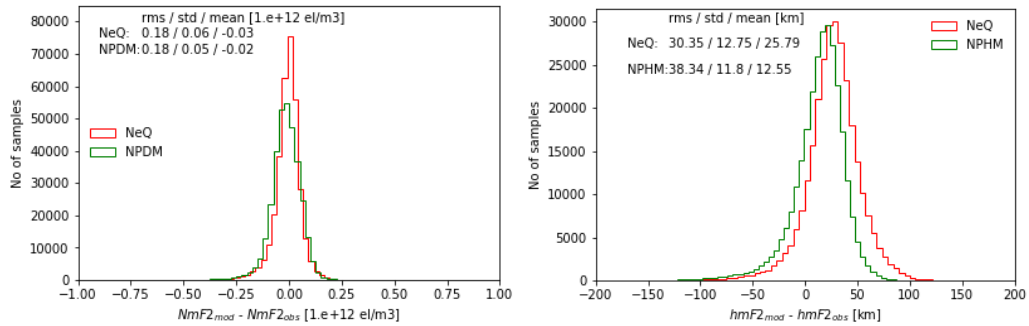


Fig.6.37. Histogram $NmF2_{mod} - NmF2_{obs}$ and $hmF2_{mod} - hmF2_{obs}$ at high latitude at low solar activity

➤ Medium solar activity (F10.7 = 100-150 flux units)

At high latitude at medium solar activity the statistic parameters root mean square (rms), standard deviation (std) and mean value (mean) have almost the same values for the

NeQuick and NPDM models. Comparing NPHM and NeQuick models, we see that for NPHM standard deviation and mean values are less.

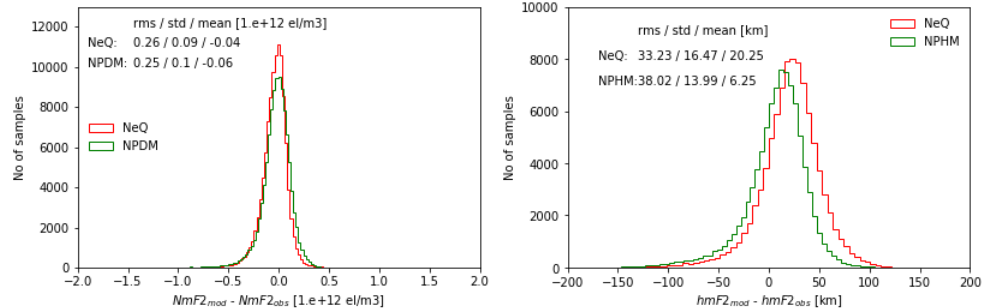


Fig.6.38. Histogram $NmF2_{mod} - NmF2_{obs}$ and $hmF2_{mod} - hmF2_{obs}$ at high latitude at medium solar activity

- High solar activity ($F10.7 = 150-200$ flux units)

At high latitude at high solar activity the statistic parameters root mean square (rms), standard deviation (std) and mean value (mean) have almost the same values for the NeQuick and NPDM models. Comparing NPHM and NeQuick models, we see that for the NeQuick model root mean square and standard deviation values are less.

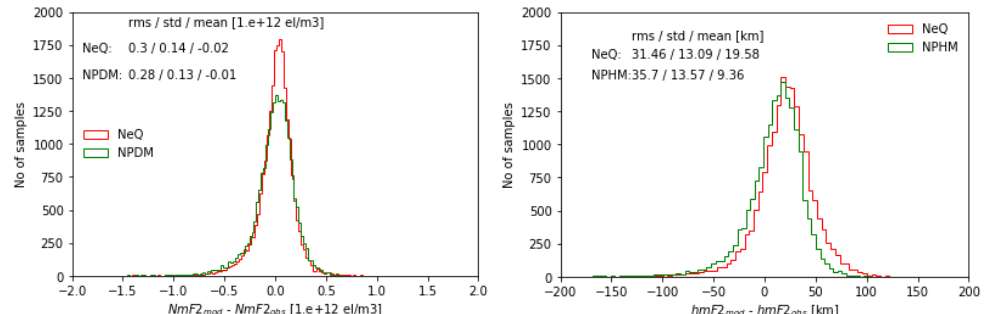


Fig.6.39. Histogram $NmF2_{mod} - NmF2_{obs}$ and $hmF2_{mod} - hmF2_{obs}$ at high latitude at high solar activity

8) Model statistics at medium latitude ($30-60^{\circ}\text{N}$)

- Low solar activity ($F10.7 = 60-100$ flux units)

At medium latitude at low solar activity the statistic parameters root mean square (rms), standard deviation (std) and mean value (mean) have almost the same values for the NeQuick and NPDM models. Comparing the NPHM and NeQuick models, we see that for the NPHM root mean square and standard deviation values are less.

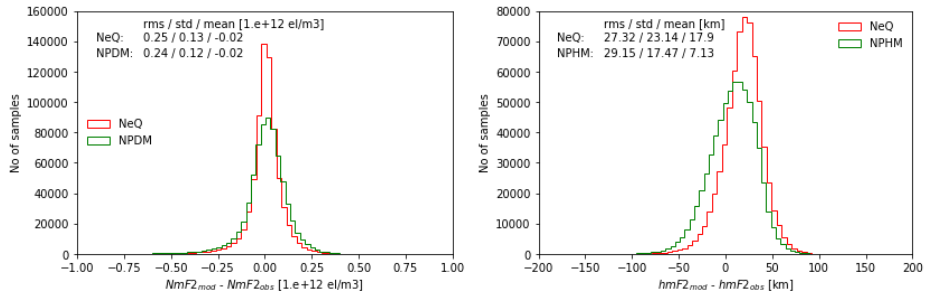


Fig. 6.40. Histogram $NmF2_{mod} - NmF2_{obs}$ and $hmF2_{mod} - hmF2_{obs}$ at medium latitude at low solar activity

➤ Medium solar activity ($F10.7 = 100\text{-}150$ flux units)

At medium latitude at low solar activity the statistic parameters root mean square (rms), standard deviation (std) have almost the same values for the NeQuick and NPDM models. Comparing the NPHM and NeQuick models, we see that for the NPHM model root mean square and standard deviation values are less.

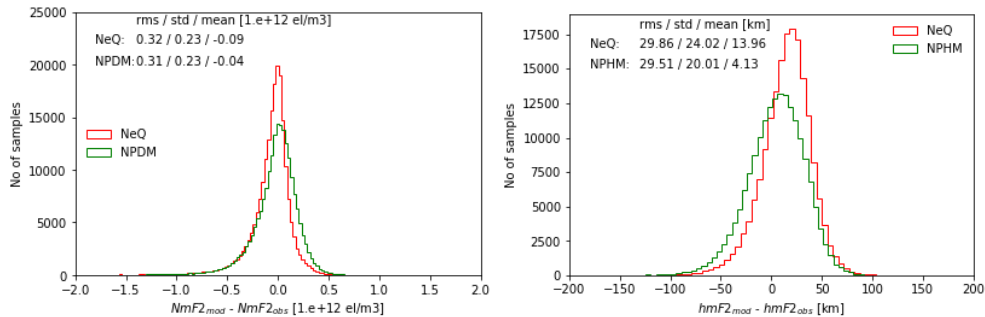


Fig. 6.41. Histogram $NmF2_{mod} - NmF2_{obs}$ and $hmF2_{mod} - hmF2_{obs}$ at medium latitude at medium solar activity

➤ High solar activity ($F10.7 = 150\text{-}200$ flux units)

At medium latitude at high solar activity the statistic parameters root mean square (rms) and standard deviation (std) are less for NPDM model. Comparing the NPHM and NeQuick models, we see that for the NPHM root mean square, standard deviation and mean values are less than for the NeQuick model.

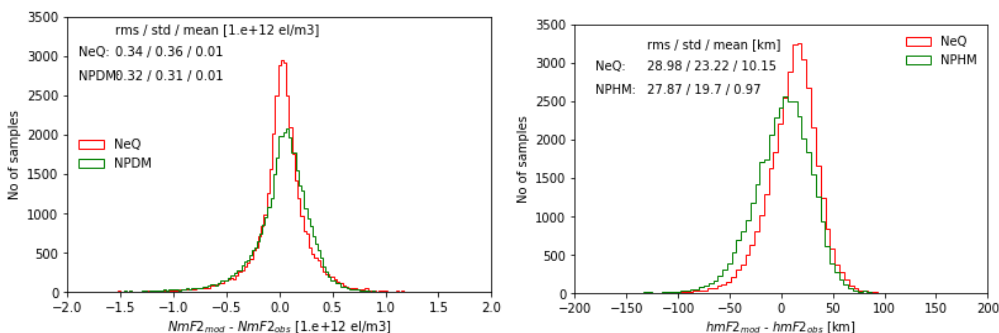


Fig. 6.42. Histogram $NmF2_{mod} - NmF2_{obs}$ and $hmF2_{mod} - hmF2_{obs}$ at medium latitude at high solar activity

- 9) Model statistics at low latitude (0-30°N)
- Low solar activity (F10.7 = 60-100 flux units)

At low latitude at low solar activity the statistic parameter root mean square (rms) is the same for the NeQuick and NPDM models, standard deviation (std) is less for the NPDM model and mean value (mean) is less for the NeQuick. Comparing the NPHM and NeQuick models, we see that the NPHM model has better statistics.

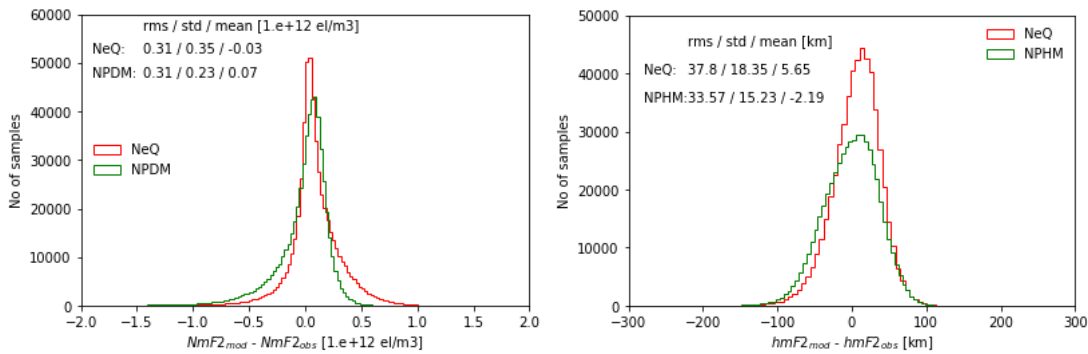


Fig.6.43. Histogram $NmF2_{mod}$ - $NmF2_{obs}$ and $hmF2_{mod}$ - $hmF2_{obs}$ at low latitude at low solar activity

- Medium solar activity (F10.7 = 100-150 flux units)

At low latitude at medium solar activity the statistic parameters root mean square (rms), standard deviation (std) and mean value (mean) have better values for the NPDM model. Comparing the NPHM and NeQuick models, we see that for NPHM root mean square and standard deviation values are less than for NeQuick model.

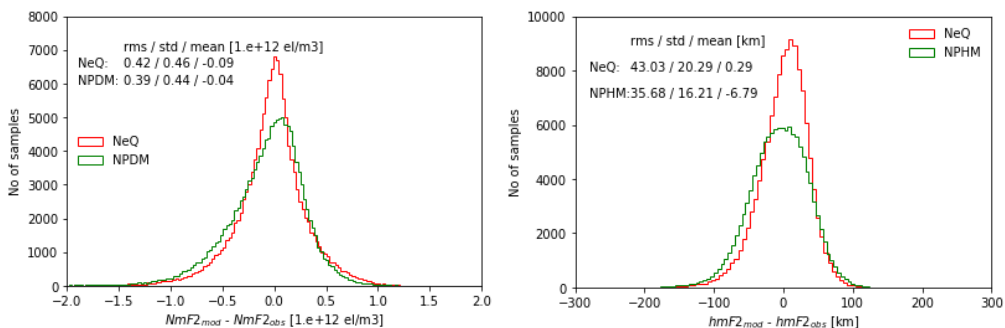


Fig.6.44. Histogram $NmF2_{mod}$ - $NmF2_{obs}$ and $hmF2_{mod}$ - $hmF2_{obs}$ at low latitude at medium solar activity

- High solar activity (F10.7 = 150-200 flux units)

At low latitude at high solar activity the statistic parameters root mean square (rms), standard deviation (std) and mean value (mean) are better for NeQuick model. Comparing the NPHM and NeQuick models, we see that for the NPHM root mean square

and standard deviation values are less for the NPHM model, and mean values are less for the NeQuick model.

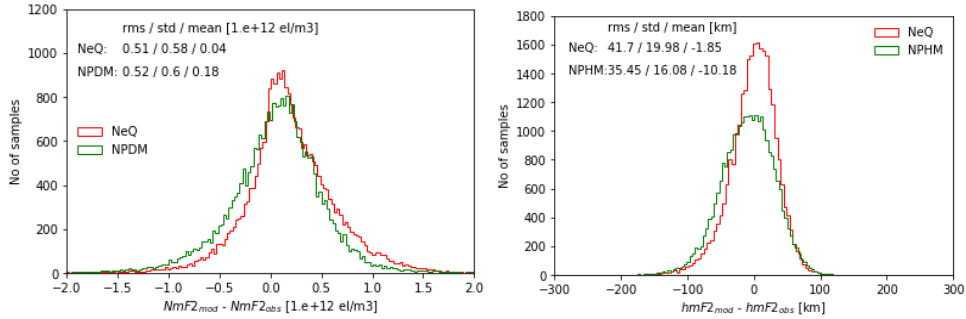


Fig.6.45. Histogram $NmF2_{mod} - NmF2_{obs}$ and $hmF2_{mod} - hmF2_{obs}$ at low latitude at high solar activity

- 10) Model statistics at low latitude ($0-30^{\circ}$ S)
- Low solar activity ($F10.7 = 60-100$ flux units)

At low latitude at low solar activity the statistic parameters root mean square (rms), standard deviation (std) are better for the NPDM models and mean value (mean) has less value for the NeQuick model. Comparing the NPHM and NeQuick models, we see that for the NPHM root mean square and mean values are less than for the NeQuick model.

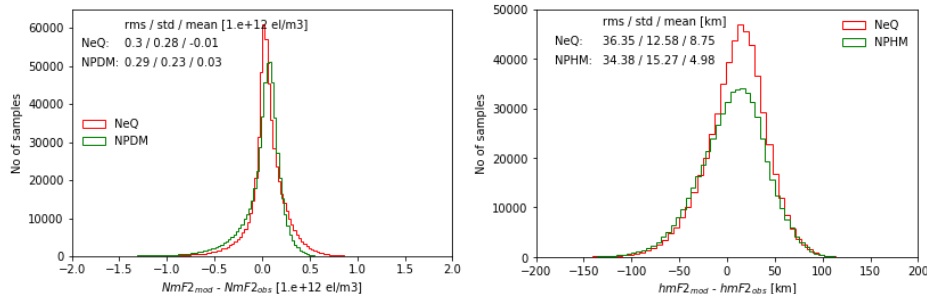


Fig.6.46. Histogram $NmF2_{mod} - NmF2_{obs}$ and $hmF2_{mod} - hmF2_{obs}$ at low latitude at low solar activity

- Medium solar activity ($F10.7 = 100-150$ flux units)

At low latitude at medium solar activity the statistic parameters root mean square (rms) and standard deviation (std) are better for the NeQuick. Comparing the NPHM and NeQuick models, we see that for the NPHM model root mean square and mean values are less than for the NeQuick model.

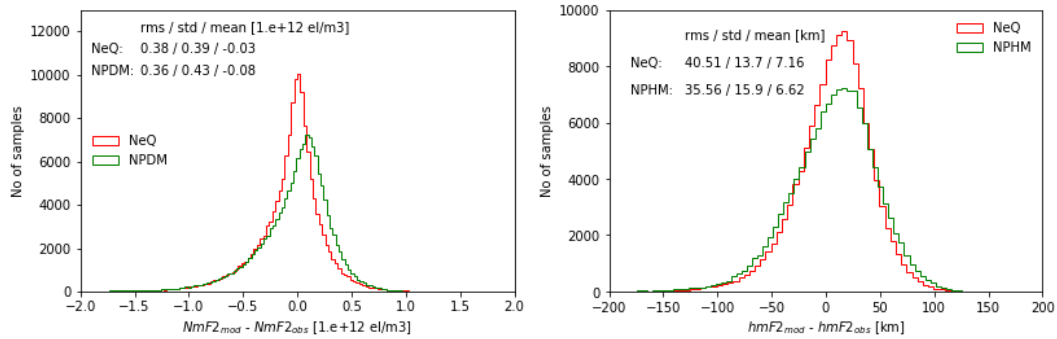


Fig. 6.47. Histogram NmF2_{mod}-NmF2_{obs} and hmF2_{mod}-hmF2_{obs} at low latitude at medium solar activity

- High solar activity ($F_{10.7} = 150\text{-}200$ flux units)

At low latitude at high solar activity the statistic parameter root mean square (rms) is less for the NPDM model and two other parameters standard deviation (std) and mean value (mean) have less values for the NeQuick model. Comparing the NPHM and NeQuick models, we see that for the NPHM model statistic parameters standard deviation and mean values are less for the NeQuick model.

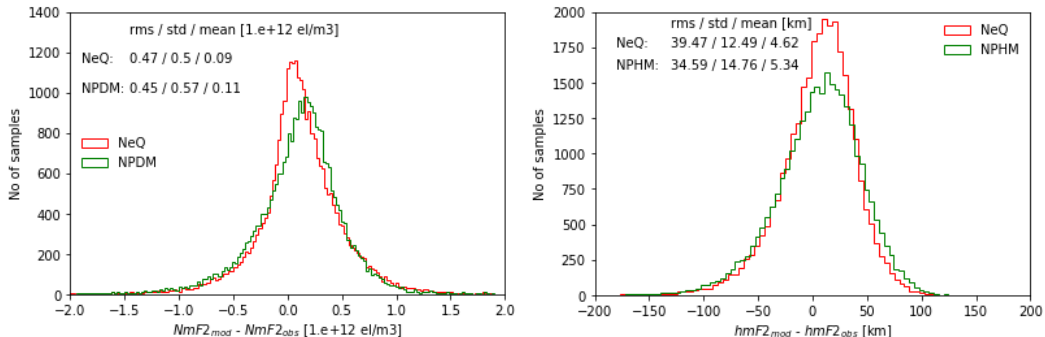
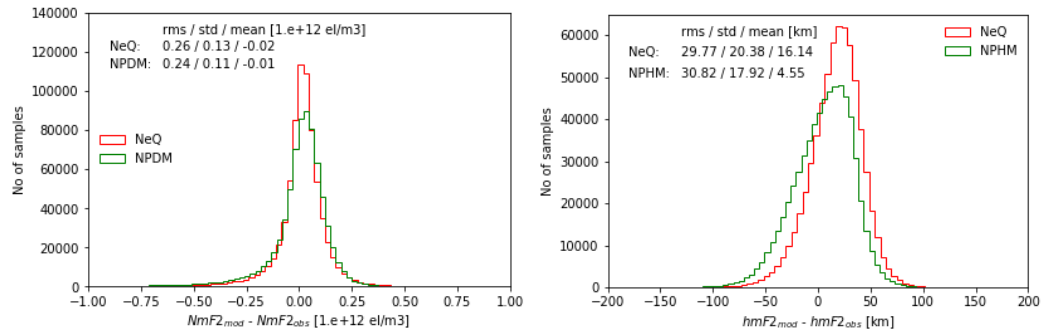


Fig. 6.48. Histogram NmF2_{mod}-NmF2_{obs} and hmF2_{mod}-hmF2_{obs} at low latitude at high solar activity

11) Model statistics at medium latitude (30-60°S)

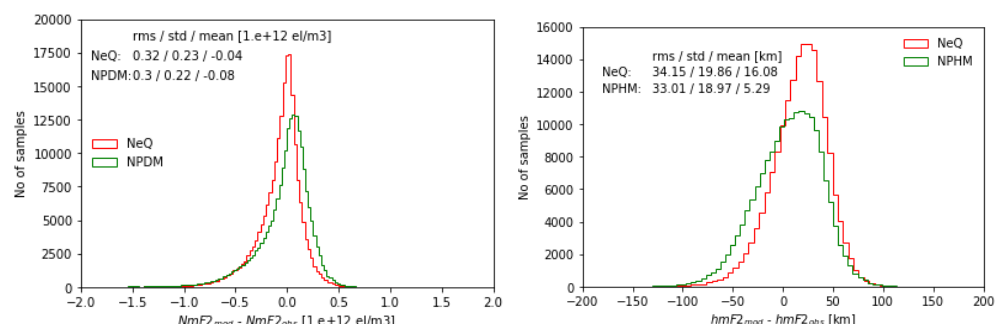
- Low solar activity ($F_{10.7} = 60\text{-}100$ flux units)

At medium latitude at low solar activity the statistics parameter root mean square (rms) and standard deviation (std) are less for the NPDM model. Comparing the NPHM and NeQuick models, we see that for the NPHM statistic parameters standard deviation and mean values have better values than the NeQuick model.



- Medium solar activity ($F10.7 = 100-150$ flux units)

At medium latitude at medium solar activity the statistics parameter root mean square (rms), standard deviation (std) and mean value (mean) are less for the NPDM model. Comparing the NPHM and NeQuick models, we see that for the NPHM statistic parameters standard deviation and mean values have better values than the NeQuick model.



- High solar activity ($F10.7 = 150-200$ flux units)

At medium latitude at high solar activity the statistics parameter root mean square (rms), standard deviation (std) and mean value (mean) are better for the NPDM model. Comparing the NPHM and NeQuick models, we see that the NPHM model has better statistic parameters.

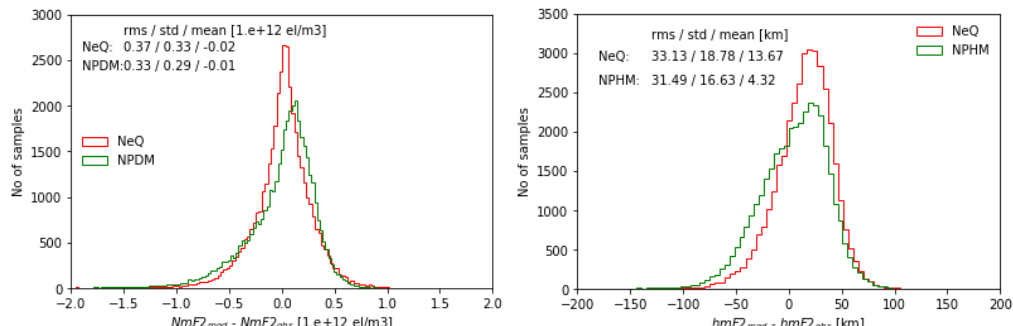


Fig.6.51. Histogram $NmF2_{mod}$ - $NmF2_{obs}$ and $hmF2_{mod}$ - $hmF2_{obs}$ at medium latitude at high solar activity

12) Model statistics at high latitude (60-90°S)

- Low solar activity ($F10.7 = 60-100$ flux units)

At high latitude at low solar activity the statistics parameter root mean square (rms), standard deviation (std) and mean value (mean) are better for the NPDM model. Comparing the NPHM and NeQuick models, we see that the NPHM model shows better statistics parameters.

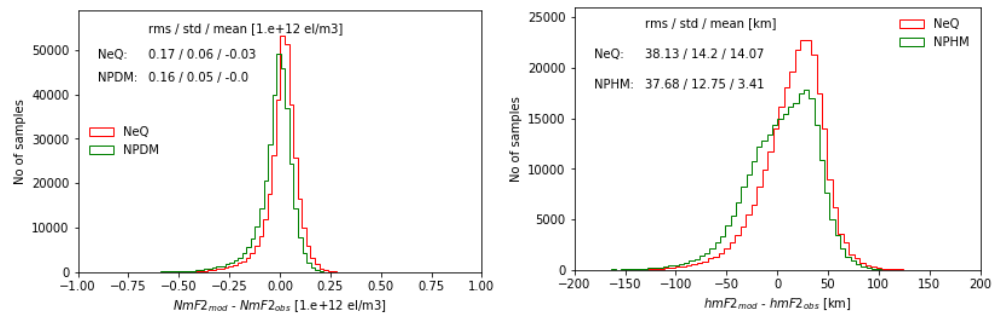


Fig.6.52. Histogram $NmF2_{mod}$ - $NmF2_{obs}$ and $hmF2_{mod}$ - $hmF2_{obs}$ at high latitude at low solar activity

- Medium solar activity ($F10.7 = 100-150$ flux units)

At high latitude at medium solar activity the statistics parameter root mean square (rms) and standard deviation (std) are less for the NPDM model. Comparing the NPHM and NeQuick models, we see that the NPHM model shows better statistics parameters.

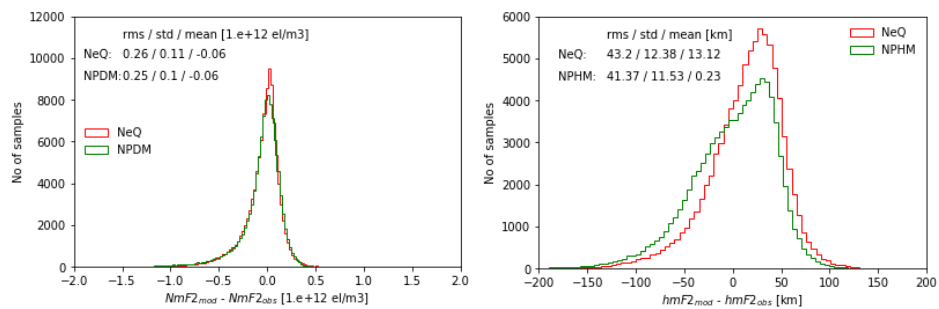


Fig.6.53. Histogram $NmF2_{mod}$ - $NmF2_{obs}$ and $hmF2_{mod}$ - $hmF2_{obs}$ at high latitude at medium solar activity

- High solar activity ($F10.7 = 150-200$ flux units)

At high latitude at high solar activity the statistics parameter root mean square (rms), standard deviation (std) and mean value (mean) are less for the NPDM model. Comparing the NPHM and NeQuick models, we see that the NPHM model shows better statistics parameters.

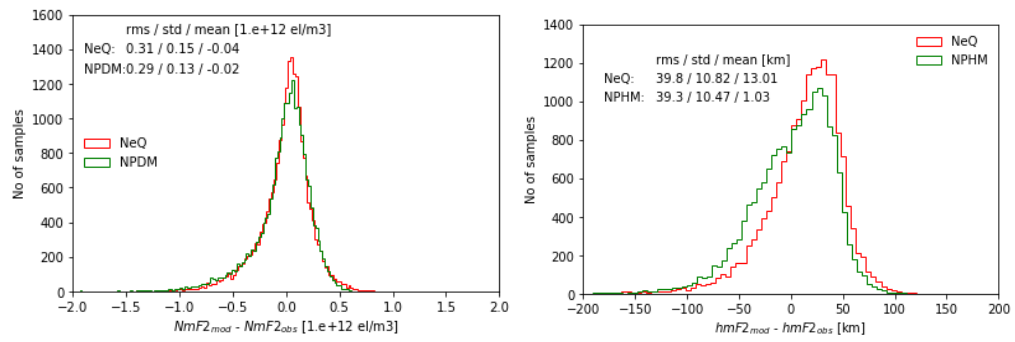


Fig. 6.54. Histogram $NmF2_{mod} - NmF2_{obs}$ and $hmF2_{mod} - hmF2_{obs}$ at high latitude at high solar activity

Conclusions

In this thesis presents the validation of three ionospheric models, such as the Neustrelitz Peak Density Model (NPDM), the Neustrelitz Peak High Model (NPHM) and quick-run ionospheric electron density model NeQuick using ground (ionosonde) - and space-based observations (IRO) at different latitudes and at different solar activity.

To compare models performance, we have computed the differences between ionosonde data, IRO data and model results for all hourly values of NmF2 and hmF2 and estimated the RMS of differences at each verification station for the selected periods. Regarding ionosonde data the NPDM model performs better than the NeQuick for all stations. The NPHM model performs better than the NeQuick for most of the stations except at medium latitude at medium and high solar activity. The NeQuick shows the worst performance at low latitude at medium and high solar activity root mean square is equal 6.0 and $6.6 \times 10^{11} \text{ m}^{-3}$ respectively. The NPDM shows the worst performance at low latitude at medium and high solar activity root mean square is equal 5.0 and $4.6 \times 10^{11} \text{ m}^{-3}$ respectively. The NPDM model shows the best performance at low latitude at low and medium solar activity root mean square is equal 0.7 and $1.1 \times 10^{11} \text{ m}^{-3}$, respectively. Regarding IRO data the NPDM model performs better than the NeQuick for most of the stations except at low latitude at high solar activity. Both models show the best performance at low latitude at low solar activity and root mean square is equal $1.8 \times 10^{11} \text{ m}^{-3}$. The NPHM model shows the best performance at medium latitude at medium solar activity. The results show that the NPDM and NPHM models show better performance than the NeQuick model on average.

Regarding time serious analysis the NeQuick model follows the observation better than NPDM and NPHM for three stations: JR055 (JULIUSRUH/RUGEN), RL052 (CHILTON) and RO041 (ROME) model during 22:00-24:00 LT period.

The performance of the model may be further improved by changing coefficients, which describing the local time variation and solar activity dependence.

References

Day and night structure of the ionosphere:

<http://www.sws.bom.gov.au/Educational/1/2/5>.

Di Giovanni, G. and S. R. Radicella, An analytical model of the electron density profile in the ionosphere”, Adv. Space Res., 10, No. 11, 27-30, 1990

Forbes, J. M., E. P. Scott, and Z. Xiaoli (2000), Variability of the ionosphere, J. Atmos. Sol. Terr. Phys., 62, 685–693, doi:10.1016/S1364-6826(00)00029-8

Hochegger, G., B. Nava, S. M. Radicella, and R. Leitinger (2000), A family of ionospheric models for different uses, Phys. Chem. Earth Part C, 25(4), 307–310, doi: 10.1016/S1464-1917(00)00022-2

Leitinger, R., S.M. Radicella, B. Nava, G. Hochegger And J. Hafner (1999): NeQuick – COSTprof – NeUoGplas, a family of 3D electron density models, in Proceedings of the COST251 Madeira Workshop, 75-89.

Mandea, M., and S. Macmillan (2000), International Geomagnetic Reference Field—The eighth generation, Earth Planets Space, 52(12), 1119–1124.

Marcel H. De Canck., IONOSPHERE//antenneX Online Issue No. 63 — July 2002.

Jayachandran et al (1992).

Marco Limberger, Ionosphere modeling from GPS radio occultations and complementary data based on B-splines. – München, 2015.

Martyn, D. F. (1955), The Physics of the Ionosphere, 254 pp., Phys. Soc., London

Nava, B., P. Coisson, and S. M. Radicella (2008), A new version of the NeQuick ionosphere electron density model, J. Atmos. Sol. Terr. Phys., 70(15), 1856–1862, doi:10.1016/j.jastp.2008.01.015

NOAA National Data Center: <https://www.ngdc.noaa.gov/>.

Rishbeth, H., and O. K. Garriott (Eds.) Introduction to Ionospheric Physics (1969), Acad. Press, New York.

Vertical temperature profile of the atmosphere:

<http://unilaggeography2012.blogspot.nl/p/gry-101-introduction-to-physical.html>.

Matveev L.T. Course of general meteorology. Physics of the Atmosphere. -Lenigrad: Hydrometeorological Institute, 1984. - 751.

Zuev VE, Komarov VS Statistical models of temperature and gas components of the atmosphere. - Leningrad: Gidrometeoizdat (1986).

List of figures

- Fig.2.1. Vertical temperature profile of the atmosphere
- Fig.2.2. The structure of the ionosphere
- Fig.2.3. Day and night structure of the ionosphere
- Fig.2.4. Asymmetry of the Equatorial Ionization Anomaly. E donates an eastward electric field and B is the northward geomagnetic field Scheme Anderson and Roble (1981)
- Fig.3.1. Three fundamental ionosphere model types (REF)
- Fig.4.1. Example of IPS file (NmF2)
- Fig.5.1. Diurnal and seasonal variations at high latitude at low solar activity
- Fig.5.2. Diurnal and seasonal variations at high latitude at medium solar activity
- Fig.5.3. Diurnal and seasonal variations at high latitude at high solar activity
- Fig.5.4. Diurnal and seasonal variations at medium latitude at low solar activity
- Fig.5.5. Diurnal and seasonal variations at medium latitude at medium solar activity
- Fig.5.6. Diurnal and seasonal variations at medium latitude at high solar activity
- Fig.5.7. Diurnal and seasonal variations at low latitude at low solar activity
- Fig.5.8. Diurnal and seasonal variations at low latitude at medium solar activity
- Fig.5.9. Diurnal and seasonal variations at low latitude at high solar activity
- Fig.5.10. Diurnal and seasonal variations at low latitude at low solar activity (SPIDR)
- Fig.5.11. Diurnal and seasonal variations at low latitude at low solar activity (IPS)
- Fig.5.12. Diurnal and seasonal variations at low latitude at medium solar activity (SPIDR)
- Fig.5.13. Diurnal and seasonal variations at low latitude at medium solar activity (IPS)
- Fig.5.14. Diurnal and seasonal variations at low latitude at high solar activity (SPIDR)
- Fig.5.15. Diurnal and seasonal variations at low latitude at high solar activity (IPS)
- Fig.5.16. Diurnal and seasonal variations at medium latitude at low solar activity (SPIDR)
- Fig.5.17. Diurnal and seasonal variations at medium latitude at low solar activity (IPS)
- Fig.5.18. Diurnal and seasonal variations at medium latitude at medium solar activity (SPIDR)
- Fig.5.19. Diurnal and seasonal variations at medium latitude at medium solar activity (IPS)
- Fig.5.20. Diurnal and seasonal variations at medium latitude at high solar activity (SPIDR)
- Fig.5.21. Diurnal and seasonal variations at medium latitude at high solar activity (IPS)
- Fig.5.22. Diurnal and seasonal variations at high latitude at low solar activity (SPIDR)
- Fig.5.23. Diurnal and seasonal variations at high latitude at medium solar activity (SPIDR)
- Fig.5.24. Diurnal and seasonal variations at high latitude at high solar activity (SPIDR)
- Fig.5.25. Diurnal and seasonal variations at high latitude at low solar activity
- Fig.5.26. Diurnal and seasonal variations at high latitude at medium solar activity
- Fig.5.27. Diurnal and seasonal variations at high latitude at high solar activity
- Fig.5.28. Diurnal and seasonal variations at medium latitude at low solar activity
- Fig.5.29. Diurnal and seasonal variations at medium latitude at medium solar activity

- Fig.5.30. Diurnal and seasonal variations at medium latitude at high solar activity
- Fig.5.31. Diurnal and seasonal variations at low latitude at low solar activity
- Fig.5.32. Diurnal and seasonal variations at low latitude at low solar activity
- Fig.5.33. Diurnal and seasonal variations at low latitude at medium solar activity
- Fig.5.34. Diurnal and seasonal variations at low latitude at high solar activity
- Fig.5.35. Seasonal variation NmF2 and F10p7 for station JR055 (2009-2011, 2014)
- Fig.5.36. Seasonal variation NmF2 and F10p7 for station JR055 (2015-2018)
- Fig.5.37. Seasonal variation NmF2 and F10p7 for station JR055 (2009-2012)
- Fig.5.38. Seasonal variation NmF2 and F10p7 for station JR055 (2013-2016)
- Fig.5.39. Seasonal variation NmF2 and F10p7 for station RL052 (2017-2018)
- Fig.5.40. Seasonal variation NmF2 and F10p7 for station RL052 (2009-2011, 2013)
- Fig.5.41. Seasonal variation NmF2 and F10p7 for station RL052 (2014-2017)
- Fig.5.42. Seasonal variation NmF2 and F10p7 for station RO041 (2018)
- Fig.5.43. Histogram $NmF2_{mod}$ - $NmF2_{obs}$ and $hmF2_{mod}$ - $hmF2_{obs}$ at high latitude at low solar activity
- Fig.5.44. Histogram $NmF2_{mod}$ - $NmF2_{obs}$ and $hmF2_{mod}$ - $hmF2_{obs}$ at high latitude at medium solar activity
- Fig.5.45. Histogram $hmF2_{mod}$ - $hmF2_{obs}$ at high latitude at high solar activity
- Fig.5.46. Histogram $NmF2_{mod}$ - $NmF2_{obs}$ and $hmF2_{mod}$ - $hmF2_{obs}$ at medium latitude at low solar activity
- Fig.5.47. Histogram $NmF2_{mod}$ - $NmF2_{obs}$ and $hmF2_{mod}$ - $hmF2_{obs}$ at medium latitude at medium solar activity
- Fig.5.48. Histogram $NmF2_{mod}$ - $NmF2_{obs}$ and $hmF2_{mod}$ - $hmF2_{obs}$ at medium latitude at high solar activity
- Fig.5.49. Histogram $NmF2_{mod}$ - $NmF2_{obs}$ at low latitude at low solar activity
- Fig.5.50. Histogram $NmF2_{mod}$ - $NmF2_{obs}$ at low latitude at medium solar activity
- Fig.5.51. Histogram $NmF2_{mod}$ - $NmF2_{obs}$ at low latitude at high solar activity
- Fig.5.52. Histogram $NmF2_{mod}$ - $NmF2_{obs}$ and $hmF2_{mod}$ - $hmF2_{obs}$ at low latitude at low solar activity
- Fig.5.53. Histogram $NmF2_{mod}$ - $NmF2_{obs}$ and $hmF2_{mod}$ - $hmF2_{obs}$ at low latitude at medium solar activity
- Fig.5.54. Histogram $NmF2_{mod}$ - $NmF2_{obs}$ at low latitude at high solar activity
- Fig.5.55. Histogram $NmF2_{mod}$ - $NmF2_{obs}$ at medium latitude at low solar activity
- Fig.5.56. Histogram $NmF2_{mod}$ - $NmF2_{obs}$ at medium latitude at medium solar activity
- Fig.5.57. Histogram $NmF2_{mod}$ - $NmF2_{obs}$ at medium latitude at high solar activity
- Fig.5.58. Histogram $NmF2_{mod}$ - $NmF2_{obs}$ at high latitude at low solar activity
- Fig.5.59. Histogram $NmF2_{mod}$ - $NmF2_{obs}$ at high latitude at medium solar activity
- Fig.5.60. Histogram $NmF2_{mod}$ - $NmF2_{obs}$ at high latitude at high solar activity
- Fig.6.1. Diurnal and seasonal variations at high latitude at low solar activity
- Fig.6.2. Diurnal and seasonal variations at high latitude at medium solar activity
- Fig.6.3. Diurnal and seasonal variations at high latitude at high solar activity
- Fig.6.4. Diurnal and seasonal variations at medium latitude at low solar activity
- Fig.6.5. Diurnal and seasonal variations at medium latitude at medium solar activity

- Fig.6.6. Diurnal and seasonal variations at medium latitude at high solar activity
- Fig.6.7. Diurnal and seasonal variations at low latitude at low solar activity
- Fig.6.8. Diurnal and seasonal variations at low latitude at medium solar activity
- Fig.6.9. Diurnal and seasonal variations at low latitude at high solar activity
- Fig.6.10. Diurnal and seasonal variations at low latitude at low solar activity
- Fig.6.11. Diurnal and seasonal variations at low latitude at medium solar activity
- Fig.6.12. Diurnal and seasonal variations at low latitude at high solar activity
- Fig.6.13. Diurnal and seasonal variations at medium latitude at low solar activity
- Fig.6.14. Diurnal and seasonal variations at medium latitude at medium solar activity
- Fig.6.15. Diurnal and seasonal variations at medium latitude at high solar activity
- Fig.6.16. Diurnal and seasonal variations at high latitude at low solar activity
- Fig.6.17. Diurnal and seasonal variations at high latitude at medium solar activity
- Fig.6.18. Diurnal and seasonal variations at high latitude at high solar activity
- Fig.6.19. Diurnal and seasonal variations at high latitude for low solar activity
- Fig.6.20. Diurnal and seasonal variations at high latitude for medium solar activity
- Fig.6.21. Diurnal and seasonal variations at high latitude for high solar activity
- Fig.6.22. Diurnal and seasonal variations at medium latitude for low solar activity
- Fig.6.23. Diurnal and seasonal variations at medium latitude for medium solar activity
- Fig.6.24. Diurnal and seasonal variations at medium latitude for high solar activity
- Fig.6.25. Diurnal and seasonal variations at low latitude for low solar activity
- Fig.6.26. Diurnal and seasonal variations at low latitude for medium solar activity
- Fig.6.27. Diurnal and seasonal variations at low latitude for high solar activity
- Fig.6.28. Diurnal and seasonal variations at low latitude for low solar activity
- Fig.6.29. Diurnal and seasonal variations at low latitude for medium solar activity
- Fig.6.30. Diurnal and seasonal variations at low latitude for high solar activity
- Fig.6.31. Diurnal and seasonal variations at medium latitude for low solar activity
- Fig.6.32. Diurnal and seasonal variations at medium latitude for medium solar activity
- Fig.6.33. Diurnal and seasonal variations at medium latitude for high solar activity
- Fig.6.34. Diurnal and seasonal variations at high latitude for low solar activity
- Fig.6.35. Diurnal and seasonal variations at high latitude for medium solar activity
- Fig.6.36. Diurnal and seasonal variations at high latitude for high solar activity
- Fig.6.37. Histogram $NmF2_{mod}$ - $NmF2_{obs}$ and $hmF2_{mod}$ - $hmF2_{obs}$ at high latitude at low solar activity
- Fig.6.38. Histogram $NmF2_{mod}$ - $NmF2_{obs}$ and $hmF2_{mod}$ - $hmF2_{obs}$ at high latitude at medium solar activity
- Fig.6.39. Histogram $NmF2_{mod}$ - $NmF2_{obs}$ and $hmF2_{mod}$ - $hmF2_{obs}$ at high latitude at high solar activity
- Fig.6.40. Histogram $NmF2_{mod}$ - $NmF2_{obs}$ and $hmF2_{mod}$ - $hmF2_{obs}$ at medium latitude at low solar activity
- Fig.6.41. Histogram $NmF2_{mod}$ - $NmF2_{obs}$ and $hmF2_{mod}$ - $hmF2_{obs}$ at medium latitude at medium solar activity

- Fig.6.42. Histogram $NmF2_{mod}$ - $NmF2_{obs}$ and $hmF2_{mod}$ - $hmF2_{obs}$ at medium latitude at high solar activity
- Fig.6.43. Histogram $NmF2_{mod}$ - $NmF2_{obs}$ and $hmF2_{mod}$ - $hmF2_{obs}$ at low latitude at low solar activity
- Fig.6.44. Histogram $NmF2_{mod}$ - $NmF2_{obs}$ and $hmF2_{mod}$ - $hmF2_{obs}$ at low latitude at medium solar activity
- Fig.6.45. Histogram $NmF2_{mod}$ - $NmF2_{obs}$ and $hmF2_{mod}$ - $hmF2_{obs}$ at low latitude at high solar activity
- Fig.6.46. Histogram $NmF2_{mod}$ - $NmF2_{obs}$ and $hmF2_{mod}$ - $hmF2_{obs}$ at low latitude at low solar activity
- Fig.6.47. Histogram $NmF2_{mod}$ - $NmF2_{obs}$ and $hmF2_{mod}$ - $hmF2_{obs}$ at low latitude at medium solar activity
- Fig.6.48. Histogram $NmF2_{mod}$ - $NmF2_{obs}$ and $hmF2_{mod}$ - $hmF2_{obs}$ at low latitude at high solar activity
- Fig.6.49. Histogram $NmF2_{mod}$ - $NmF2_{obs}$ and $hmF2_{mod}$ - $hmF2_{obs}$ at medium latitude at low solar activity
- Fig.6.50. Histogram $NmF2_{mod}$ - $NmF2_{obs}$ and $hmF2_{mod}$ - $hmF2_{obs}$ at medium latitude at medium solar activity
- Fig.6.51. Histogram $NmF2_{mod}$ - $NmF2_{obs}$ and $hmF2_{mod}$ - $hmF2_{obs}$ at medium latitude at high solar activity
- Fig.6.52. Histogram $NmF2_{mod}$ - $NmF2_{obs}$ and $hmF2_{mod}$ - $hmF2_{obs}$ at high latitude at low solar activity
- Fig.6.53. Histogram $NmF2_{mod}$ - $NmF2_{obs}$ and $hmF2_{mod}$ - $hmF2_{obs}$ at high latitude at medium solar activity
- Fig.6.54. Histogram $NmF2_{mod}$ - $NmF2_{obs}$ and $hmF2_{mod}$ - $hmF2_{obs}$ at high latitude at high solar activity

List of tables

Table 4.1. Station coordinates (IPS)

Table 5.1. The validation strategy

Table 5.2. Geographic coordinates of ionosonde stations from SPIDR at high latitude

Table 5.3. Geographic coordinates of ionosonde stations from SPIDR at medium latitude

Table 5.4. Geographic coordinates of ionosonde stations from SPIDR at low latitude

Table 5.5. Geographic coordinates of ionosonde stations from SPIDR at low latitude

Table 5.6. Geographic coordinates of ionosonde stations from SPIDR at medium latitude

Table 5.7. Geographic coordinates of ionosonde stations from SPIDR at high latitude

Table 5.8. Geographic coordinates of ionosonde stations from IPS at low latitude

Table 5.9. Geographic coordinates of ionosonde stations from IPS at medium latitude

Table 5.10. The validation strategy

Table 5.11. Geographic coordinates of ionosonde stations from SPIDR at high latitude

Table 5.12. Geographic coordinates of ionosonde stations from SPIDR at medium latitude

Table 5.13. Geographic coordinates of ionosonde stations from SPIDR at low latitude

Table 5.14. Geographic coordinates of ionosonde stations from SPIDR at low latitude

Table 5.15. Number of obs. used

Table 5.16. RMS values for ionosonde data at different latitudes at different solar activity

Table 5.17. RMS values for IRO data at different latitudes at different solar activity